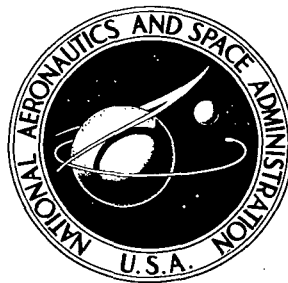


NASA TECHNICAL NOTE



NASA TN D-5393

C.1

NASA TN D-5393



LOAN COPY: RETURN TO
AFWL (WLOL-2)
KIRTLAND AFB, N MEX

EFFECT OF JET VELOCITY AND AXIAL
LOCATION OF NOZZLE EXIT ON THE
PERFORMANCE OF A TWIN-JET AFTERBODY
MODEL AT MACH NUMBERS UP TO 2.2

by Bobby Lee Berrier and Frederick H. Wood, Jr.

Langley Research Center

Langley Station, Hampton, Va.



0132220

1. Report No. NASA TN D-5393	2. Government Accession No.	3. Recipient's Catalog No.
4. Title and Subtitle EFFECT OF JET VELOCITY AND AXIAL LOCATION OF NOZZLE EXIT ON THE PERFORMANCE OF A TWIN-JET AFTERBODY MODEL AT MACH NUMBERS UP TO 2.2	5. Report Date September 1969	6. Performing Organization Code
7. Author(s) Bobby Lee Berrier and Frederick H. Wood, Jr.	8. Performing Organization Report No. L-6671	10. Work Unit No. 720-03-11-01-23
9. Performing Organization Name and Address NASA Langley Research Center Hampton, Va. 23365	11. Contract or Grant No.	13. Type of Report and Period Covered Technical Note
12. Sponsoring Agency Name and Address National Aeronautics and Space Administration Washington, D.C. 20546	14. Sponsoring Agency Code	
15. Supplementary Notes		
16. Abstract The twin-jet afterbody model used two balances to measure thrust-minus-afterbody drag, and afterbody drag separately at static conditions and at Mach numbers up to 2.20 at a constant angle of attack of 0° . A high-pressure air system was used to simulate the nozzle flow at jet total-pressure ratios up to 22.0. All configurations had identical nondimensional area distributions. The results indicate that performance was generally increased by moving the jet exits to the extreme aft end of the afterbody for Mach numbers up to 1.30. The configurations utilizing nozzles with low exit velocity (convergent nozzles) had lower afterbody drag than configurations utilizing nozzles with higher exit velocity (convergent-divergent nozzles) at most test conditions.		
17. Key Words Suggested by Author(s) Twin-jet afterbody model Nozzle exhaust velocity Nozzle axial location	18. Distribution Statement Unclassified - Unlimited	
19. Security Classif. (of this report) Unclassified	20. Security Classif. (of this page) Unclassified	21. No. of Pages 78
		22. Price* \$3.00

EFFECT OF JET VELOCITY AND AXIAL LOCATION OF NOZZLE EXIT
ON THE PERFORMANCE OF A TWIN-JET AFTERBODY MODEL
AT MACH NUMBERS UP TO 2.2

By Bobby Lee Berrier and Frederick H. Wood, Jr.
Langley Research Center

SUMMARY

The effects of jet-exhaust flow velocity and longitudinal location of nozzle exits on the performance of twin-jet afterbodies have been investigated at static conditions and at Mach numbers of 0.50 to 2.2. All afterbody configurations had identical nondimensional area distributions, the cross section of cylindrical jet plumes as solid bodies being included in the area. Direct measurements of thrust-minus-afterbody drag and afterbody drag were made by using two separate force balances in the model. The jet total-pressure ratio was varied from 1.0 to approximately 22.0 depending on the Mach number. Two nonjet reference bodies representing an axisymmetric (single jet) minimum-wave-drag body and a minimum wave-drag body having oval sections (twin jet) were also investigated, and the drag measurements were compared with calculations based on axisymmetric wave-drag theory.

The results indicate that the configuration with no surface adjacent to a jet-flow stream (exits at extreme aft end, no interfairing) generally has the lowest drag at Mach numbers up to 1.3. However, at Mach numbers of 1.83 and 2.2, a small surface adjacent to the jet flow (small interfairing) was beneficial. The configurations utilizing nozzles with low exit velocity (convergent nozzles) had lower afterbody drag than configurations utilizing nozzles with a higher exit velocity (convergent-divergent nozzles) at most test conditions. The accuracy of equivalent body of revolution wave-drag calculations decreased when surfaces were placed adjacent to jet-exhaust flow.

INTRODUCTION

Although much performance data exist for single-engine isolated nacelle jet models utilizing various nozzle types (refs. 1 to 9), little work has been done on multiple-jet installations until recently. Reference 1 indicates that the aft portion (afterbody) of a twin-jet fighter-type airplane can account for a large part of total airplane drag and reference 10 indicates a 4 percent to 6 percent net thrust loss due to installation effects on a twin-jet model. In addition to model asymmetry, jet interference on airplane

structure and mutual interference between jet streams further complicate installation of multiple jets in airplane configurations. (See refs. 1, 2, and 10 to 13.) References 1, 10, and 13 show that the entire afterbody-nozzle combination must be integrated as a unit in order to reduce the performance loss from nozzle installation.

An investigation was conducted in the Langley 16-foot transonic tunnel and 4- by 4-foot supersonic pressure tunnel to evaluate the effect of jet stream exit velocity and longitudinal location of the jet exit on the performance of twin-jet afterbody-nozzle combinations using a pylon-supported model with air exhaust. Three twin-jet afterbody shapes with the same cross-sectional area distribution but different nozzle exit locations and two nozzle configurations (convergent and convergent-divergent) were used in the investigation. In addition, two reference bodies were investigated to obtain a minimum afterbody drag value. Theoretical values of wave drag were calculated from slender body theory and are compared with experimental data. Tests were conducted at Mach numbers from 0.50 to 2.2 at an angle of attack of 0° and at nozzle-jet total-pressure ratios from 1.0 (jet off) to approximately 22.0 depending on Mach number.

SYMBOLS

A	cross-sectional area, meters ²
A_e	exit area of one nozzle, meters ²
A_{\max}	maximum cross-sectional area, meters ²
A_{seal}	cross-sectional area enclosed by seal strip, meters ²
A_t	throat area of one nozzle, meters ²
$C_{A,a}$	afterbody axial-force (drag) coefficient, positive downstream, $\frac{F_{A,t}}{q_\infty A_{\max}}$; for static conditions, $\frac{F_{A,t}}{p_\infty A_{\max}}$
C_p	pressure coefficient, $\frac{p_l - p_\infty}{q_\infty}$
$C_{p,b}$	base pressure coefficient, $\frac{p_b - p_\infty}{q_\infty}$
$C_{p,j}$	pressure coefficient on jth orifice row ($j = 1$ to 6)
d_e	exit diameter of nozzle, meters

$F_{A,t}$	total axial force (afterbody plus nozzles), positive downstream, newtons
$F_{bal,a}$	force measured by drag balance, positive downstream, newtons
$F_{bal,j}$	force measured by thrust-minus-drag balance, positive upstream, newtons
F_i	ideal thrust for complete isentropic expansion of jet flow, $m \sqrt{2R \frac{\gamma}{\gamma - 1} T_{t,j} \left[1 - \left(\frac{p_\infty}{p_{t,j}} \right)^\gamma \right]}, \text{ newtons}$
F_j	jet thrust, positive upstream, newtons
H	half maximum afterbody height, meters
h	half afterbody height measured from afterbody center line (see fig. 4), meters
l	length of model measured from nose, 121.920 centimeters
M	free-stream Mach number
M_e	jet-exit Mach number
m	measured mass flow rate, kilograms/second
p_b	base pressure, newtons/meter ²
p_{es}	static pressure at external seal station, newtons/meter ²
p_i	internal static pressure, newtons/meter ²
p_l	local static pressure, newtons/meter ²
$p_{t,j}$	jet total pressure, newtons/meter ²
p_∞	free-stream or ambient static pressure, newtons/meter ²
q_∞	free-stream dynamic pressure, newtons/meter ²

r	radius at nozzle center line, meters
r_b	base radius, meters
$r_{b,max}$	maximum base radius, meters
$r_{b,min}$	minimum base radius, meters
r_e	nozzle exit radius, meters
R	maximum afterbody radius, meters; or gas constant, joules/kilogram-°Kelvin
s	distance between nozzle center lines, meters
$T_{t,j}$	jet stagnation temperature, °Kelvin
w	half-width of afterbody, meters
x	axial coordinate from nose, meters
y	distance from afterbody center line to nozzle tailpipe center line, meters
y_{max}	maximum width of interfairing at given axial location, meters
y_{min}	minimum width of interfairing at given axial location, meters
γ	ratio of specific heats

A bar over symbol indicates an average condition.

APPARATUS AND METHODS

Wind Tunnels

The present investigation was conducted in the Langley 16-foot transonic tunnel and in the Langley 4- by 4-foot supersonic pressure tunnel. The Langley 16-foot transonic tunnel is a single-return, atmospheric wind tunnel with an octagonal test section and continuous air exchange. The tunnel has a continuously variable speed range from a Mach number of 0.20 to 1.30. The Langley 4- by 4-foot supersonic pressure tunnel is a single-return, continuous-flow wind tunnel with a stagnation pressure range of $0.2758 \times 10^5 \text{ N/m}^2$

to $2.0684 \times 10^5 \text{ N/m}^2$ and a stagnation temperature range of 316.7° K to 322.2° K . By use of a variable wall tunnel nozzle, the Mach number can be varied from 1.25 to 2.60.

Model and Support System

A sketch of the strut-supported, twin turbojet-engine simulator model used in the investigation is presented in figure 1, and a photograph of the model installed in the test section of the Langley 16-foot transonic tunnel is given in figure 2.

The external "metric" portion (afterbody) of the model begins 83.345 cm from the nose and attaches to a drag balance (measures afterbody force) which in turn is attached in series to a thrust-minus-drag balance (measures afterbody and nozzle force) as shown in figure 3. (The metric portion is that portion of a body attached to a balance.) The external metric portion of the cylindrical reference body started 52.324 cm from the nose and was attached directly to the thrust-minus-drag balance. A 0.155-cm annular gap between the jet afterbodies and nozzles was required for clearance to prevent fouling of the two balance systems. A flexible teflon strip inserted into slots machined into the metric and nonmetric portions of the model was used as a seal to prevent internal flow in the model. The low coefficient of friction of teflon minimized restraint on the two balances. Transition was fixed 6.03 cm from the nose with a 0.25-cm-wide strip of number 100 grit.

A high-pressure air system was used to supply air ($\gamma = 1.4$) to the twin-engine nozzles at a stagnation temperature of approximately 294° K . Air was piped into the model and passed through eight orifice nozzles into the low-pressure plenum chamber. (See fig. 1.) The orifice nozzles were located perpendicular to the model longitudinal axis to eliminate transfer of axial momentum. The air was passed through the tailpipe-nozzle system to simulate the exhaust of a twin-jet configuration.

A sketch giving dimensions and pressure-orifice locations for the three jet afterbodies and two minimum wave-drag reference bodies used in this investigation is presented in figure 4 and a photograph of four of the afterbody configurations is given as figure 5. Afterbody configurations A-1, A-2, and A-3 had nozzle exits located 121.92 cm, 111.76 cm, and 101.60 cm, respectively, from the model nose. Nozzle spacing ratio s/d_e was constant and equal to 1.874 for the three jet configurations. The two reference bodies had closed bases at station 121.92 with no provisions for jet flow. All afterbodies of this investigation had the same total length (121.92 cm) and by including two cylindrical jets as equivalent solid bodies, had the same nondimensional cross-sectional area distribution as shown in figure 6 by the solid line. The area distribution shown in figure 6 between $x/l = 0.685$ and $x/l = 1.0$ was calculated by a computer program, for axisymmetric bodies, adapted from reference 14 and is representative of a minimum-wave-drag body at a Mach number of 1.000001 with the restraints of a given

forebody geometry, afterbody length, maximum cross-sectional area, and base area. The area distribution of the jet afterbodies was the same as the equivalent axisymmetric minimum-wave-drag body area distribution.

Figure 7 presents a sketch showing geometry and instrumentation details of the two nozzle types investigated. Both nozzle sets were designed for the specific-heat ratio of 1.40 for air. The convergent nozzle set was designed for $M_e = 1.0$ ($p_{t,j}/p_\infty = 1.89$). The convergent-divergent nozzle set was designed for $M_e = 2.0$ ($p_{t,j}/p_\infty = 7.82$) by utilizing the method of reference 15 which approximates an isentropic nozzle contour. The exit divergence angle for the convergent-divergent nozzles was equal to 3° .

Instrumentation

External static-pressure orifices were located on the afterbodies as shown in figure 4. No external static pressures were measured on afterbody A-3. External static pressures were not measured on the afterbodies in the Langley 4- by 4-foot supersonic pressure tunnel. Internal pressures were measured around the afterbody cavity at three axially spaced internal orifice locations and eight external static pressures (values averaged) were measured at orifices located on both sides of the seal gap (see fig. 3) between the centerbody and afterbodies. These pressure measurements were used to adjust the balance force measurements. The total pressure and stagnation temperature of the jet flow were measured in each tailpipe nozzle at locations indicated in figure 1.

Forces and moments on the metric portions of the model were obtained by means of a 5-component strain-gage balance used to measure thrust minus total drag and a tandem 6-component auxiliary strain-gage balance which measured forces and moments on the afterbody shell. Figure 3 presents a sketch showing the metric portion of the model for each balance. An electronic turbine flowmeter was used to obtain air mass flow rate to the nozzles.

Data obtained in the Langley 16-foot transonic tunnel were recorded simultaneously on magnetic tape. Approximately 5 frames of data were taken over a time period of about 1 second for each data point and the average value was used for computations. Data obtained in the Langley 4- by 4-foot supersonic pressure tunnel were transmitted to the self-balancing potentiometers, digitized, and punched into cards. An electrically actuated pressure scanning valve was used for measuring and recording the internal and external pressures.

Data Reduction

The recorded data were used to compute standard force and pressure coefficients. Pressure forces on the afterbodies were obtained by assigning to each pressure orifice

an incremental area projected on a plane normal to the model axis and by numerically integrating the incremental forces. No correction was made for strut interference.

The gross thrust minus afterbody axial force (drag) was obtained directly by the thrust-minus-drag balance. (See fig. 3.) The forces sensed by the balance and included in the axial-force term $F_{bal,j}$ are nozzle thrust, afterbody external and internal axial forces transferred to the thrust-minus-drag balance through the tandem drag balance, and internal axial forces on the nozzle system. This force measurement was adjusted to thrust-minus-afterbody drag as follows:

$$F_j - F_{A,t} = F_{bal,j} + (\bar{p}_{es} - p_{\infty})(A_{max} - A_{seal}) + (\bar{p}_i - p_{\infty})A_{seal}$$

Afterbody axial force (drag) was obtained directly from the tandem drag balance. (See fig. 3.) Included in the afterbody axial force (drag) term is the force acting on the portion of the base made up of the physical afterbody base, the area of the annulus between the afterbody and nozzle, and the physical nozzle base area. The afterbody axial force was computed as follows:

$$F_{A,t} = F_{bal,a} - (\bar{p}_{es} - p_{\infty})(A_{max} - A_{seal}) - (\bar{p}_i - p_{\infty})(A_{seal} - 2A_e)$$

Nozzle internal thrust is obtained by combining the two balance axial forces as follows:

$$F_j = F_{bal,j} + F_{bal,a} + (\bar{p}_i - p_{\infty})2A_e = (F_j - F_{A,t}) + F_{A,t}$$

The internal-pressure correction terms used in the previous force equations can be large and they approached an order of magnitude equal to the drag balance reading ($F_{bal,a}$) in several instances. The three measured values of internal pressure were within 0.2-percent agreement at all test conditions and indicated no internal flow inside the afterbody shell. A total-pressure rake was used to survey the jet total-pressure distribution at the exit of the convergent nozzles and the jet total-pressure probe reading was corrected to the integrated value of jet total pressure at the exit to eliminate non-uniformity of total-pressure effects. The largest correction made for nonuniformity of total pressure was approximately 5 percent. The integrated value of jet total pressure at the exit was used to calculate the ideal thrust for complete isentropic expansion of the jet flow for the convergent nozzle set. A survey of the jet total-pressure distribution at the exit of the convergent-divergent nozzle set was not made. However, as a result of a larger convergence angle, a more uniform total-pressure distribution should exist inside the convergent-divergent nozzle set.

Afterbody external skin-friction drag (used in conjunction with theoretical wave drag and integrated pressure drag) was calculated by using the Frankl and Voishel equation for compressible, turbulent flow on a flat plate. (See ref. 16.)

Test

Data were obtained in the Langley 16-foot transonic tunnel at Mach numbers from 0 to 1.3 and in the Langley 4- by 4-foot supersonic tunnel at Mach numbers of 1.83 and 2.2 at a stagnation pressure of $1.241 \times 10^5 \text{ N/m}^2$ and a stagnation temperature of 316.7° K . The angle of attack was held at a constant value of 0° during the entire investigation. Reynolds number based on model length varied from approximately 1.16×10^7 at $M = 0.50$ to 1.50×10^7 at $M = 1.3$ in the Langley 16-foot tunnel and from 1.79×10^7 at $M = 1.8$ to 1.49×10^7 at $M = 2.2$ in the Langley 4- by 4-foot supersonic pressure tunnel. The ratio of jet total pressure to free-stream static pressure was varied from 1.0 (jet off) to about 22.0 depending on Mach number.

RESULTS AND DISCUSSION

Pressure Distributions

Reference bodies.- The pressure distributions on the axisymmetric reference body and the twin jet (asymmetric) reference body are shown in figures 8 and 9, respectively. The axisymmetric reference body had a symmetrical flow field indicated by nearly identical pressure distributions on each orifice row. The symmetrical flow field indicates little or no strut interference. Pressure recovery was obtained over the aft 20 percent of the axisymmetric reference body and some positive pressure coefficients were obtained at all Mach numbers up to 1.3. Base-pressure coefficient remained negative for the test conditions shown.

The twin-jet reference body had an asymmetric pressure distribution as shown by figure 9. This result was expected as the curvature on the body at various orifice rows was different on the twin-jet reference body. Pressure recovery was obtained over the aft portion of the afterbody, some positive pressure coefficients occurring on all rows. Some positive base-pressure coefficients were also obtained. Although the nondimensional area distributions of the two reference bodies are identical, local slopes on the two bodies were different and results in different pressure distributions being obtained on the two reference bodies (for example, compare $C_{p,1}$ data from figures 8 and 9 at $M = 1.3$).

Jet afterbodies.- Figures 10 and 11 present the pressure distributions on the A-1 and A-2 afterbodies, respectively, obtained by utilizing convergent nozzles. The most notable feature of the distributions on the A-1 afterbody is a region of positive pressure coefficients on the entire aft end of the body, positive pressure coefficients being over 15 to 20 percent of the body length in some instances. Increasing jet total-pressure ratio generally increases pressures on the aft end of the body.

Pressure coefficients on the A-2 afterbody shown in figure 11 generally remain negative except on the top and side of the interfairing between and downstream of the nozzle exits. For jet total-pressure ratios greater than 6.0, extreme expansions and compressions are exhibited on the interfairing side as a result of the jet-exhaust wave pattern impinging on the interfairing. These pressure fluctuations are decreased with increasing Mach number. Operation of the jet is generally favorable on the pressures forward of the nozzle exit while pressures downstream of the nozzle exit exhibit large variations with changing jet total-pressure ratio.

Pressure distributions on the A-1 and A-2 afterbodies utilizing the convergent-divergent nozzles are shown in figures 12 and 13, respectively. The influence of convergent-divergent nozzle jet operation on the afterbody pressure distributions is not as great as the influence of convergent nozzle jet operation shown in figures 10 and 11. This result is probably due to less jet pluming with the convergent-divergent nozzles for the pressure-ratio range of this investigation. With this exception, the pressure distributions obtained on the convergent-divergent nozzle configurations generally exhibit the same trends as the pressure distributions obtained on the convergent nozzle configurations.

Afterbody Drag

Reference bodies.- Figure 14 presents afterbody drag coefficients for the two reference afterbodies as a function of Mach number. The afterbody drag coefficients have base-pressure force removed from afterbody drag $F_{A,t}$. This pressure force was obtained from an integration over the base area of base pressures similar to those shown in figures 8 and 9. Also shown in figure 14 is a theoretical calculation of afterbody wave drag, as obtained from a wave-drag computer program of reference 14 which assumes an infinite cylinder extending downstream from the base of an axisymmetric body, plus calculated skin-friction drag. Calculated skin-friction drag on the twin-jet reference body is also presented as a separate quantity in figure 14.

Both reference afterbodies have the same nondimensional area distribution as shown in figure 6 and hence theoretically have identical wave-drag coefficients. However, the axisymmetric (single jet) reference body had circular-shaped cross sections whereas the twin-jet reference body had oval-shaped cross sections.

Afterbody drag of the twin-jet reference body was higher than the afterbody drag of the single jet reference body at all test conditions at which both were investigated. Afterbody drag coefficient predicted by wave-drag theory agrees well with measured afterbody drag.

Figure 15 presents a comparison of afterbody drag on the twin-jet reference body derived by two methods, namely, afterbody drag obtained from balance measurements and

afterbody drag obtained from integration of afterbody pressures over the axially projected area. The integration of pressures method results in the lowest value of afterbody drag coefficient at all test conditions. It is believed that the more accurate method is direct measurement by a force balance.

Jet afterbodies.- Jet-off afterbody drag coefficients for the three jet afterbodies, the twin-jet reference body, and as predicted by wave-drag theory are presented in figure 16 as a function of Mach number. Of the three jet afterbodies, the A-1 afterbody (exit at extreme aft end) had the lowest jet-off afterbody drag at all test conditions. The twin-jet reference afterbody had lower drag than the jet afterbodies at Mach numbers up to 1.3; however, at Mach numbers of 1.83 and 2.2, both the A-1 and A-2 afterbodies had lower drag values than the reference afterbody, probably because the area distribution was optimized for a Mach number only slightly greater than 1.00. In addition, base drag on the afterbody and nozzle bases and the annular gap between is included in the data of figure 16 but is not accounted for by the wave-drag calculations.

The afterbody drag coefficient predicted by equivalent-body-of-revolution wave-drag theory is low when compared with direct measurements on the afterbodies. However, it should be noted that although the theory includes no base drag, the four afterbodies shown in figure 16 were charged with some drag on the base, namely, that on the afterbody and nozzle bases and the clearance gap between the two. The reference-body afterbody drag was adjusted to include the same amount of base area as was charged to the jet afterbodies. The force on the remaining area was removed from the drag measurements by using the pressures measured at locations shown in figure 4(d). Afterbody drag coefficient determined by wave-drag theory would be increased approximately 0.004 at $M = 1.3$ if the same amount of base drag were charged to theory as was charged to the twin-jet reference body.

Figures 17 and 18 present afterbody drag coefficients for the three twin-jet afterbody configurations with convergent and convergent-divergent nozzles, respectively. Afterbody drag was obtained by two methods, first, by direct measurement by a strain-gage balance and, second, by integration of the pressures shown in figures 10 to 13. The measured drag values are shown by open symbols (figs. 17 and 18) and the integrated drag values by solid symbols (fig. 17). The integrated drag data were used to extend the range of jet total-pressure ratio.

Comparison of the convergent nozzle data with that obtained by using a convergent-divergent nozzle indicates that jet operation has a larger effect on afterbody drag when convergent nozzles are utilized. This trend was also indicated by the afterbody pressures previously presented. One possible explanation for this trend is that the convergent nozzle exhaust started pluming at a jet total-pressure ratio of approximately 1.89

and increased with increasing pressure ratio whereas the convergent-divergent nozzle exhaust does not start pluming until a pressure ratio of 7.82 is reached.

Figure 17 shows that convergent nozzle jet interference was generally favorable (jet-on drag less than jet-off drag) on the A-1 and A-2 afterbodies throughout the Mach number and jet total-pressure-ratio range investigated with the exception of $M = 0.50$. Unfavorable jet interference on the A-3 afterbody generally occurred during some portion of the pressure ratio range until a higher Mach number was reached, namely, $M = 1.15$. With the exception of the A-3 afterbody at Mach numbers up to 0.95, afterbody drag initially decreases, and then increases and decreases with increasing pressure ratio.

At Mach numbers up to 1.3, the afterbody with the exits at the extreme aft end (afterbody A-1) generally had the lowest afterbody drag. At transonic and low supersonic Mach numbers, a small interfairing between and downstream of the nozzle exits (afterbody A-2) was beneficial only at selective pressure ratios (for example, $M = 1.2$; $p_{t,j}/p_{\infty} = 1.5$ or 8.0). At supersonic speeds $M = 1.83$ and $M = 2.2$ the advantage of an interfairing between and downstream of the nozzle exits becomes apparent as the A-2 afterbody generally exhibits the lowest drag and the A-3 afterbody (large interfairing) which had substantially higher drag than the A-1 afterbody at subsonic Mach numbers, has lower drag than the A-1 afterbody at the higher jet total-pressure ratios.

One possible explanation for the unfavorable effect of interfairing surfaces at low pressure ratios (low Mach numbers) is that the convergent nozzles are operating near design and adjacent surfaces are aspirated by the near-cylindrical jet plume. At higher pressure ratios (high Mach numbers), the nozzle is substantially underexpanded and adjacent surfaces provide expansion surfaces on which beneficial thrust terms may be obtained.

Convergent-divergent nozzle jet interference is shown by figure 18 to be unfavorable for a wider range of Mach numbers and jet total-pressure ratios than the convergent nozzle jet interference shown in figure 17, probably because the convergent-divergent nozzles are usually operating overexpanded or near design ($p_{t,j}/p_{\infty} \leq 7.82$) and thus aspirate adjacent surfaces. Convergent-divergent jet interference on the three afterbodies was generally unfavorable at Mach numbers below 0.9. Above $M = 0.9$, mixed results were obtained. With convergent-divergent nozzles, the large interfairing afterbody (afterbody A-3) has the highest drag level throughout the entire range of test variables and the small interfairing afterbody (afterbody A-2) has only a slight advantage over the A-1 afterbody at selective jet total pressures at Mach numbers between 0.9 and 1.3.

Afterbody drag coefficient at design $p_{t,j}/p_{\infty}$ - Afterbody drag coefficient of the three afterbodies with both convergent ($M_e = 1.00$) and convergent-divergent ($M_e = 2.00$)

nozzles operating at their respective design jet total-pressure ratios of 1.89 and 7.82 is presented in figure 19 as a function of Mach number. Also shown in figure 19 are the values of afterbody drag coefficient as obtained from equivalent-body-of-revolution wave-drag theory. The theoretical values do not include any base drag as do the jet afterbodies (drag on nozzle and afterbody physical bases and the clearance gap between the two). The measured drag values are shown at design jet total-pressure ratio since at this condition, the jet plume should simulate an infinite cylinder extending downstream of the jet exit and agree closely with theory which assumes an infinite cylinder extending downstream from the base. Wave-drag calculations predict afterbody drag with reasonable accuracy for the afterbody with no surface adjacent to the jet flow (afterbody A-1); however, agreement between theory and experiment decreased when a surface was placed adjacent to the jet flow (afterbodies A-2 and A-3), particularly when nozzles with an exhaust Mach number of 2.00 (convergent-divergent) are utilized. For example, wave-drag values were approximately 10 percent low at $M = 1.2$ and 4 percent low at $M = 2.2$ for afterbody A-1, but for afterbody A-3, the agreement decreased so that the calculated values were approximately 24 percent low at $M = 1.2$ and 15 percent low at $M = 2.2$. This result was expected since wave-drag theory does not account for jet interference effects which can be large for configurations which include surfaces adjacent to jet exhaust flow. (See ref. 1.)

Afterbody drag obtained with each afterbody utilizing nozzles with an exhaust Mach number of 1.00 (convergent) was lower at all test conditions shown in figure 19 than the afterbody drag obtained by utilizing nozzles with an exhaust Mach number of 2.00 (convergent-divergent). Since a near-cylindrical jet exists for both nozzle sets at their respective design jet total-pressure ratios, the differences in afterbody drag for the same afterbody but utilizing different nozzles must be accounted for in the total (friction being neglected) by jet-afterbody interference differences produced by the difference in jet-flow exit velocity of the two nozzle sets. Hence, at the design jet total-pressure ratio, a jet exhaust with $M_e = 2.00$ (convergent-divergent nozzles) had a detrimental effect on afterbody drag of the afterbodies investigated when compared with the afterbody drag obtained with a jet exhaust with $M_e = 1.00$ (convergent nozzles). The detrimental jet interference increment of the convergent-divergent nozzles ($M_e = 2.00$) over the convergent nozzles ($M_e = 1.00$) generally decreases with increasing Mach number and increases with increasing distance between the nozzle exit and model end (that is, afterbody surface area exposed to the jet flow increases).

Performance Characteristics

Thrust-minus-drag ratio.- The variations of thrust-minus-drag ratio with jet total-pressure ratio and Mach number for the three jet afterbodies are shown in figure 20 for

the convergent nozzle configurations and in figure 21 for the convergent-divergent nozzle configurations. Thrust data at $M = 1.83$, for the convergent-divergent nozzles, were lost and thrust values obtained at $M = 0$ were substituted to obtain the values shown in figure 21(d). This procedure is sound if nozzle internal performance is not affected by external flow which should be the case when the nozzle is operating at or above the design pressure ratio. (Design pressure ratio is 7.82 for the convergent-divergent nozzles of this investigation.)

Thrust minus drag of the convergent nozzle configurations generally increases with increasing jet total-pressure ratio except at $M = 0$ where external drag is essentially zero and the nozzle internal thrust suffers from underexpansion losses for jet total-pressure ratios above 1.89. At Mach numbers up to 1.3, the A-1 afterbody (exits at extreme aft end) generally exhibits the highest thrust-minus-drag performance probably as a result of no losses due to aspiration of a surface adjacent to the jet flow as pointed out in the afterbody drag section. A few exceptions are shown at low jet total-pressure ratios as might be expected from the afterbody drag shown previously in figure 17. At Mach numbers of 1.83 and 2.2, an interfairing extending between and downstream of the nozzle exits improves thrust-minus-drag performance and is probably a result of the nozzles operating at an underexpanded condition, thrust being realized on the external expansion surface. The A-2 afterbody generally exhibits the highest thrust-minus-drag performance at $M = 1.83$ and $M = 2.2$. At the highest pressure ratios the lowest performance is obtained with the configuration having no interfairing (A-1 afterbody) as might be expected if thrust is indeed obtained on the interfairing of the A-2 and A-3 afterbodies.

Thrust-minus-drag performance of the three afterbodies utilizing convergent-divergent nozzles, shown in figure 21, generally exhibits the same trends shown in figure 20 for the convergent nozzle configurations. Thrust-minus-drag ratio increases with increasing jet total-pressure ratio. Nozzle overexpansion losses occur for jet total-pressure ratios below 7.82. At Mach numbers up to 1.3, the highest thrust-minus-drag performance is obtained with the A-1 afterbody (exits at extreme aft end). The A-2 afterbody (small interfairing) generally exhibits the highest thrust-minus-drag performance at Mach numbers of 1.83 and 2.20. The A-3 afterbody (large interfairing) exhibits the lowest performance at all test conditions when convergent-divergent nozzles are used. The improved performance obtained with convergent nozzles for the A-3 afterbody at $M = 1.83$ and $M = 2.20$ is not exhibited when convergent-divergent nozzles are utilized probably because the convergent-divergent nozzles are operating closer to design pressure ratio and hence the jet plume is not as large.

Internal performance.— The variation of internal performance F_j/F_i with jet total-pressure ratio and Mach number is presented in figures 22 and 23 for the convergent

and convergent-divergent nozzle configurations, respectively. Balance force $F_{bal,j}$ was lost at $M = 1.83$ for the convergent-divergent nozzle configurations.

For conditions of choked nozzle flow and no internal flow separation, internal performance of the nozzles of this investigation should not vary with Mach number or afterbody configuration. However, figure 22 shows some variation of internal performance with afterbody configurations incorporating convergent nozzles, particularly at low jet total-pressure ratios. One possible explanation, below the nozzle choke point, is that different back pressures, created by interfairings for example, changed the effective pressure ratio. The general shape of the curves follow that of ideal convergent thrust. Little or no variation of internal performance with Mach number or configuration is shown in figure 23 for the convergent-divergent nozzles.

CONCLUSIONS

An investigation of the effect of jet velocity and axial location of the nozzle exit on the performance of twin jet afterbodies indicated the following conclusions:

1. At Mach numbers from 0.50 to 1.30, afterbody drag was generally decreased and thrust minus drag was generally increased by moving the nozzle exits to the extreme aft end of the afterbody so that no afterbody surface exists adjacent to jet flow.

2. At Mach numbers of 1.83 and 2.2, afterbody drag was generally reduced and thrust minus drag was generally increased by moving the nozzle exits forward so that a small interfairing exists adjacent to the jet flow.

3. A large interfairing configuration generally gave the highest drag and lowest thrust-minus-drag performance at all test conditions.

4. Afterbody drag obtained on configurations with a jet-flow exit Mach number of 1.00 (convergent nozzles) was substantially lower than that obtained on configurations with a jet-flow exit Mach number of 2.00 (convergent-divergent nozzles) when both nozzle sets are operating on design (cylindrical jet plumes). The afterbody drag increment between nozzle sets for the same afterbody decreases with increasing Mach number and increases with increasing amount of surface adjacent to the jet flow. This drag increment is a sole result of jet-afterbody interference differences produced by the difference in jet-flow exit velocity of the two nozzle sets.

5. At design jet total-pressure ratio for each nozzle set, wave drag calculations based on an equivalent body of revolution predict drag approximately 4 percent to 10 percent low when no surface exists adjacent to the jet-flow stream. Accuracy of the

wave-drag calculations decreases when a surface exists adjacent to the jet-flow stream; for example, on the large interfairing configuration, the calculations were approximately 15 percent to 24 percent low.

Langley Research Center,
National Aeronautics and Space Administration,
Langley Station, Hampton, Va., June 23, 1969,
720-03-11-01-23.

REFERENCES

1. Runckel, Jack F.: Jet-Exit and Airframe Interference Studies on Twin-Engine-Fuselage Aircraft Installations. NASA TM X-1274, 1966. (Also available as NASA SP-124, pp. 229-244.)
2. Corson, Blake W., Jr.; and Schmeer, James W.: Summary of Research on Jet-Exit Installations. NASA TM X-1273, 1966.
3. Norton, Harry T., Jr.; Runckel, Jack F.; and Pendergraft, Odis C., Jr.: Transonic Performance of Two Convergent-Divergent Ejector Nozzles Designed for Corrected Secondary Flows of 3 and 9.4 Percent. NASA TM X-909, 1964.
4. Mercer, Charles E.; and Schmeer, James W.: Transonic Performance of Ejector Nozzles Having Zero Boattail Angle and an Internal Base. NASA TM X-1104, 1965.
5. Norton, Harry T., Jr.; and Pendergraft, Odis C., Jr.: Transonic Performance of a Convergent-Divergent Ejector Nozzle Designed for a Corrected Secondary-Weight-Flow Ratio of 0.07. NASA TM X-974, 1964.
6. Schmeer, James W.; Mercer, Charles E.; and Kirkham, Frank S.: Effect of Bypass Air on the Performance of a Blow-In-Door Ejector Nozzle at Transonic Speeds. NASA TM X-896, 1963.
7. Schmeer, James W.; Kirkham, Frank S.; and Salters, Leland B., Jr.: Performance Characteristics of a 10° Conical Plug Nozzle at Mach Numbers Up to 1.29. NASA TM X-913, 1964.
8. Berrier, Bobby L.; and Mercer, Charles E.: Off-Design Performance of Two Isentropic Plug Nozzles Designed for a Pressure Ratio of 16.5. NASA TN D-3852, 1967.
9. Berrier, Bobby L.: Effect of Plug and Shroud Geometry Variables on Plug-Nozzle Performance at Transonic Speeds. NASA TN D-5098, 1969.
10. Schmeer, James W.; Lauer, Rodney F., Jr.; and Berrier, Bobby L.: Performance of Blow-In-Door Ejector Nozzles Installed on a Twin-Jet Variable-Wing-Sweep Fighter Airplane Model. NASA TM X-1383, 1967.
11. Re, Richard J.; Wilmoth, Richard G.; and Runckel, Jack F.: Investigation of Effects of Afterbody Closure and Jet Interference on the Drag of a Twin-Engine Tactical Fighter. NASA TM X-1382, 1967.
12. Wilmoth, Richard G.; Norton, Harry T., Jr.; and Corson, Blake W., Jr.: Effect of Engine-Interfairing Modifications on the Performance of a Powered Twin-Jet Fighter-Airplane Model at Mach 1.20. NASA TM X-1534, 1968.

13. Mercer, Charles E.; Pendergraft, Odis C., Jr.; and Berrier, Bobby L.: Effect of Geometric Variations on Performance of a Twin-Jet Blow-In-Door Ejector Nozzle Installation. NASA TM X-1633, 1968.
14. Harris, Roy V., Jr.: An Analysis and Correlation of Aircraft Wave Drag. NASA TM X-947, 1964.
15. Rao, G. V. R.: Approximation of Optimum Thrust Nozzle Contour. ARS J., vol. 30, no. 6, June 1960, p. 561.
16. Shapiro, Ascher H.: The Dynamics and Thermodynamics of Compressible Fluid Flow. Vol. II. The Ronald Press Co., c.1954.

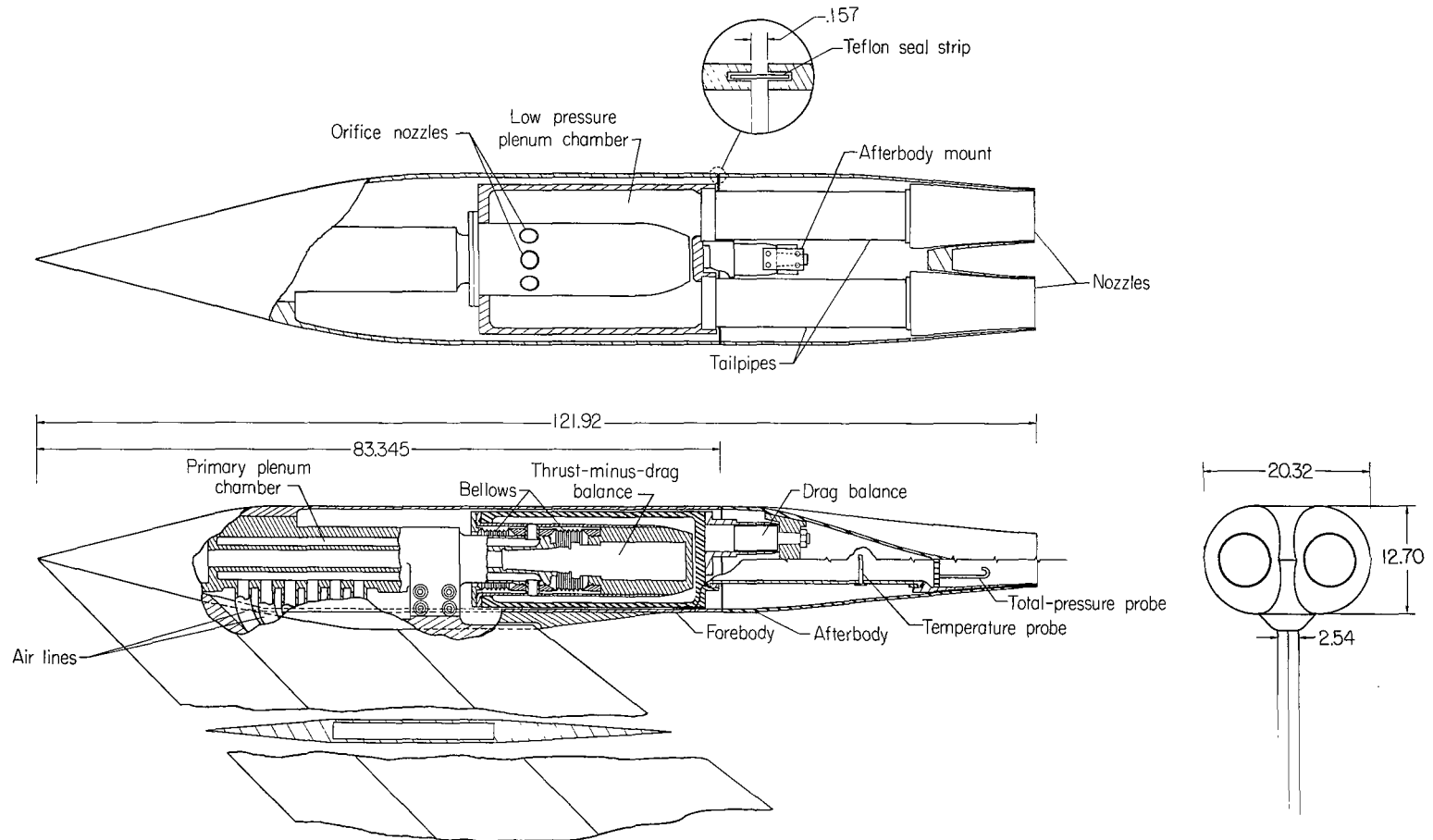


Figure 1.- Sketch of air-powered twin-jet afterbody model. All dimensions are in centimeters.

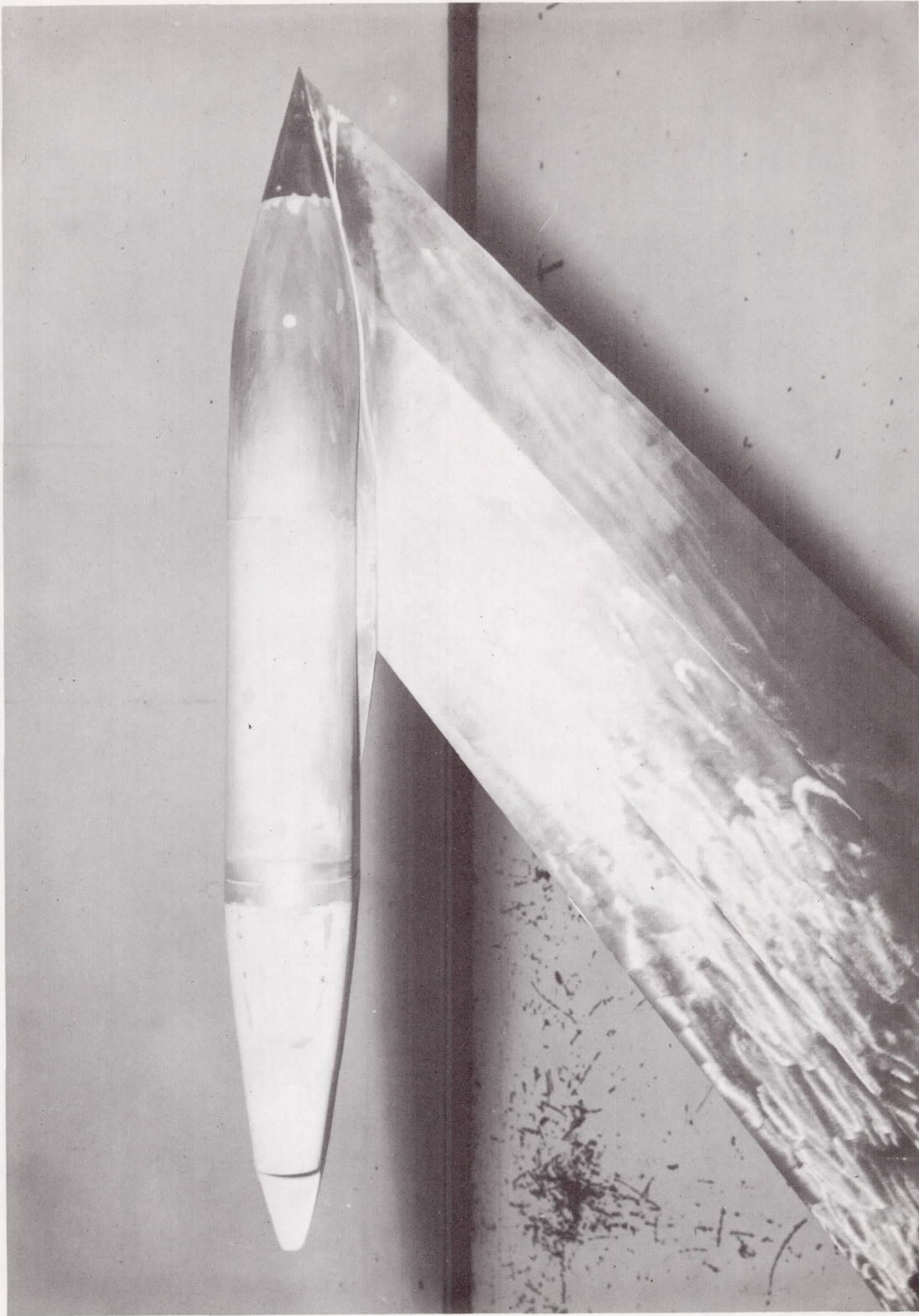


Figure 2.- Photograph of model with A-2 afterbody mounted in Langley 16-foot transonic tunnel.

L-67-8591

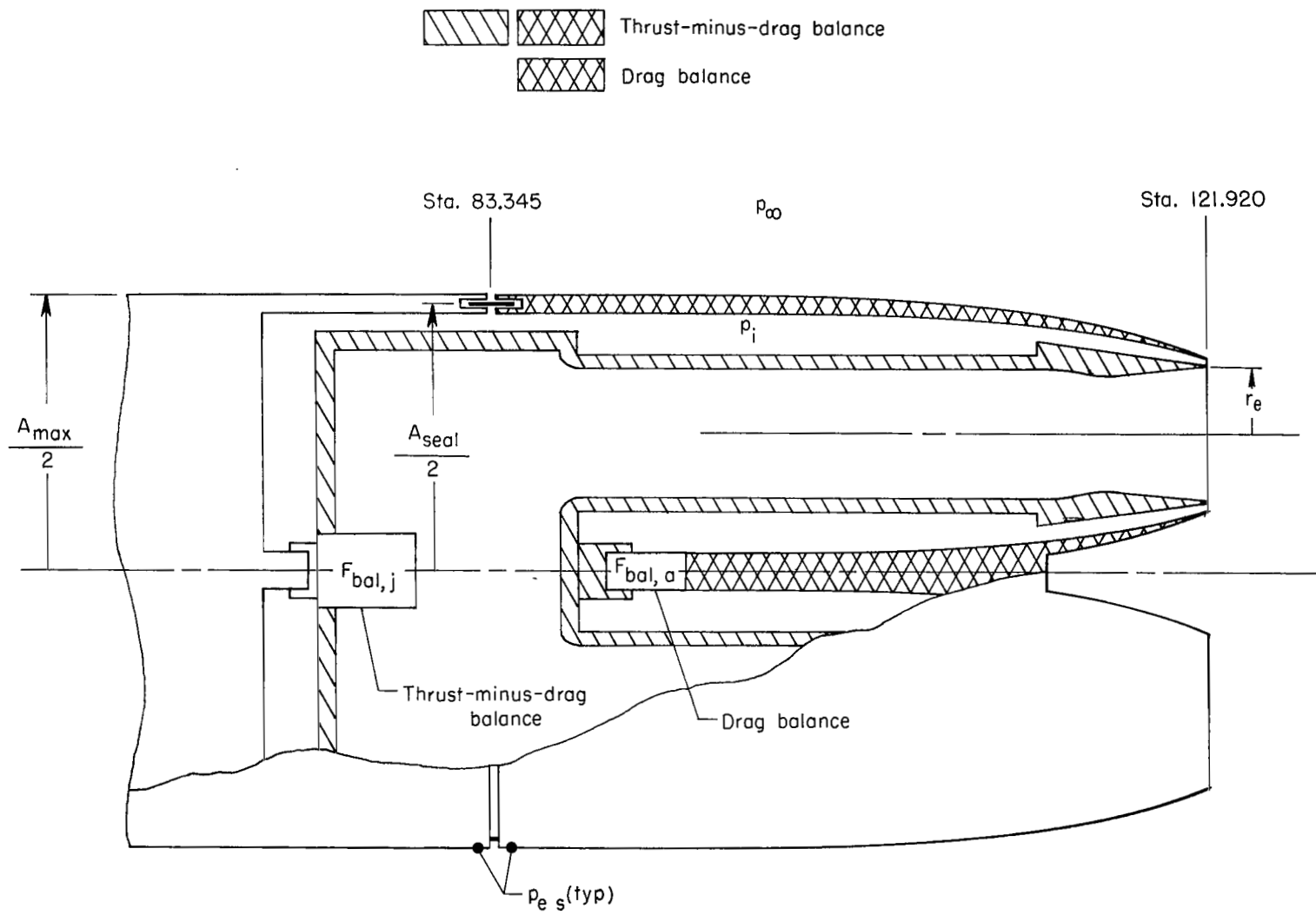
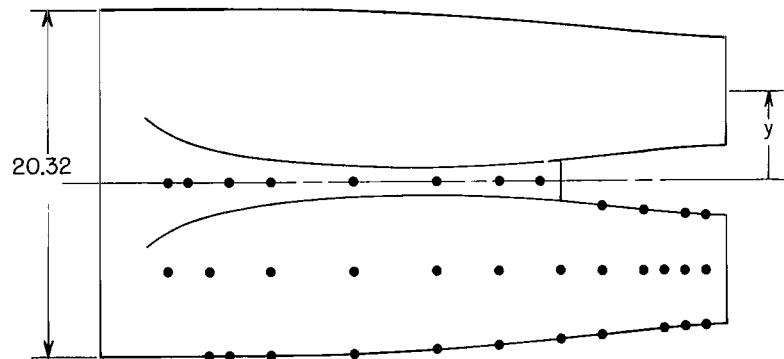
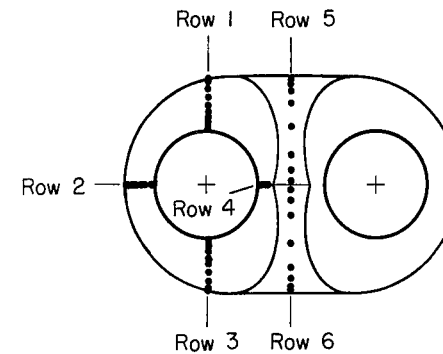
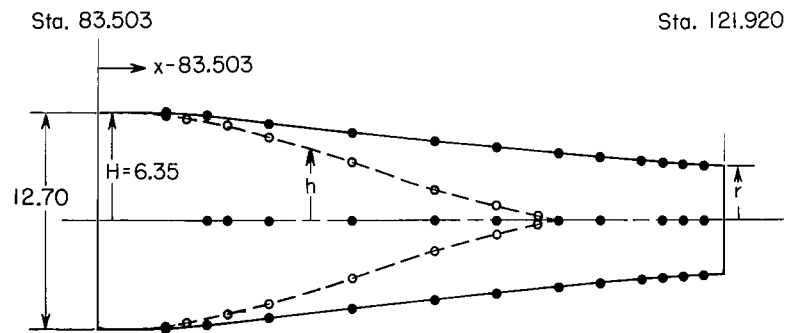


Figure 3.- Schematic sketch showing arrangement of two force balances.

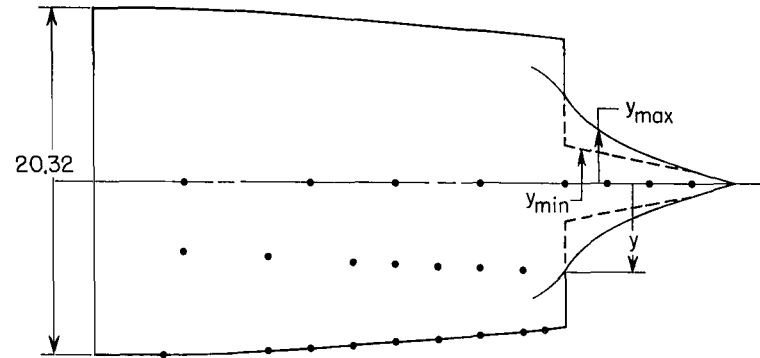


$\frac{x}{L}$	$\frac{y}{H}$	$\frac{h}{H}$	$\frac{r}{H}$	Row					
				1	2	3	4	5	6
0.685	0.600	1.000	1.000						
.708	.601	.998	.999						
.718				X	X		X	X	
.729							X	X	
.736				X	X	X			
.750	.654	.867	.946	X			X	X	
.771				X	X	X		X	X
.792	.728	.663	.862						
.812				X	X	X		X	X
.833	.788	.404	.778						
.854				X	X	X		X	X
.875	.818	.178	.700						
.886				X	X	X		X	X
.906								X	X
.917	.825	0.000	.630	X	X	X			
.937				X	X	X	X		
.958	.825	0.000	.552	X		X	X		
.969				X	X	X			
.979				X	X	X	X		
.990				X	X	X	X		
1.000	.825	0.000	.500						

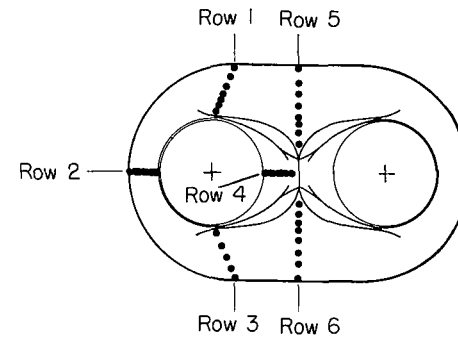
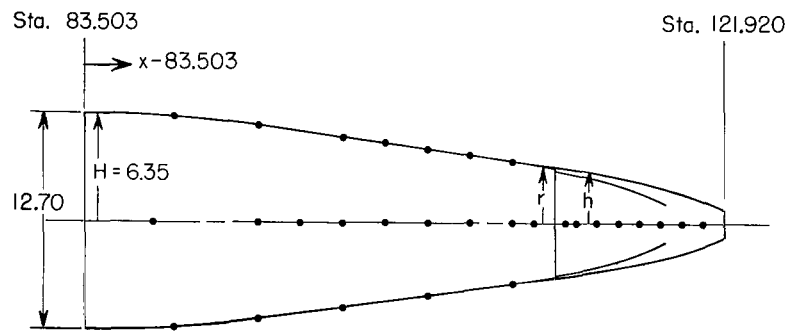


(a) Afterbody A-1.

Figure 4.- Sketch giving geometry and orifice locations of afterbody configurations. All dimensions are in centimeters.

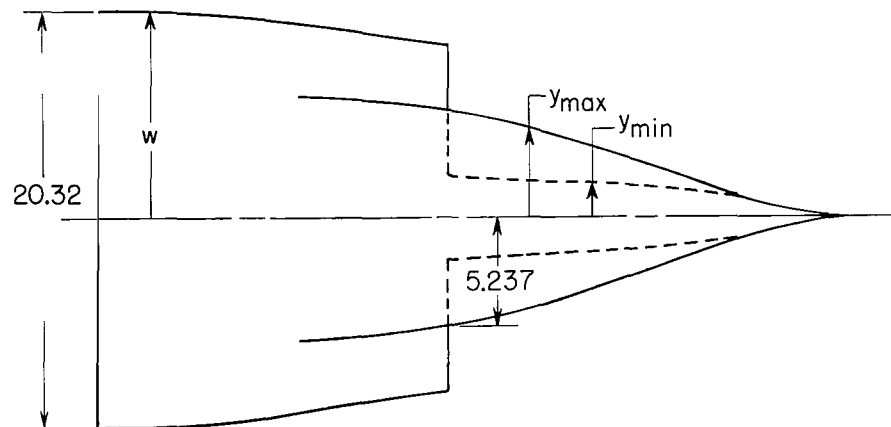


$\frac{x}{L}$	$\frac{r}{H}$	$\frac{h}{H}$	$\frac{y}{H}$	$\frac{y_{\max}}{H}$	$\frac{y_{\min}}{H}$	Row					
						1	2	3	4	5	6
0.685	1.000	1.000	0.600								
.708	.996	.996	.604								
.719							X				
.729	.970	.970	.628			X		X		X	X
.771	.890	.890	.672			X	X	X			
.792	.842	.842	.694				X			X	X
.813	.791	.791	.716			X	X	X			
.833	.736	.736	.738			X	X			X	X
.854	.680	.680	.760			X	X	X			
.875	.623	.623	.782			X	X			X	X
.896	.565	.562	.804			X	X	X			
.906							X				
.917	.500	.518	.825	0.800	0.340					X	X
.922										X	
.927										X	
.938		.460		.448	.272				X	X	X
.948									X		
.958		.384		.260	.200				X	X	X
.969									X		
.979		.280		.122	.122				X	X	X
.990									X		
1.000		.132		0.000	0.000						



(b) Afterbody A-2.

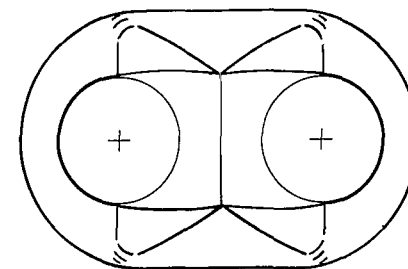
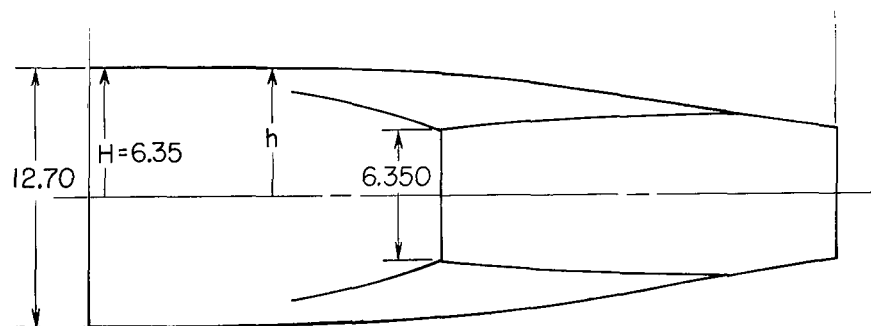
Figure 4.- Continued.



$\frac{x}{L}$	$\frac{h}{H}$	$\frac{w}{H}$	$\frac{y_{max}}{H}$	$\frac{y_{min}}{H}$
0.685	1.000	1.600		
.703	1.000	1.600		
.750	.988	1.544		
.792	.984	1.440		
.833	.950	1.326	0.824	0.324
.875	.850		.660	.271
.917	.740		.410	.236
.958	.620		.140	.140
1.000	.500		.000	.000

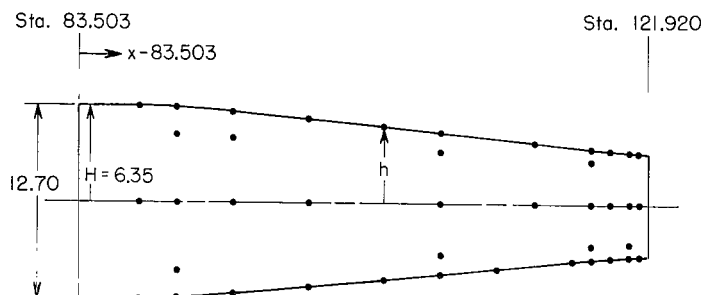
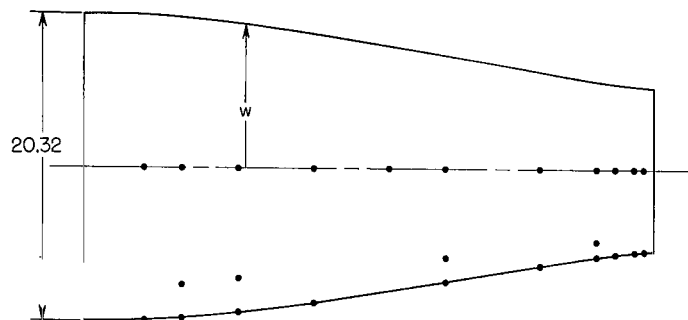
Sta. 83.503
→ x-83.503

Sta. 121.920



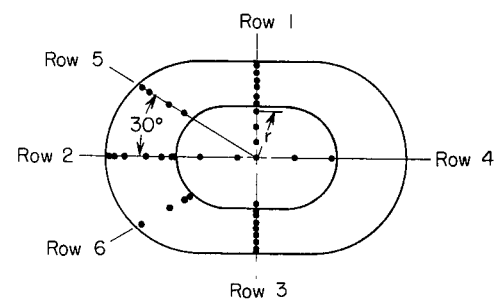
(c) Afterbody A-3.

Figure 4.- Continued.



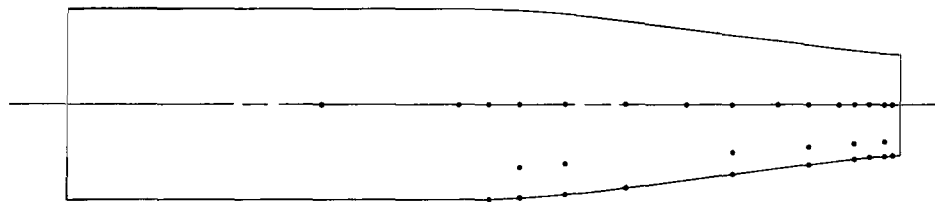
$\frac{w}{z}$	$\frac{h}{H}$	$\frac{w}{H}$	Row					$\frac{x}{z}$	$\frac{h}{H}$	$\frac{w}{H}$	Row				
			1	2	3	5	6				1	2	3	5	6
0.685	1.000	1.600						0.917	0.671	1.073			X		
.718			X	X	X			.938	.628	1.005	X	X			
.729	.986	1.578						.958	.588	.941			X		
.740			X	X	X	X	X	.969			X	X	X	X	X
.771	.938	1.501	X	X	X	X		.979	.553	.885	X	X	X		
.813	.874	1.398	X	X	X			.990			X	X	X		
.854	.798	1.276	X	X				.995			X	X	X		
.885			X	X	X	X	X	1.000	.532	.851					

Base pressures		
$\frac{r}{H}$	Row 2-4	Row 3-1
-0.60	X	
-0.48		X
-0.20	X	
0	X	X
.16		X
.32		X
.40	X	
.48		X
.80	X	



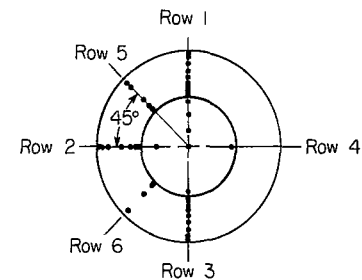
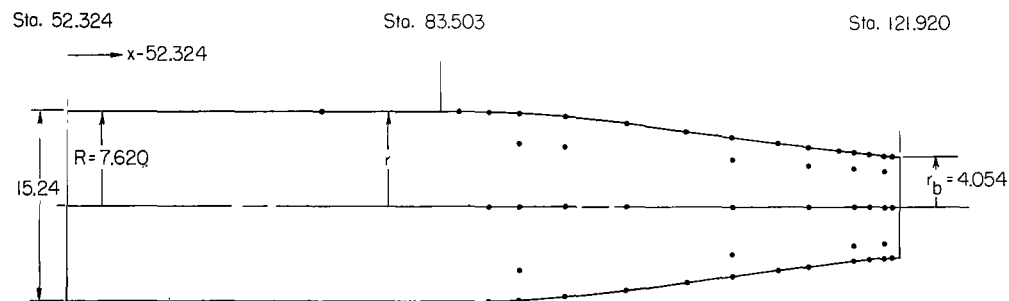
(d) Twin-jet reference body.

Figure 4.- Continued.



$\frac{x}{L}$	$\frac{r}{R}$	Row						$\frac{x}{L}$	$\frac{r}{R}$	Row					
$\frac{x}{L}$	$\frac{r}{R}$	1	2	3	5	6		$\frac{x}{L}$	$\frac{r}{R}$	1	2	3	5	6	
0.429	1.000							0.885	0.734	X	X	X	X	X	
.604	1.000	X						.917	.671	X		X			
.685	1.000							.938	.628	X	X	X	X		
.698	1.000	X						.958	.588	X					
.719	.994	X	X	X				.969	.569	X	X	X	X	X	
.740	.976	X	X	X	X	X		.979	.553	X	X	X			
.771	.938	X	X	X	X			.990	.540	X	X	X	X	X	
.813	.874	X	X	X				.995	—	X	X	X			
.854	.797	X		X				1.000	.532						

Base pressures		
$\frac{r}{r_b}$	Row 2-4	Row 3-1
-0.877		X
-0.658	X	
0	X	X
.313		X
.627		X
.877	X	X



(e) Axisymmetric reference body.

Figure 4.- Concluded.

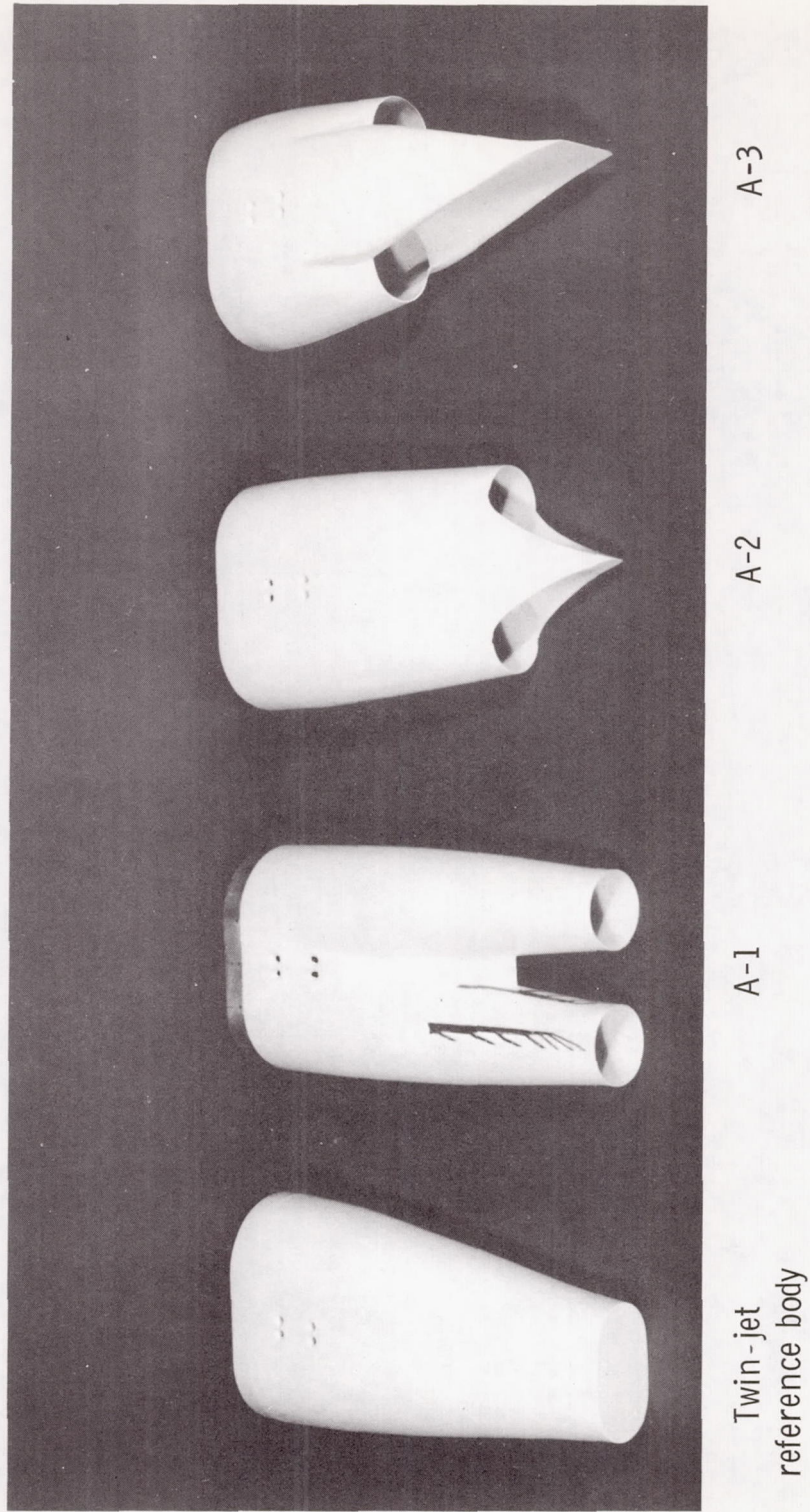


Figure 5.- Photograph of afterbody configurations.

L-68-3471

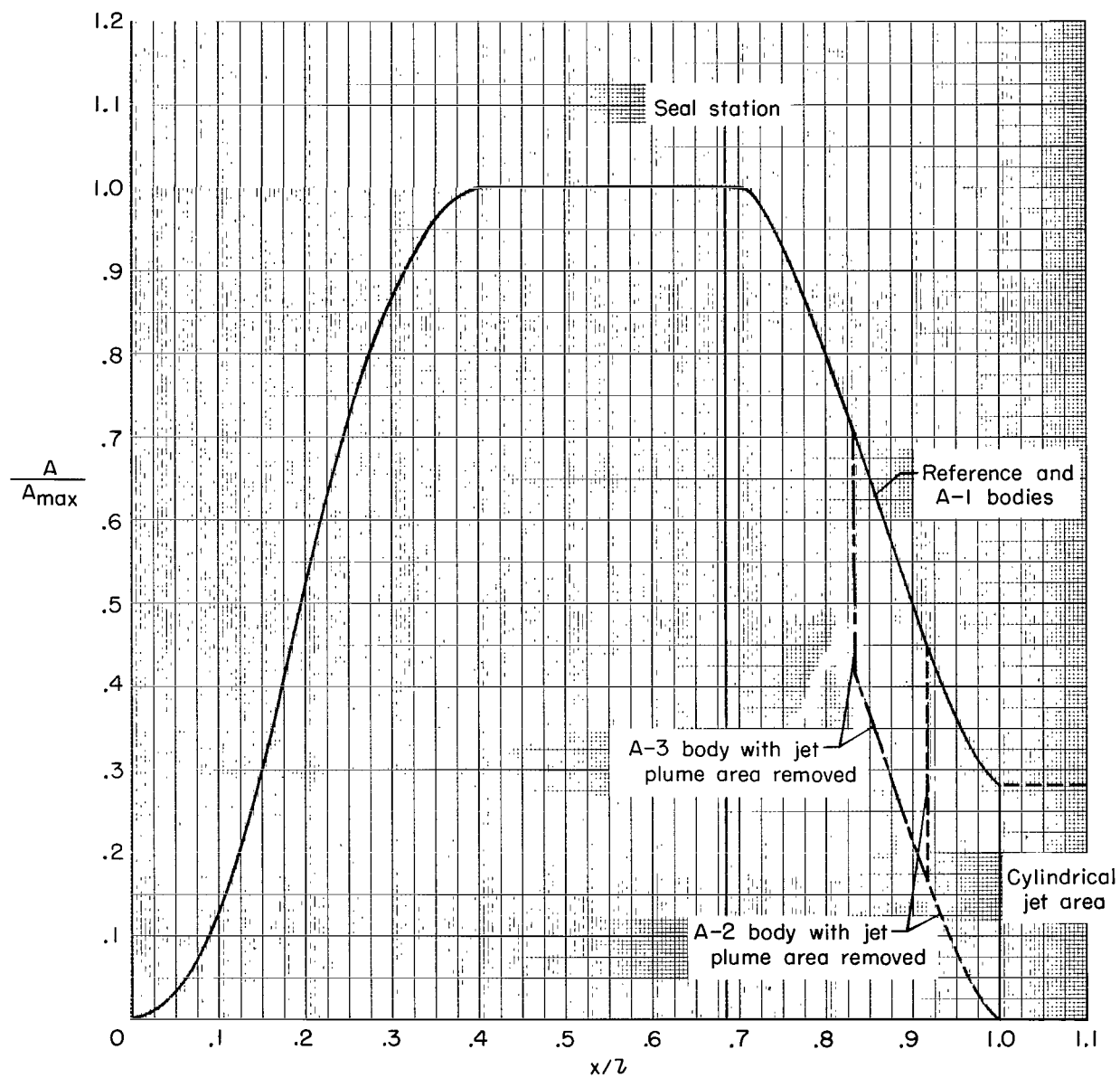
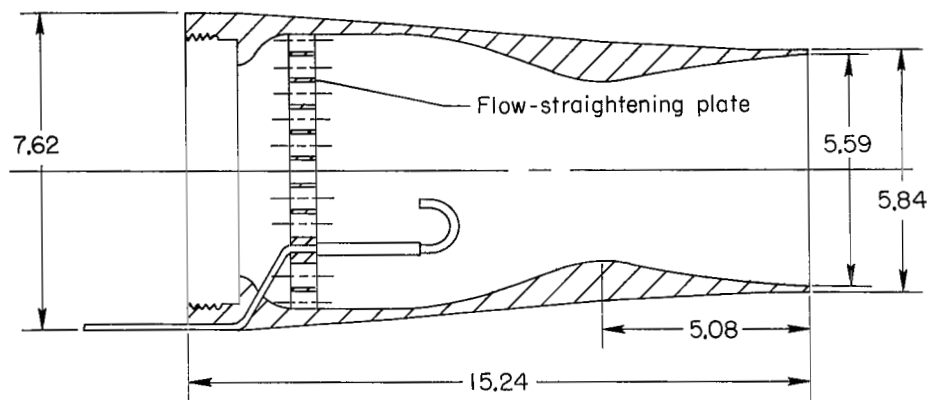
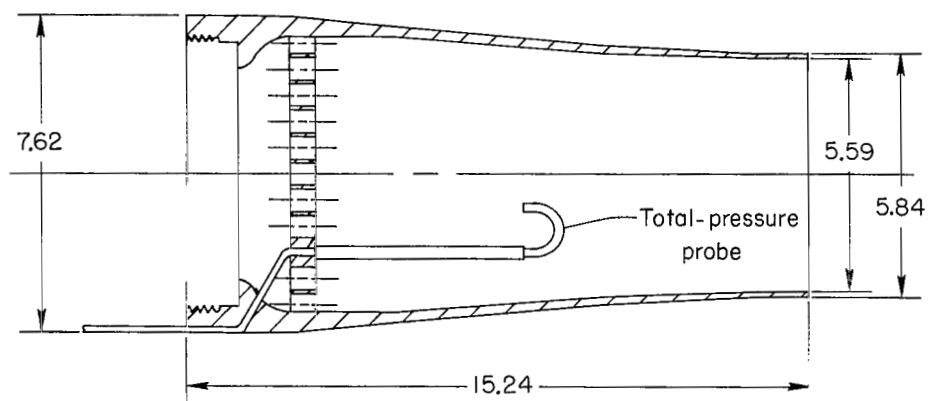
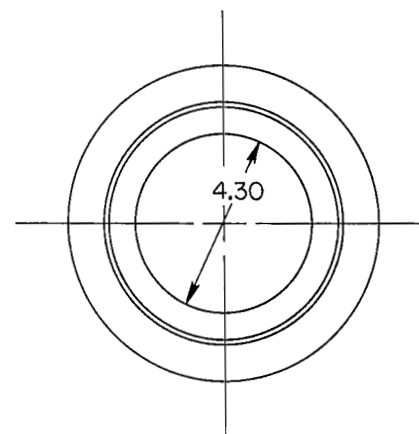


Figure 6.- Area distribution of twin-jet model with various afterbodies. $A_{\max} = 223.562 \text{ cm}^2$.



(a) Convergent-divergent nozzle ($A_e/A_t = 1.688$).



(b) Convergent nozzle ($A_e/A_t = 1.00$).

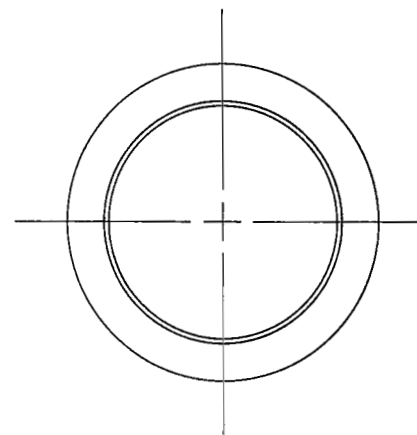
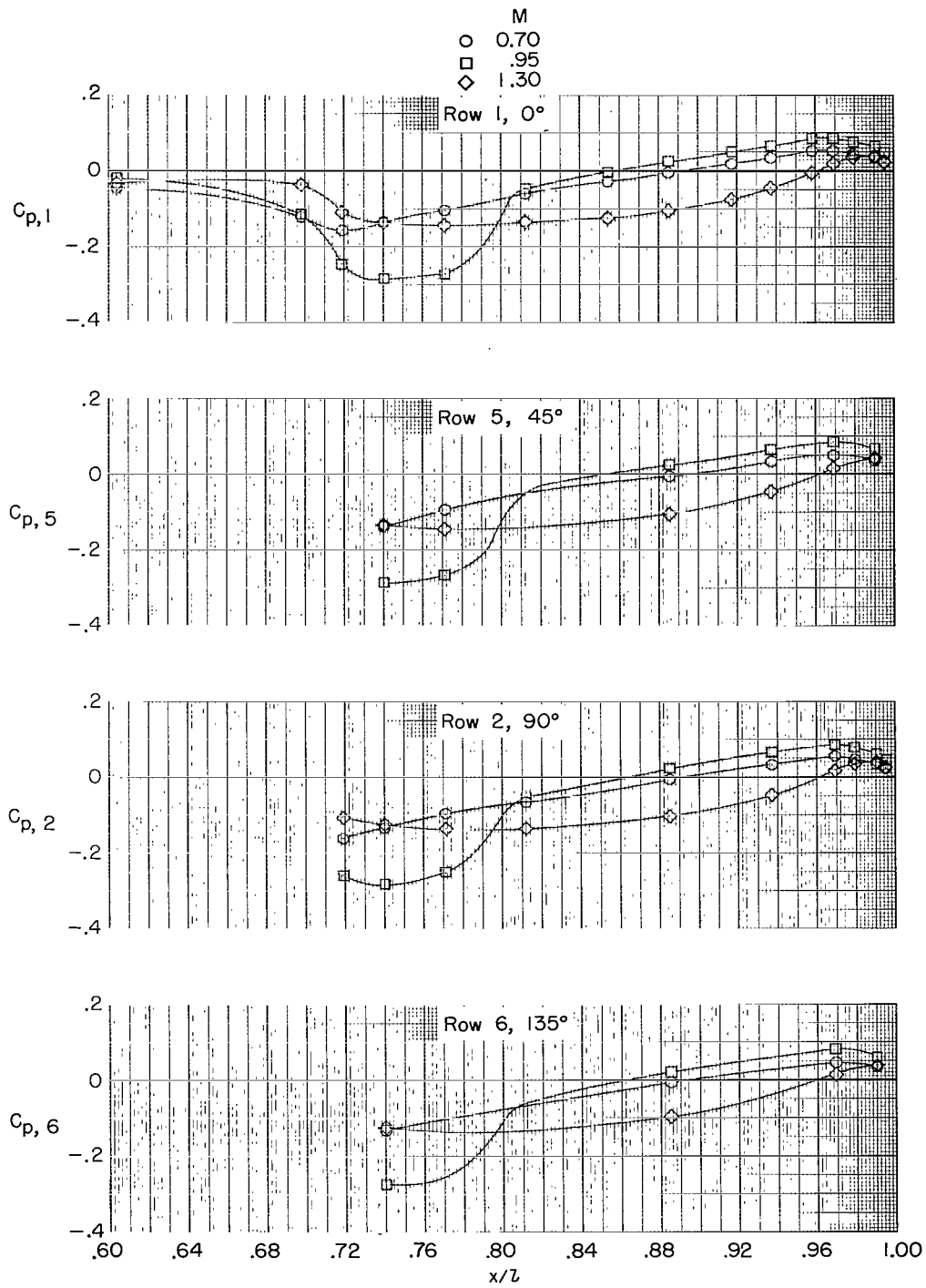
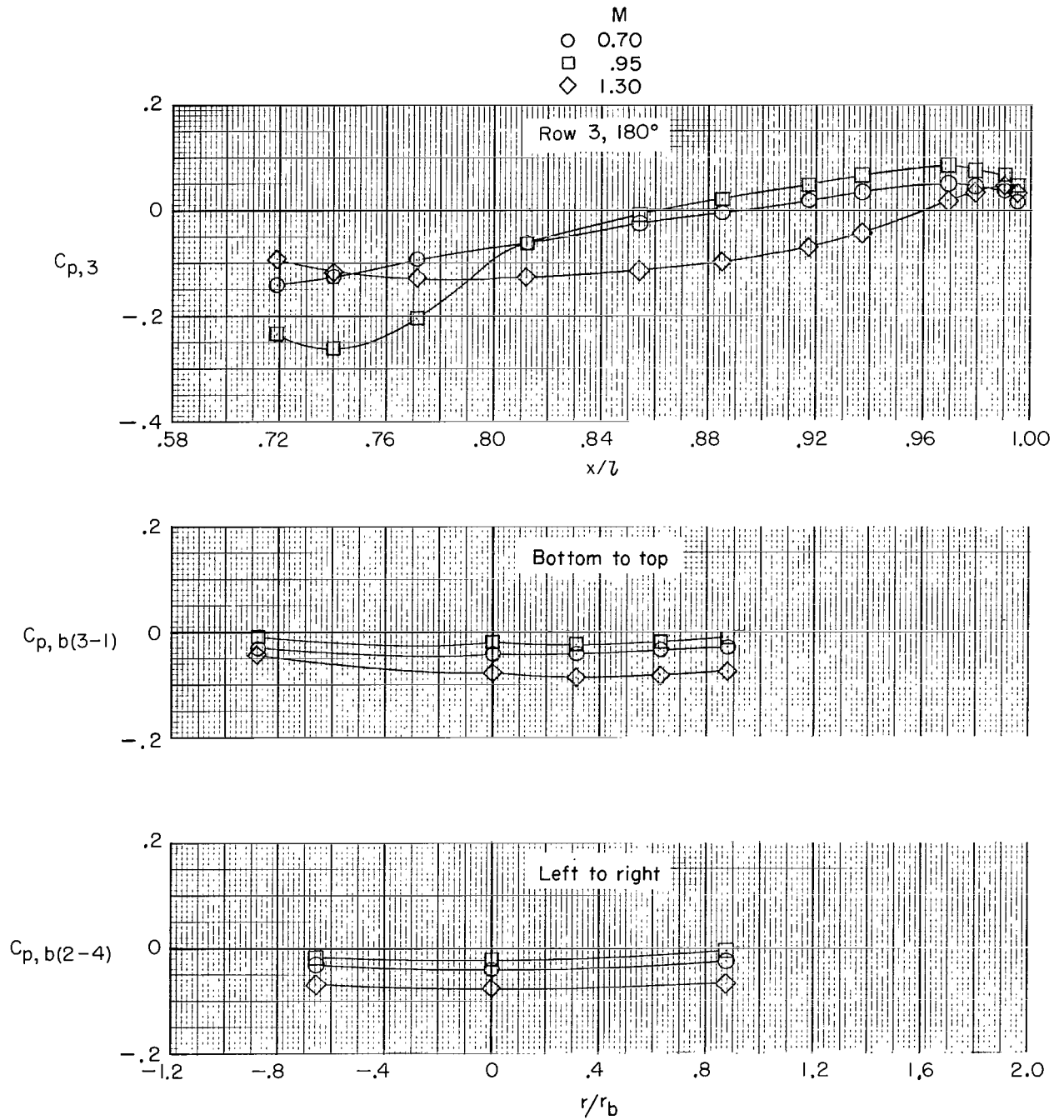


Figure 7.- Sketch of nozzle configurations. All dimensions are in centimeters.



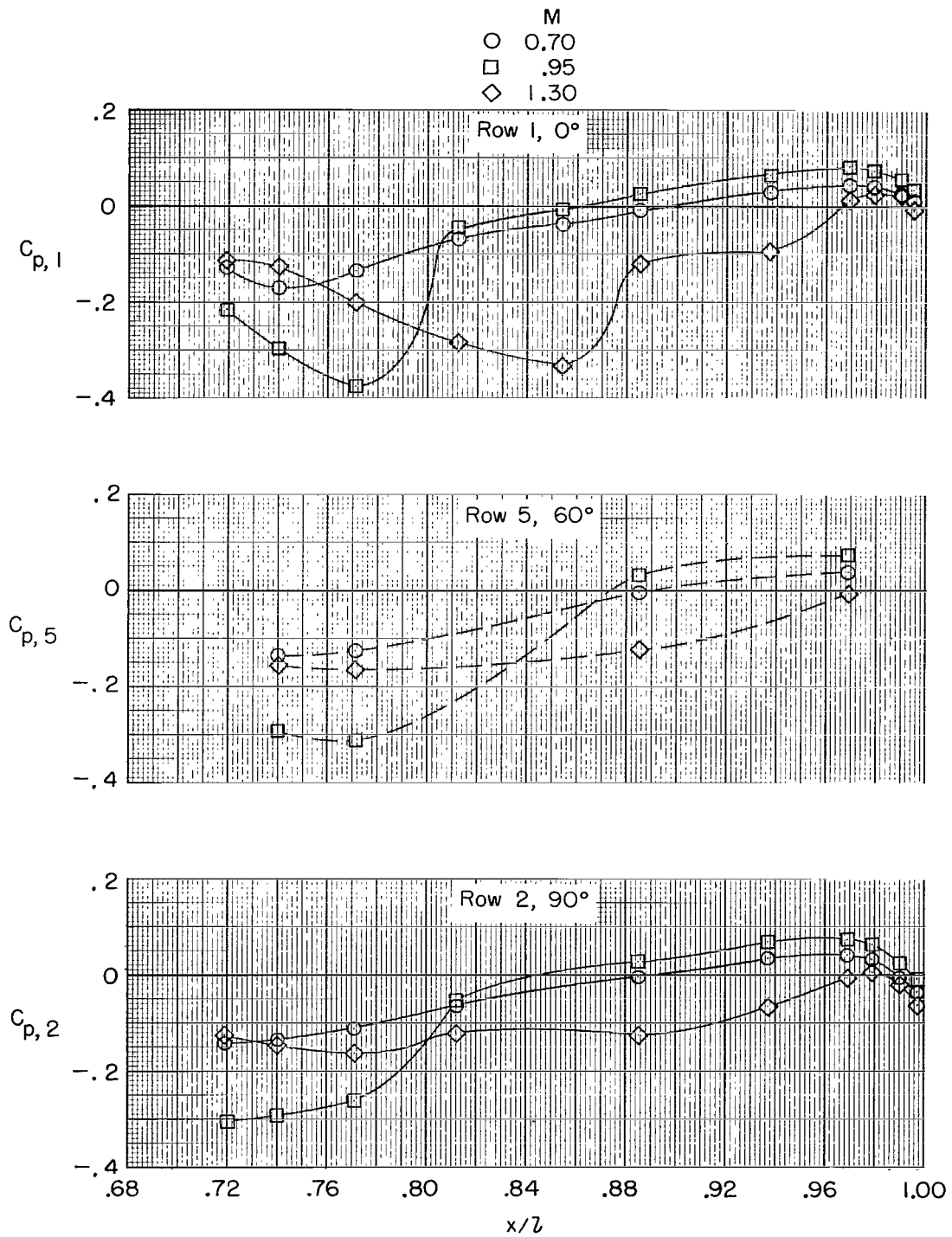
(a) 0° to 135° .

Figure 8.- Pressure distributions on axisymmetric reference body at several Mach numbers.



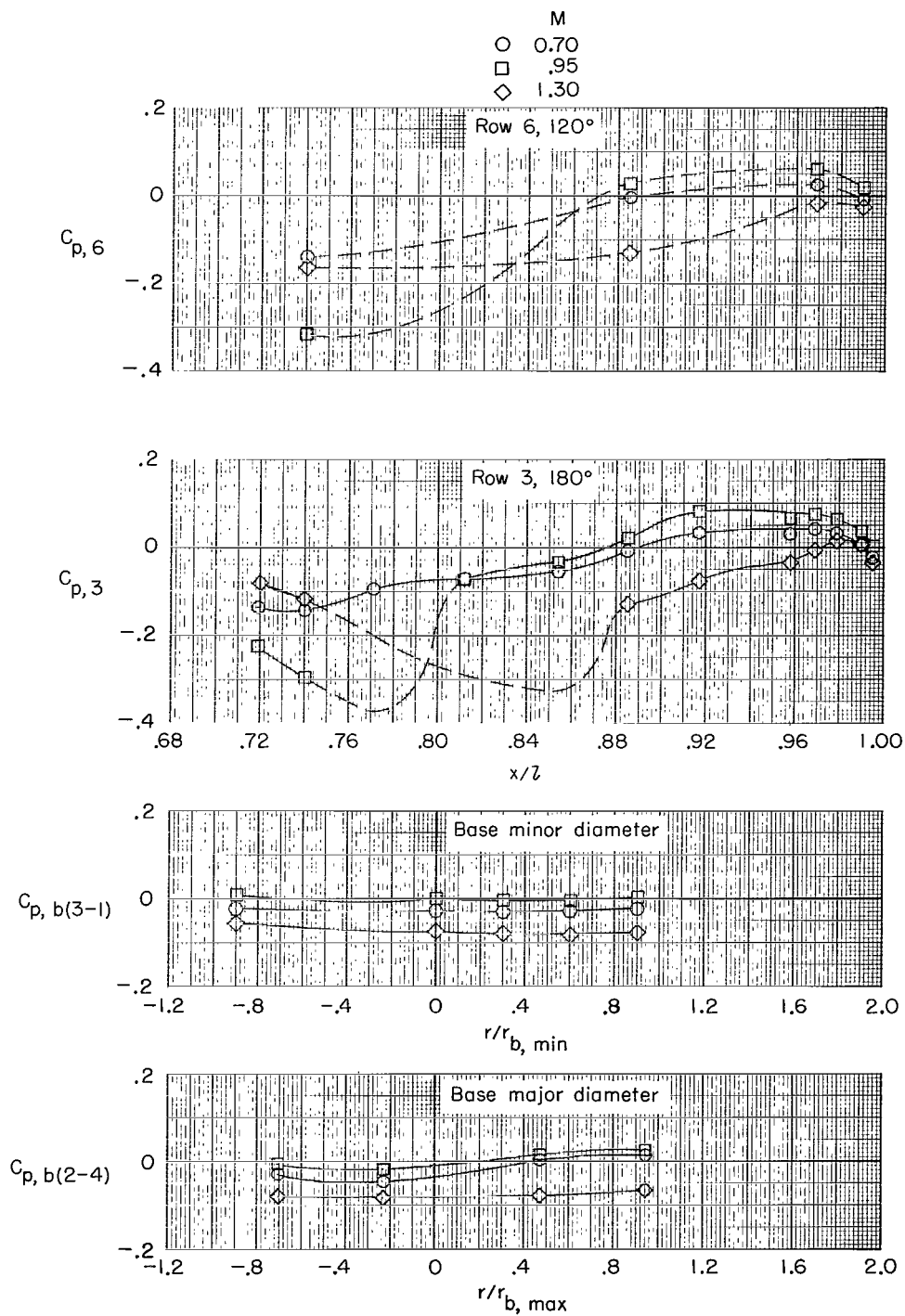
(b) 180° and base.

Figure 8.- Concluded.



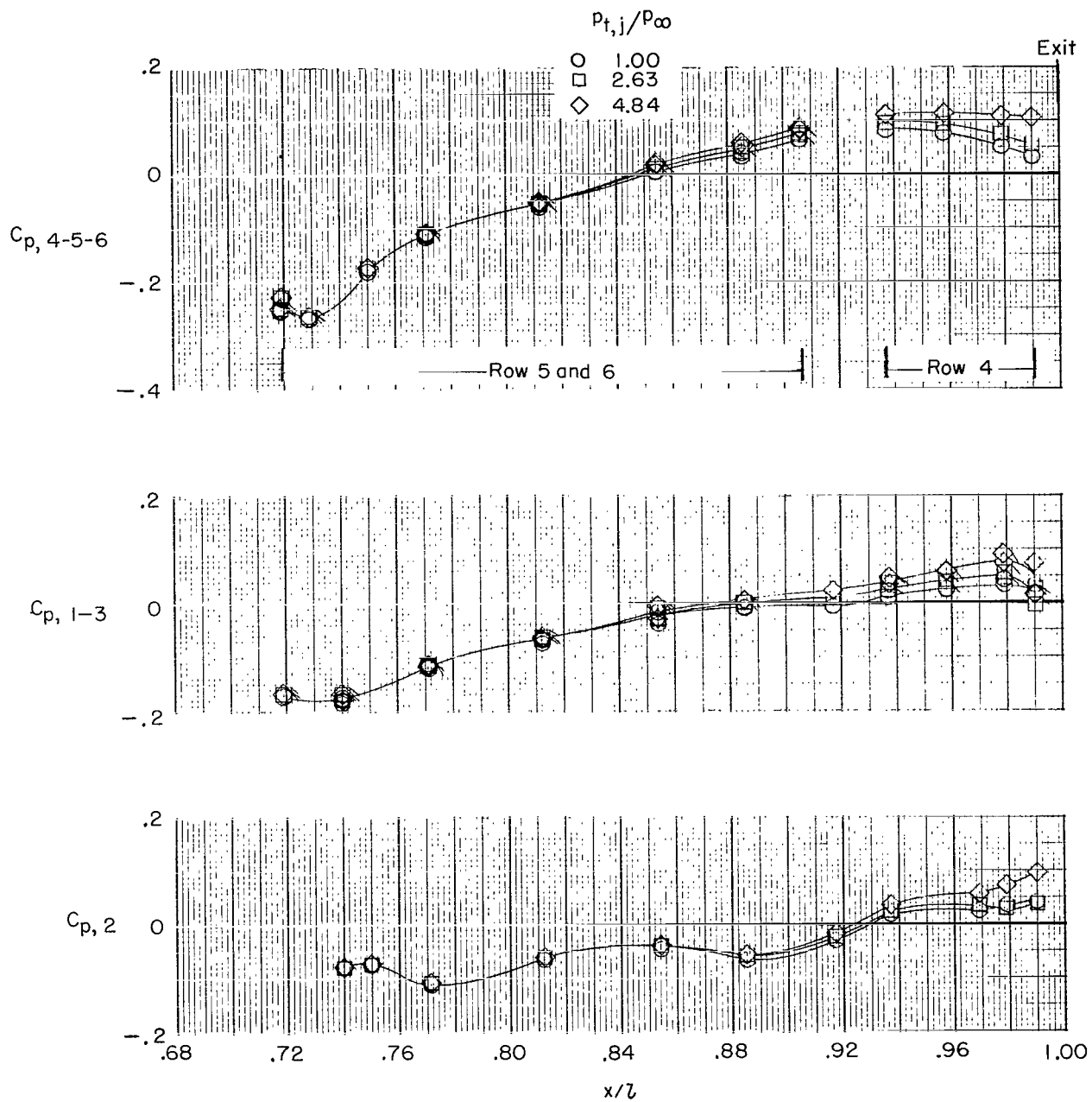
(a) 0° to 90° .

Figure 9.- Pressure distributions on twin-jet reference body at several Mach numbers.



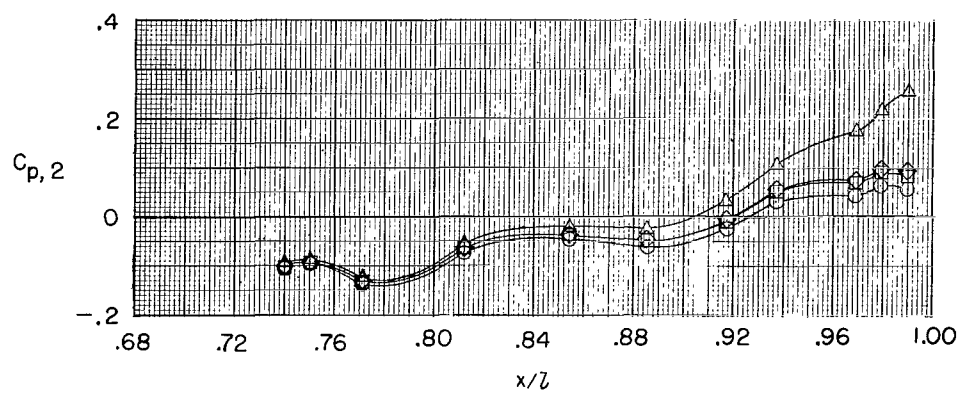
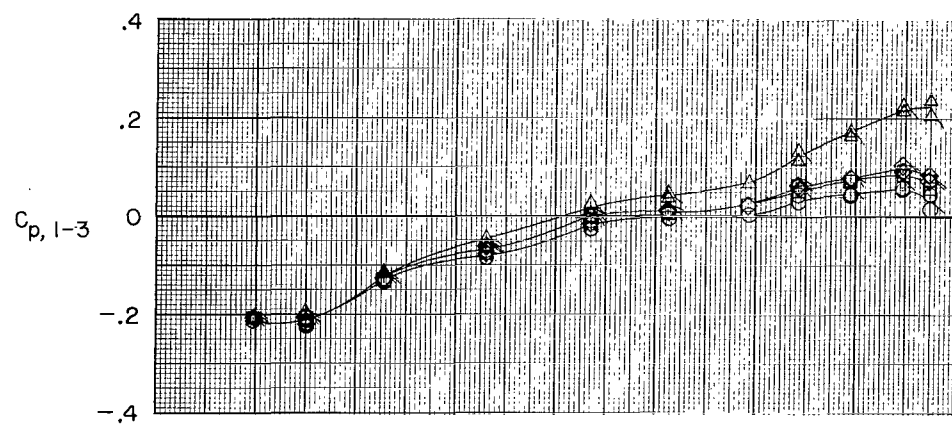
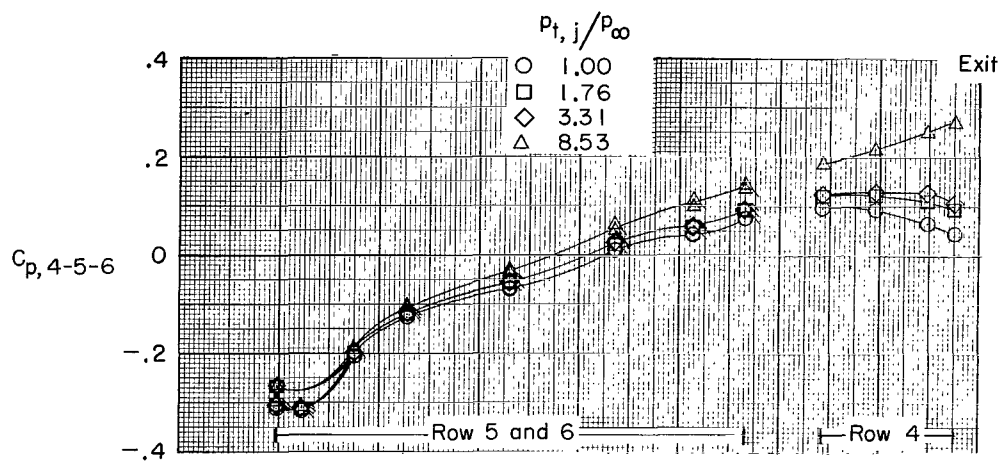
(b) 120°, 180°, and base.

Figure 9.- Concluded.



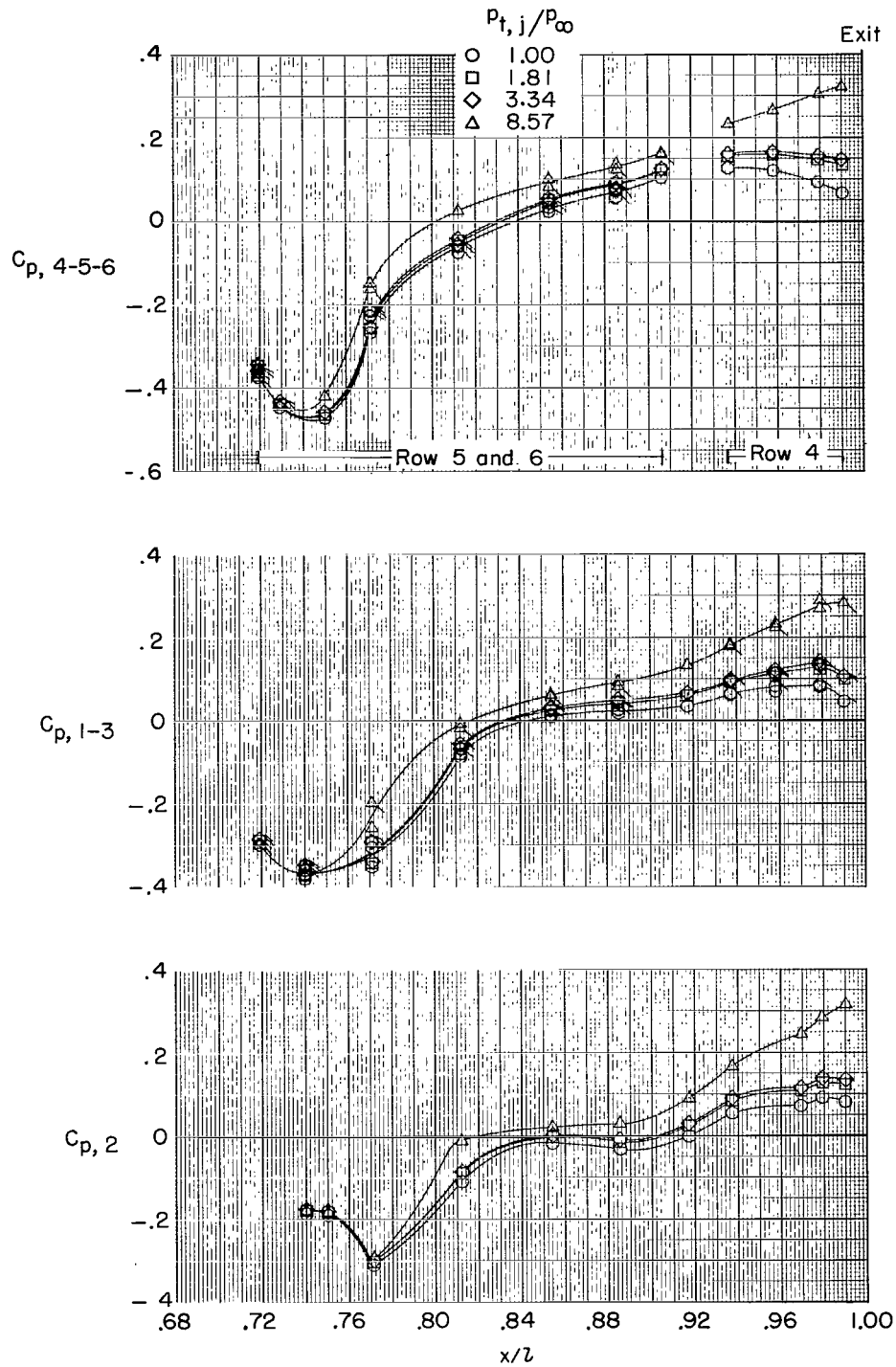
(a) $M = 0.50$.

Figure 10.- Afterbody pressure distributions for A-1 afterbody. Convergent nozzles. Flagged symbols denote bottom row.



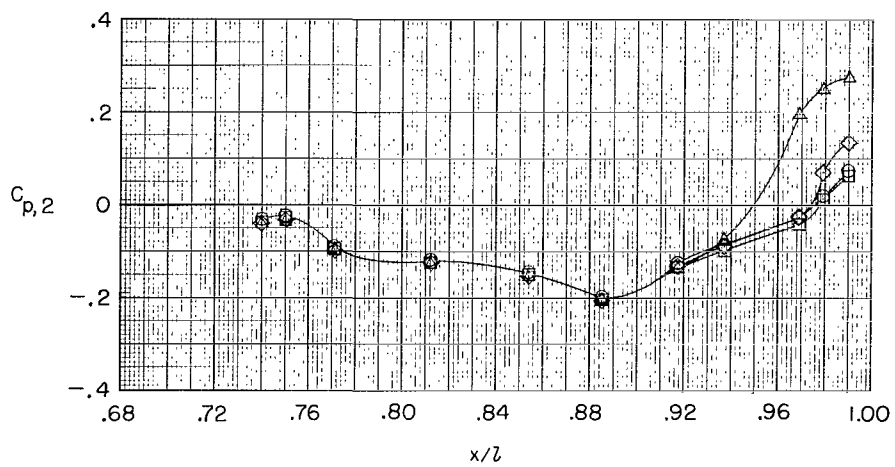
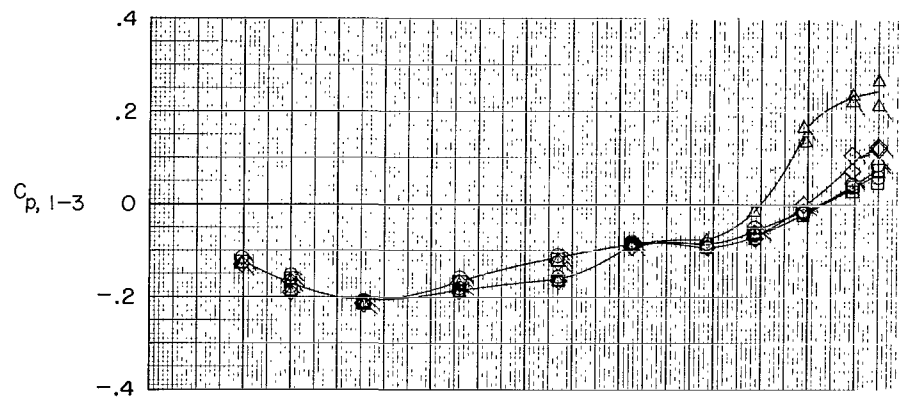
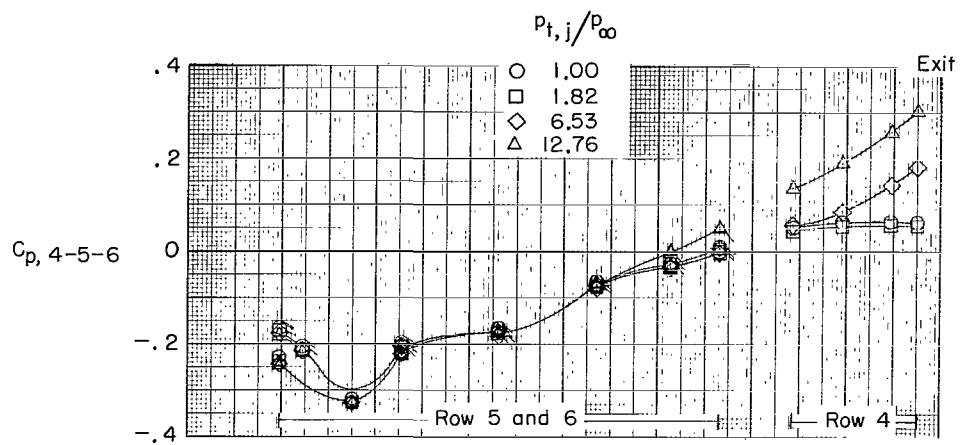
(b) $M = 0.80$.

Figure 10.- Continued.



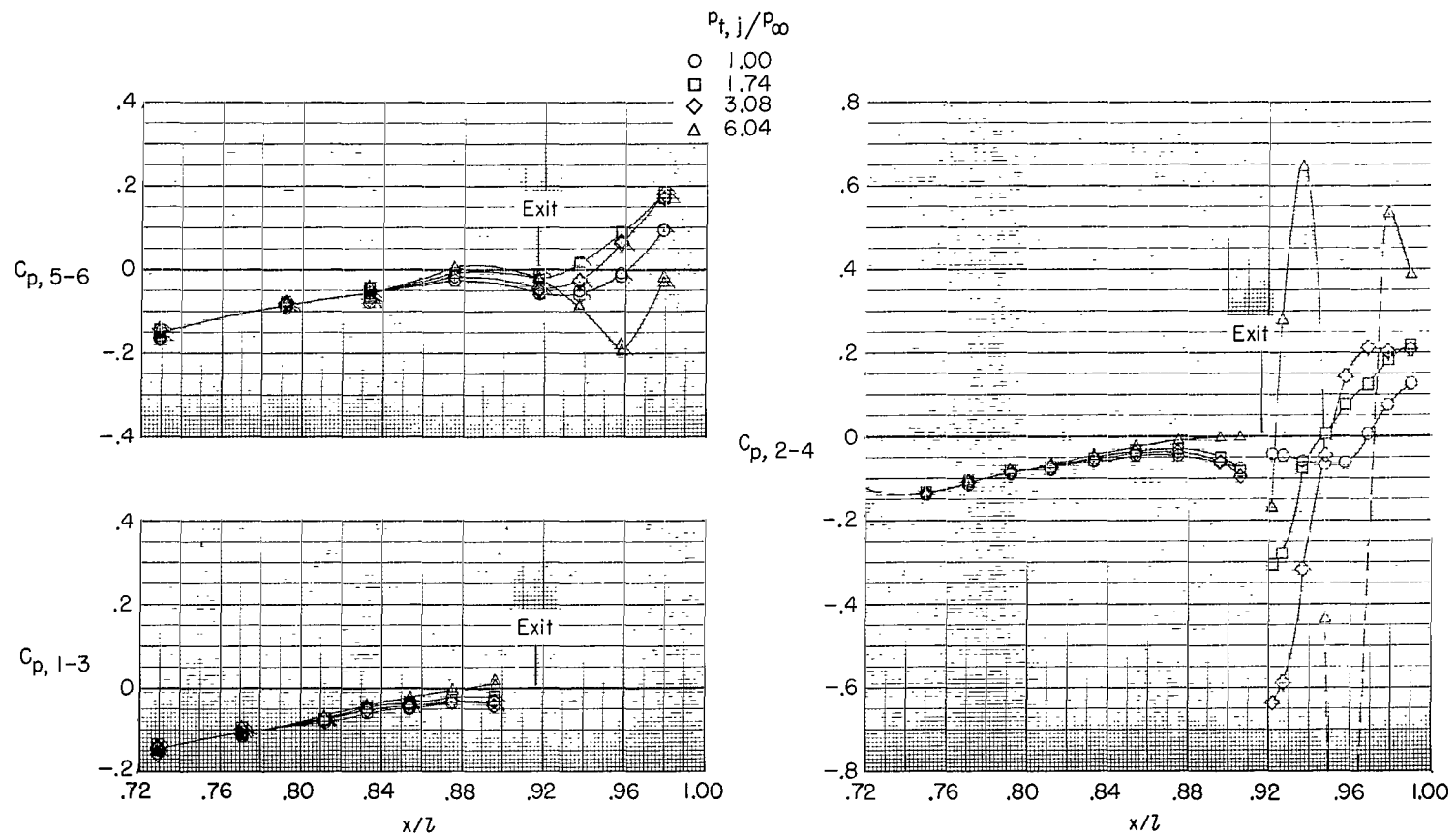
(c) $M = 0.95$.

Figure 10.- Continued.



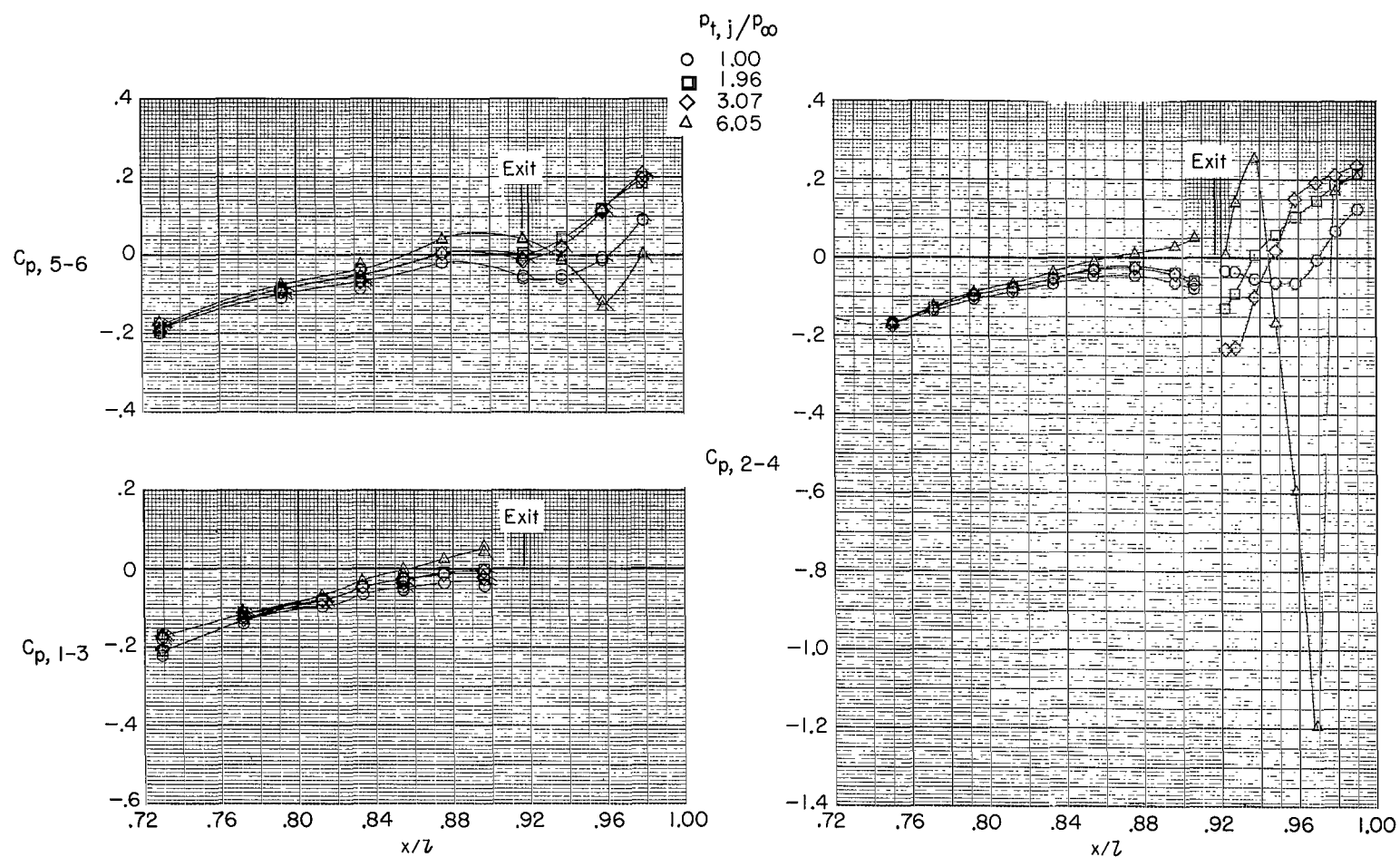
(d) $M = 1.30$.

Figure 10.- Concluded.



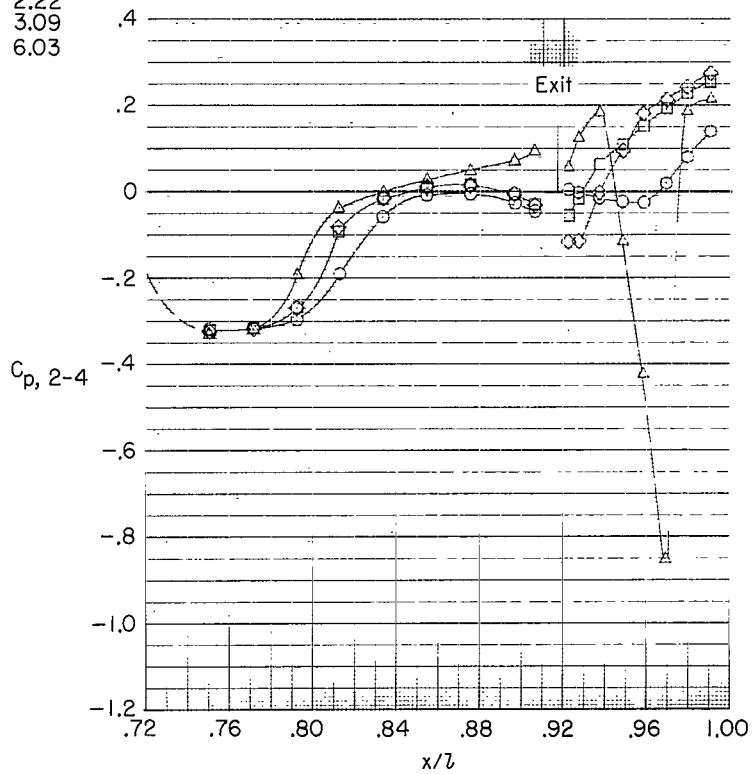
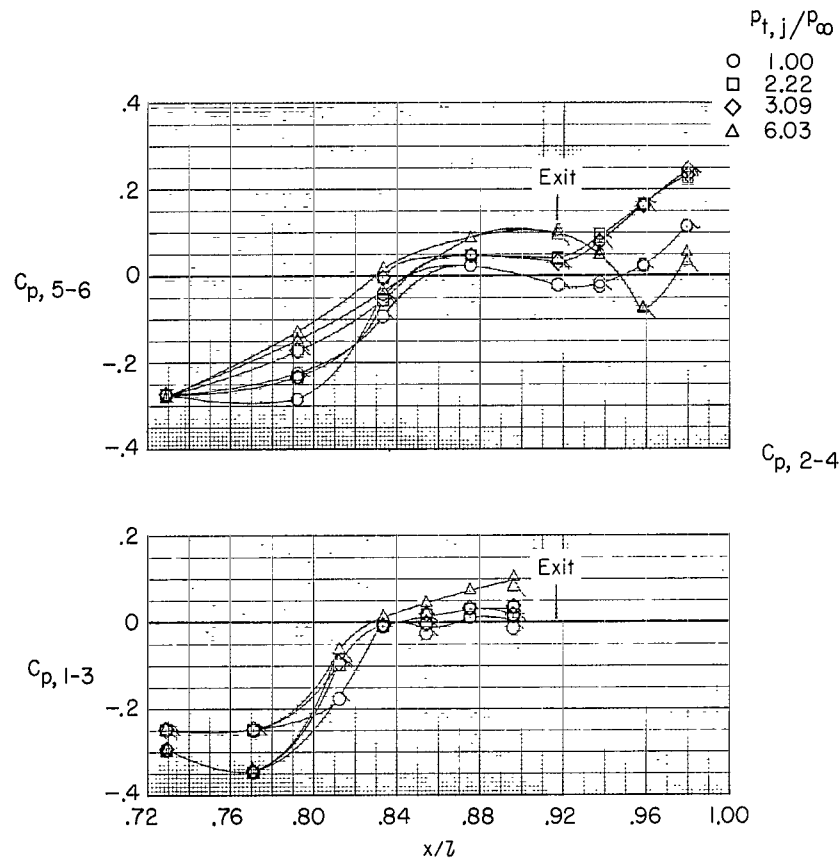
(a) $M = 0.50$.

Figure 11.- Afterbody pressure distributions for A-2 afterbody. Convergent nozzles. Flagged symbols indicate bottom row.



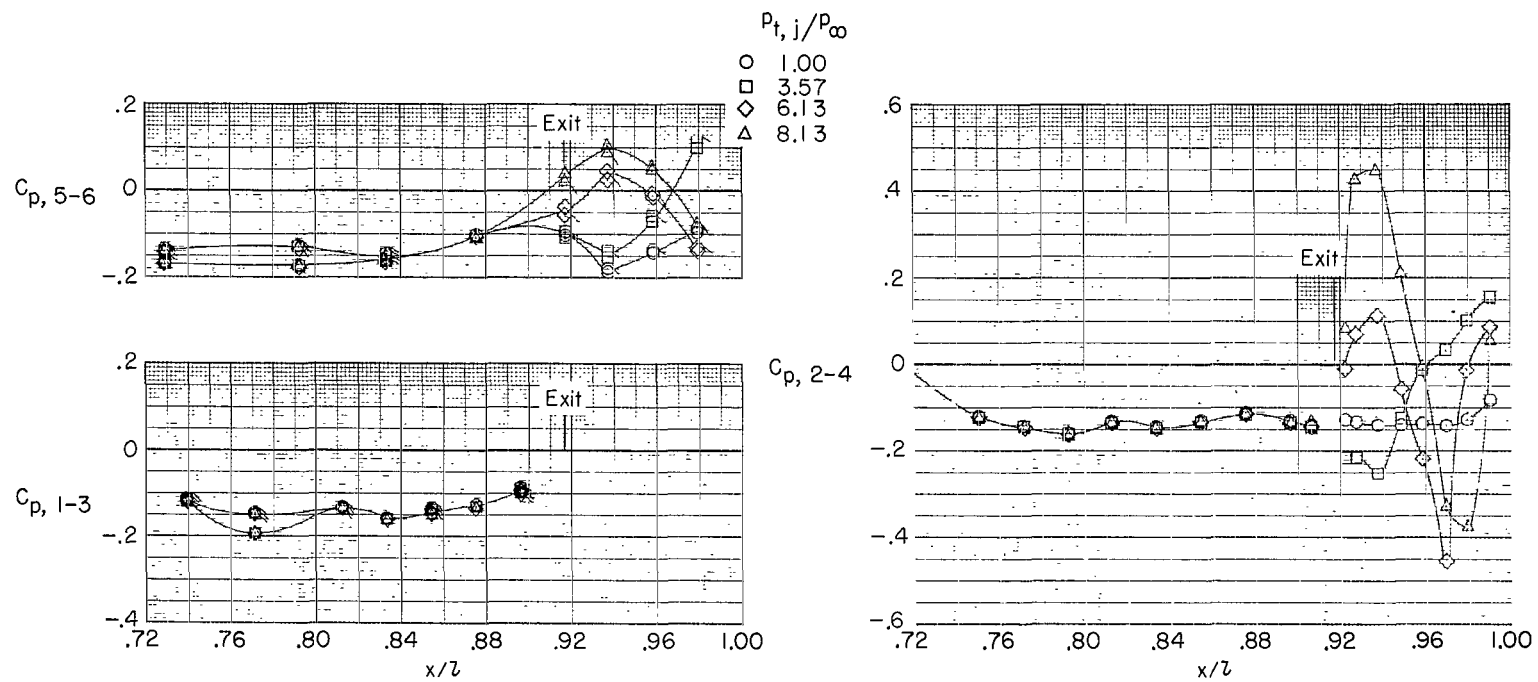
(b) $M = 0.80$.

Figure 11.- Continued.



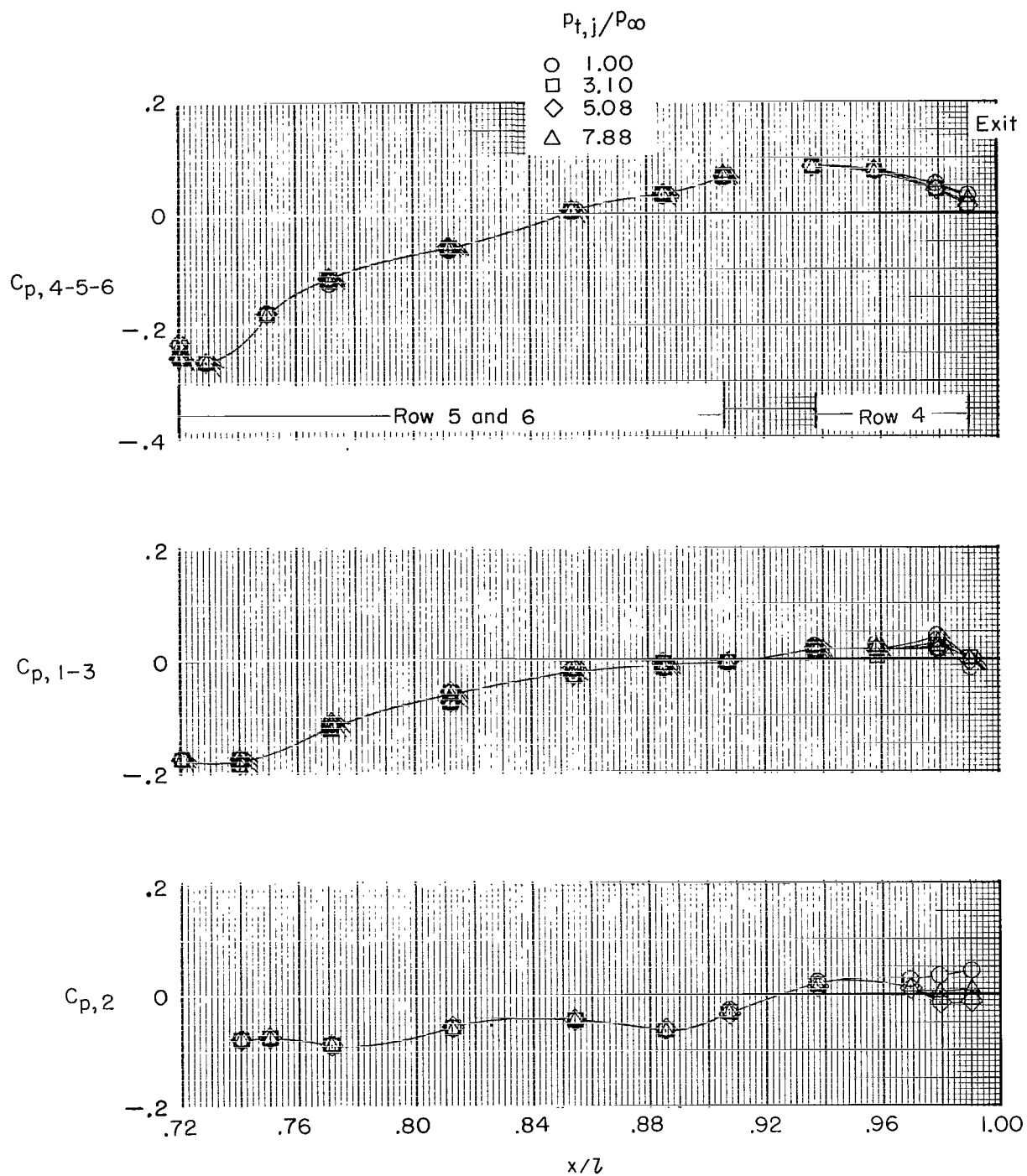
(c) $M = 0.95$.

Figure 11.- Continued.



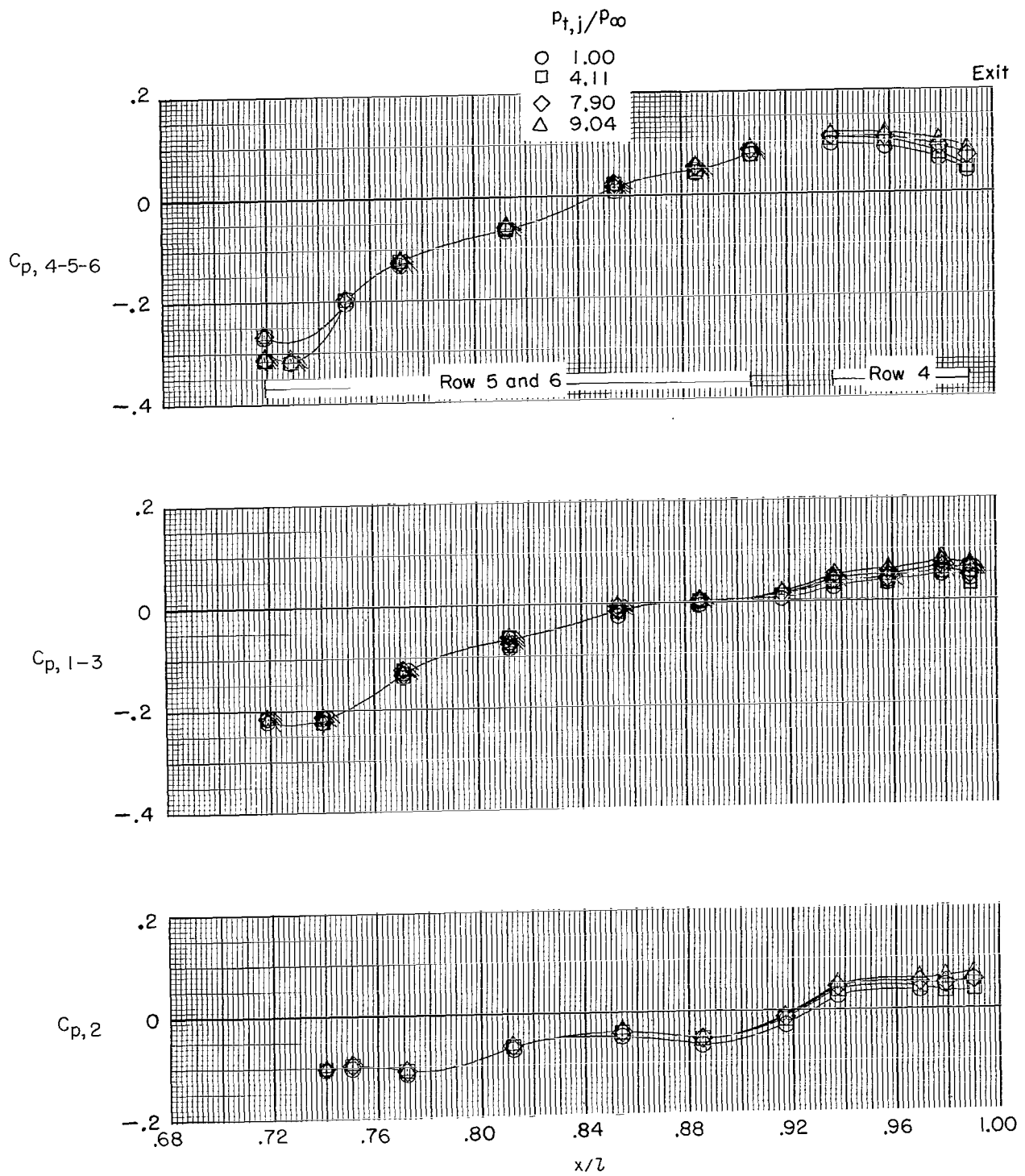
(d) $M = 1.30$.

Figure 11.- Concluded.



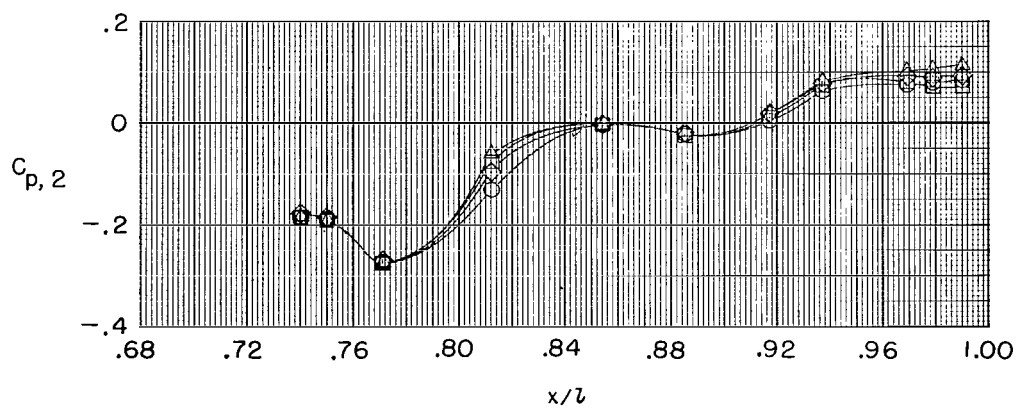
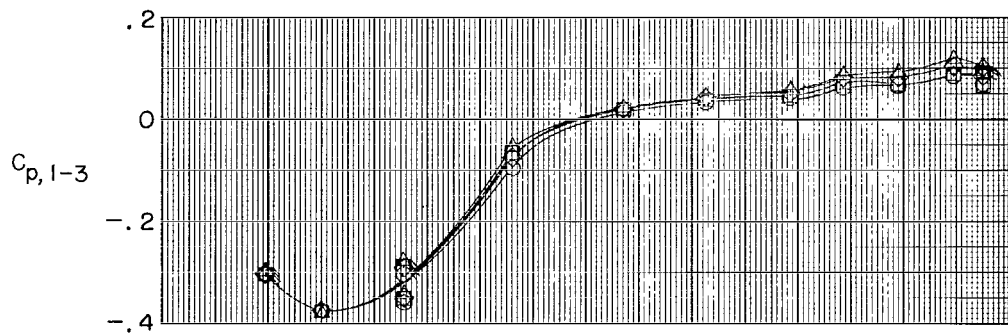
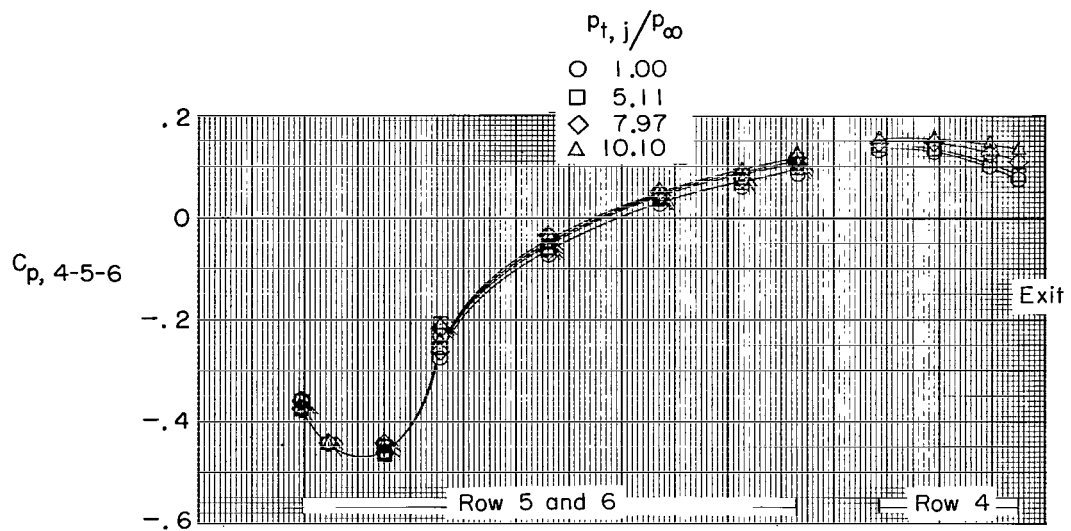
(a) $M = 0.50$.

Figure 12.- Afterbody pressure distributions for A-1 afterbody. Convergent-divergent nozzles. Flagged symbols indicate bottom row.



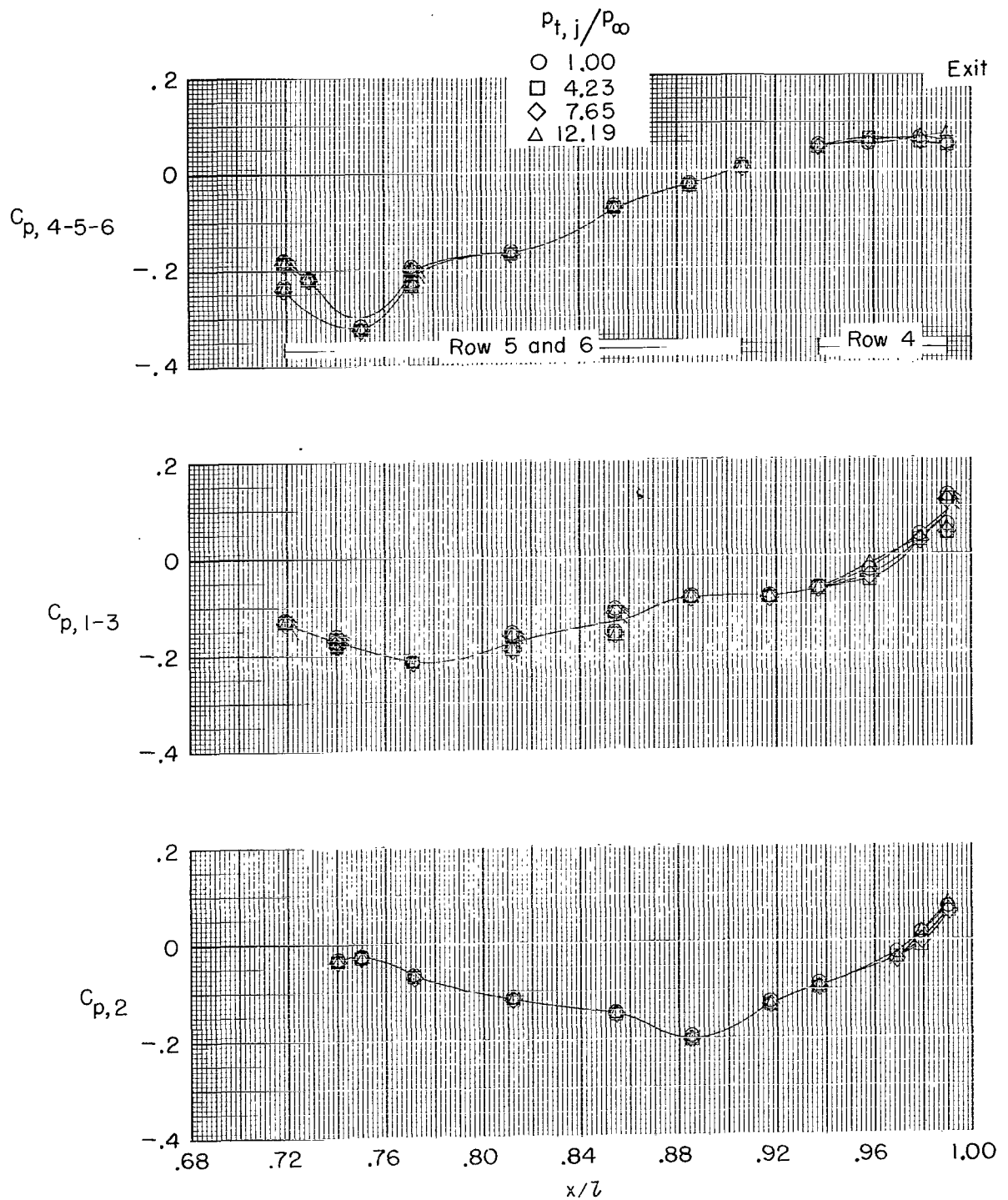
(b) $M = 0.80$.

Figure 12.- Continued.



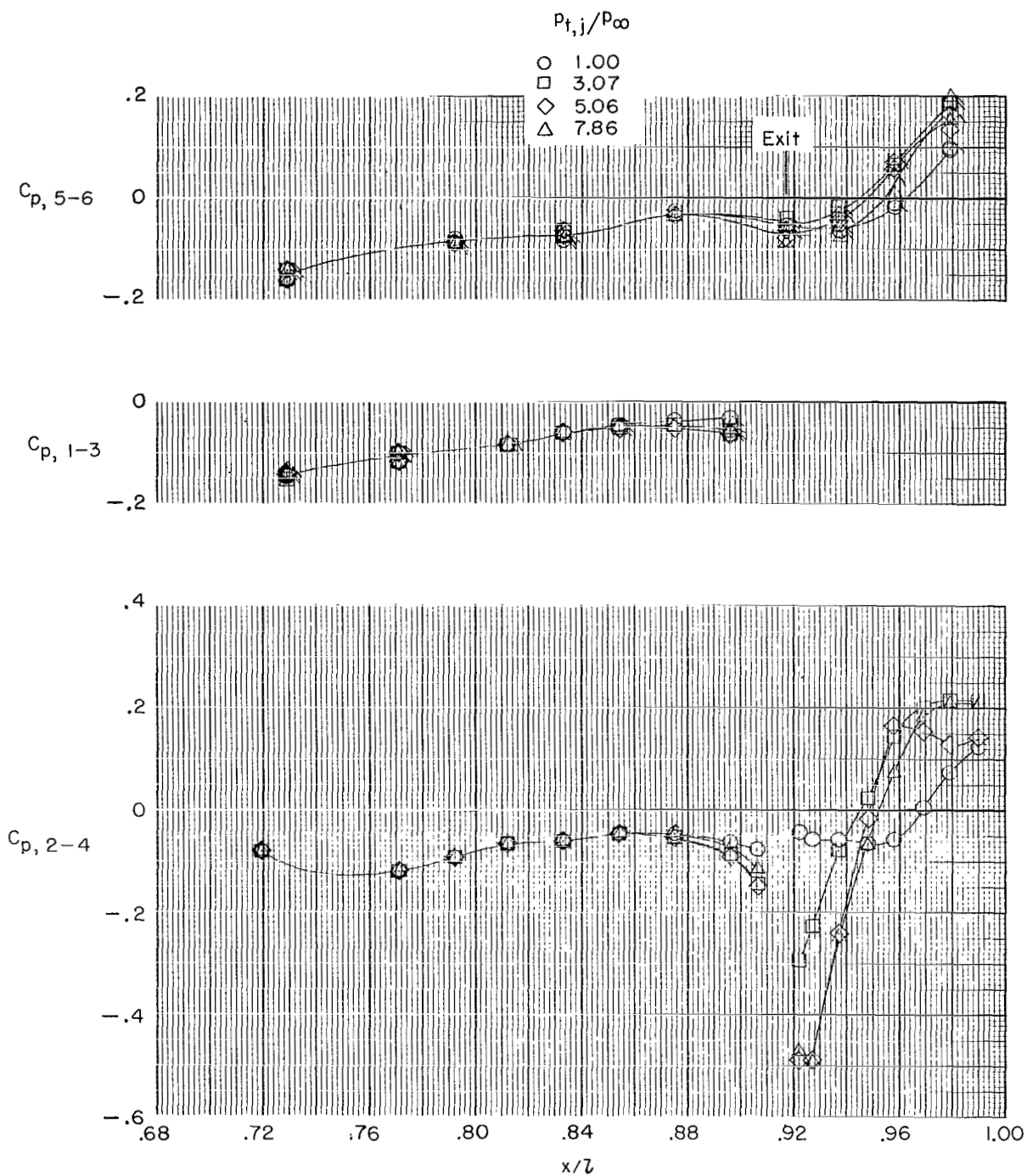
(c) $M = 0.95$.

Figure 12.- Continued.



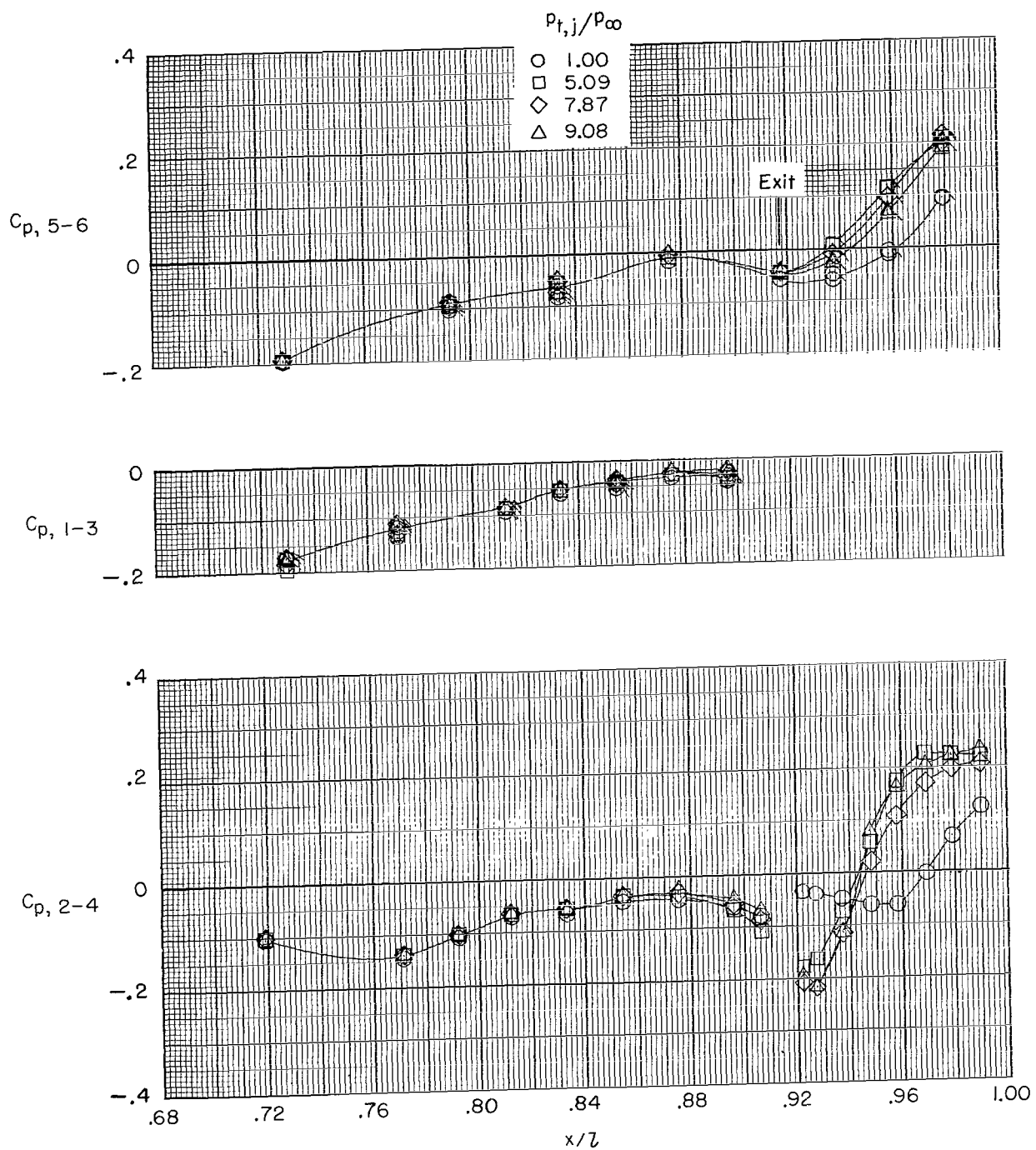
(d) $M = 1.30$.

Figure 12.- Concluded.



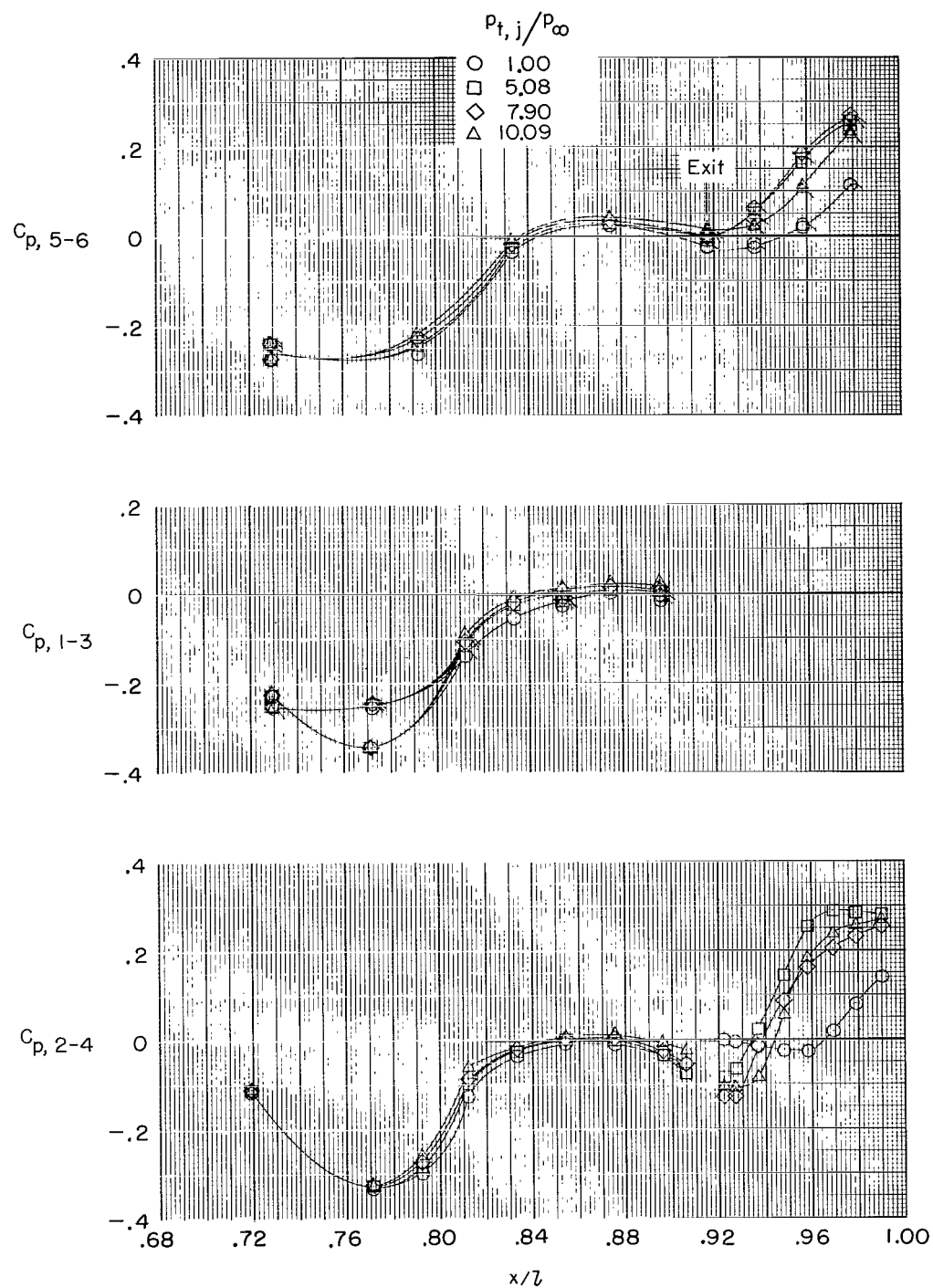
(a) $M = 0.50$.

Figure 13.- Afterbody pressure distributions for A-2 afterbody. Convergent-divergent nozzles.



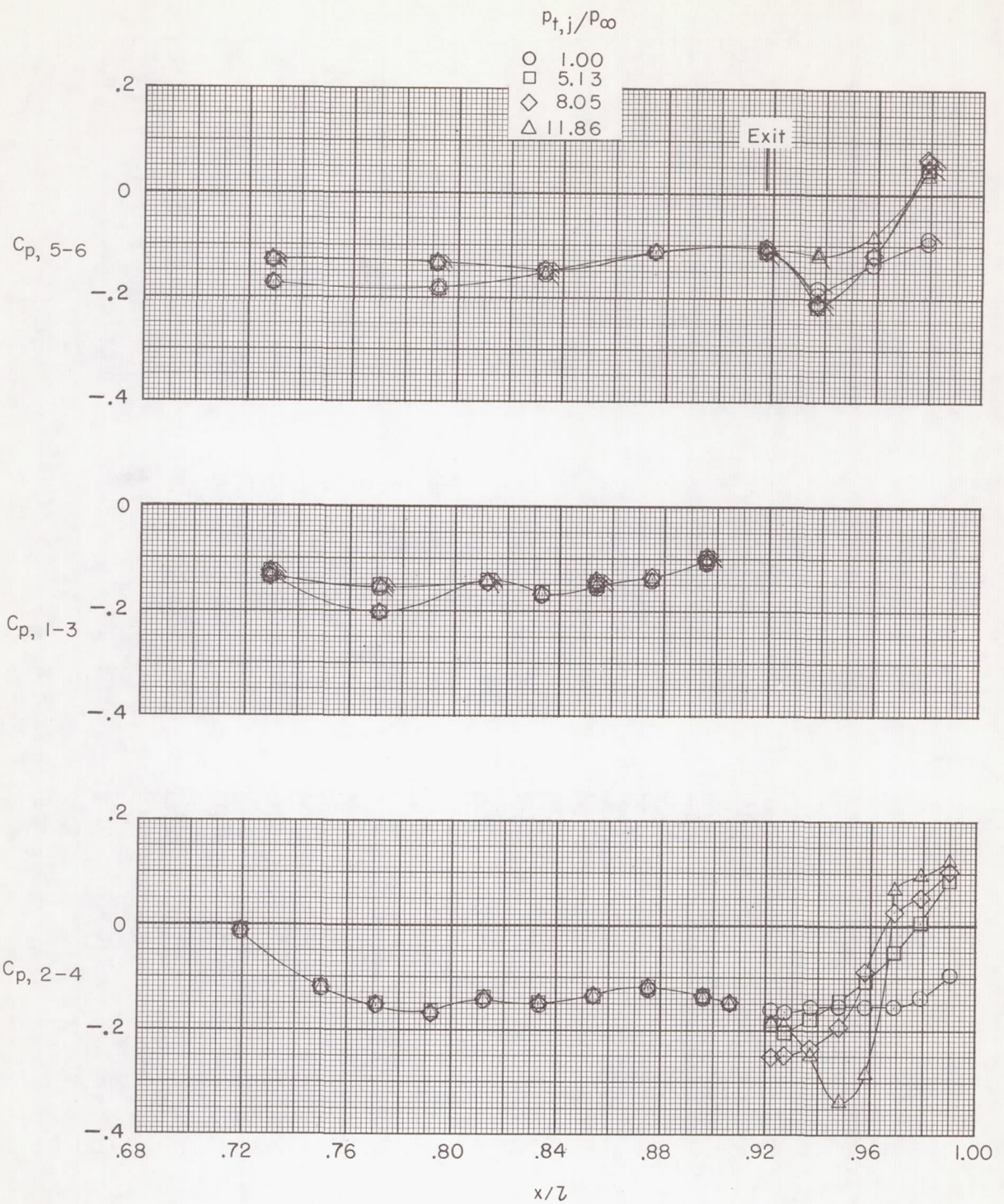
(b) $M = 0.80$.

Figure 13.- Continued.



(c) $M = 0.95$.

Figure 13.- Continued.



(d) $M = 1.30$.

Figure 13.- Concluded.

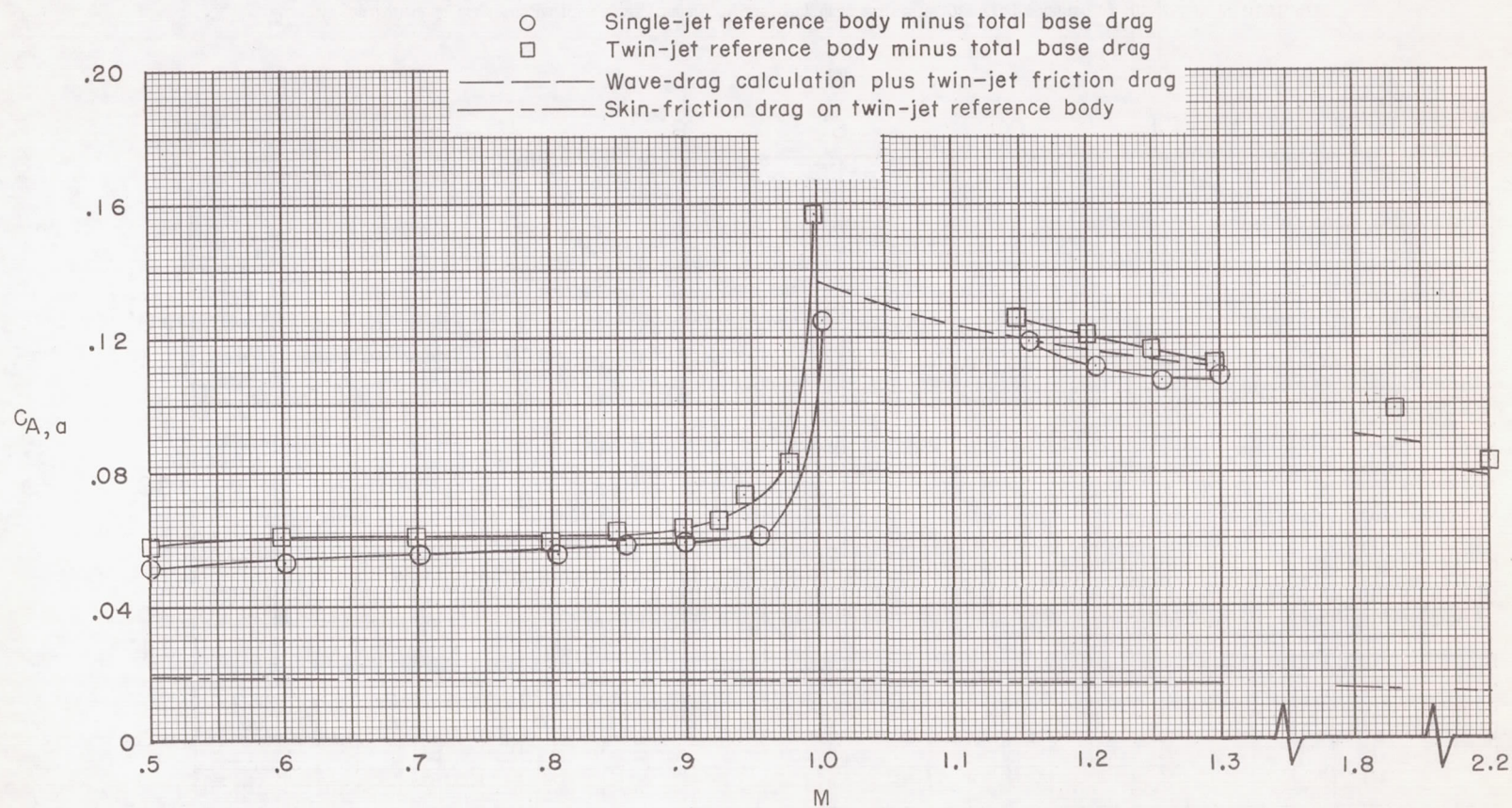


Figure 14.- Comparison of measured drag on the twin- and single-jet reference bodies with total base drag removed.

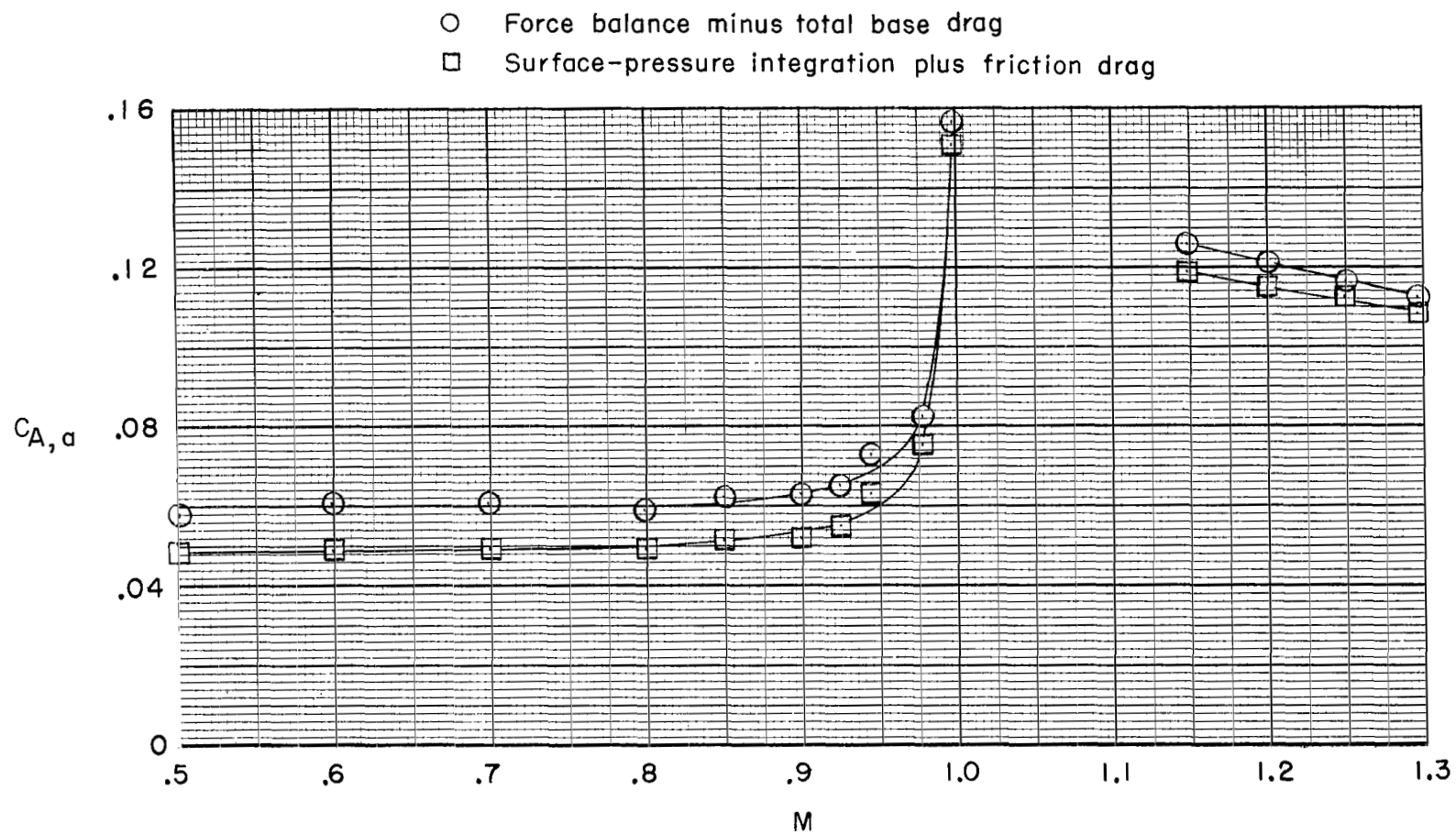


Figure 15.- Comparison of direct-force balance measurement of afterbody drag with afterbody drag obtained by integration of afterbody pressures for twin-jet reference body.

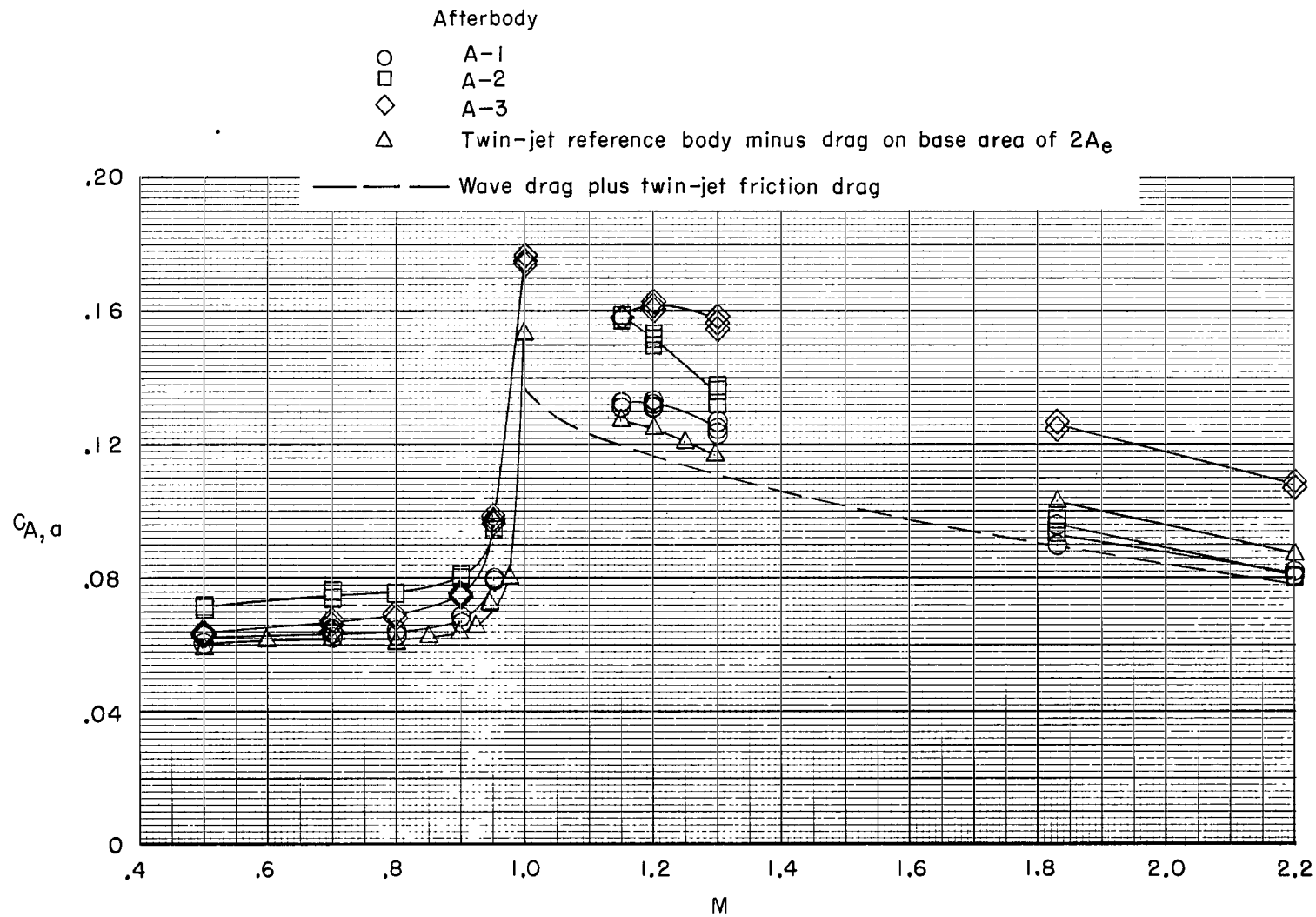
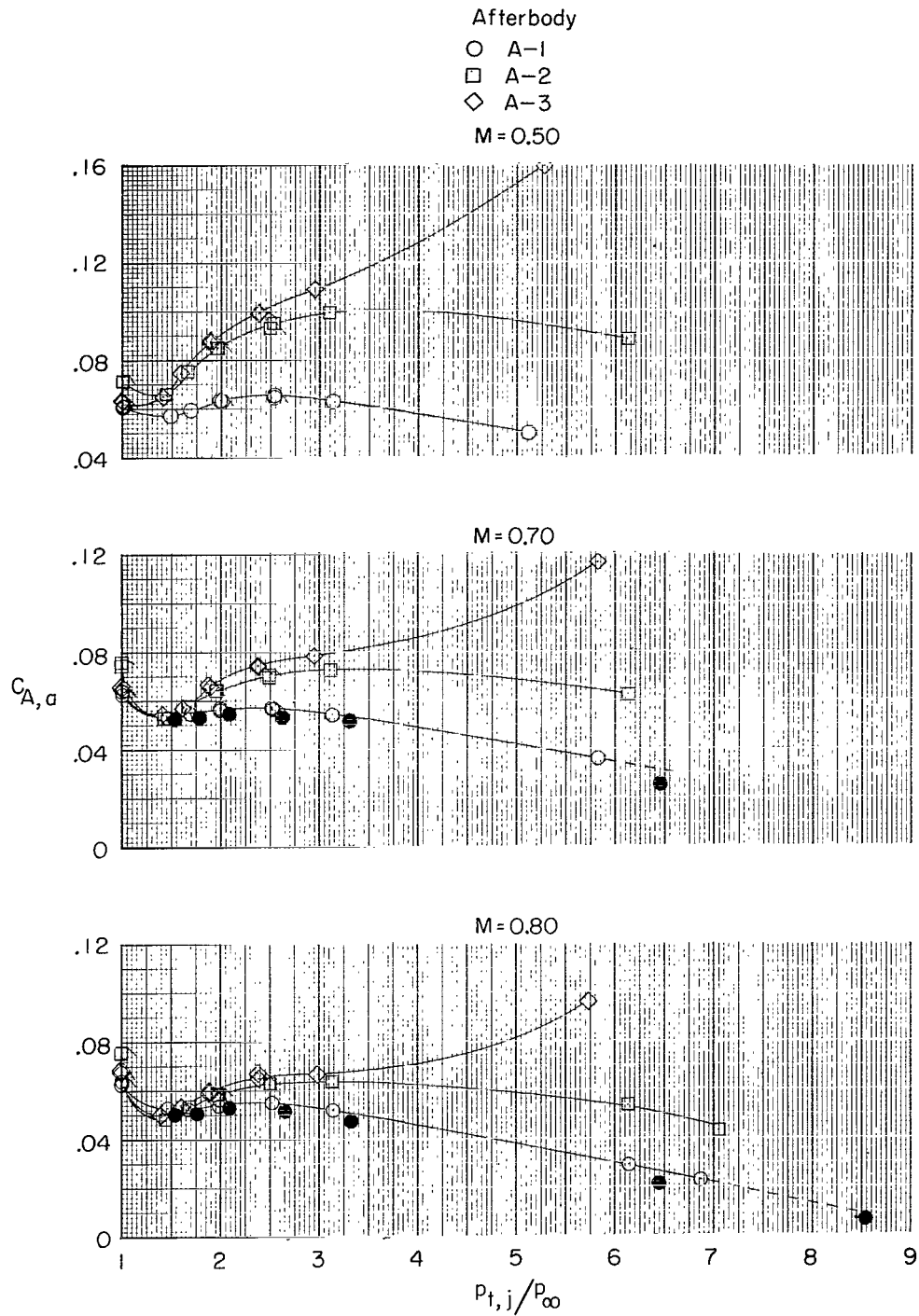
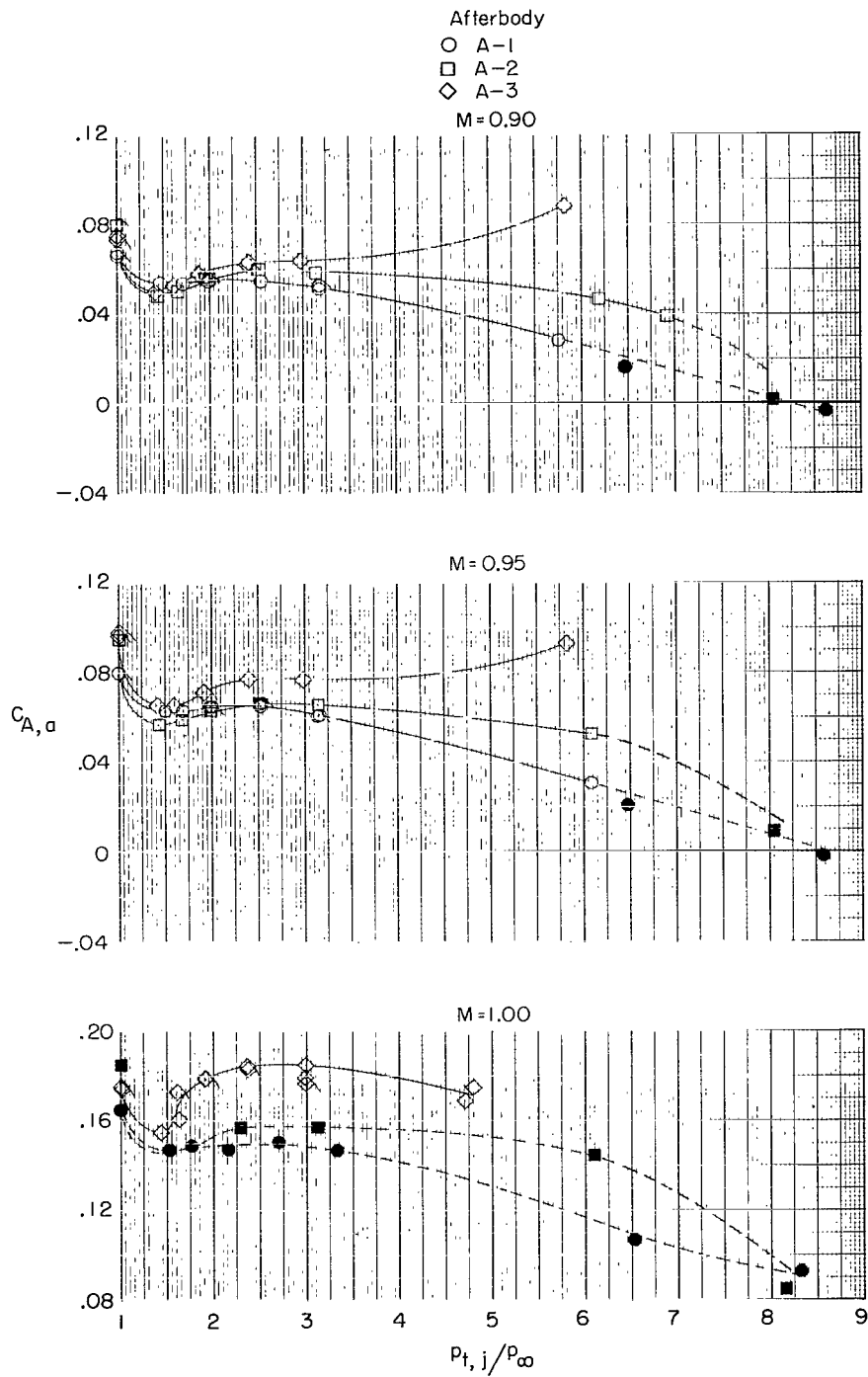


Figure 16.- Afterbody drag coefficient variation with Mach number. Jet off.



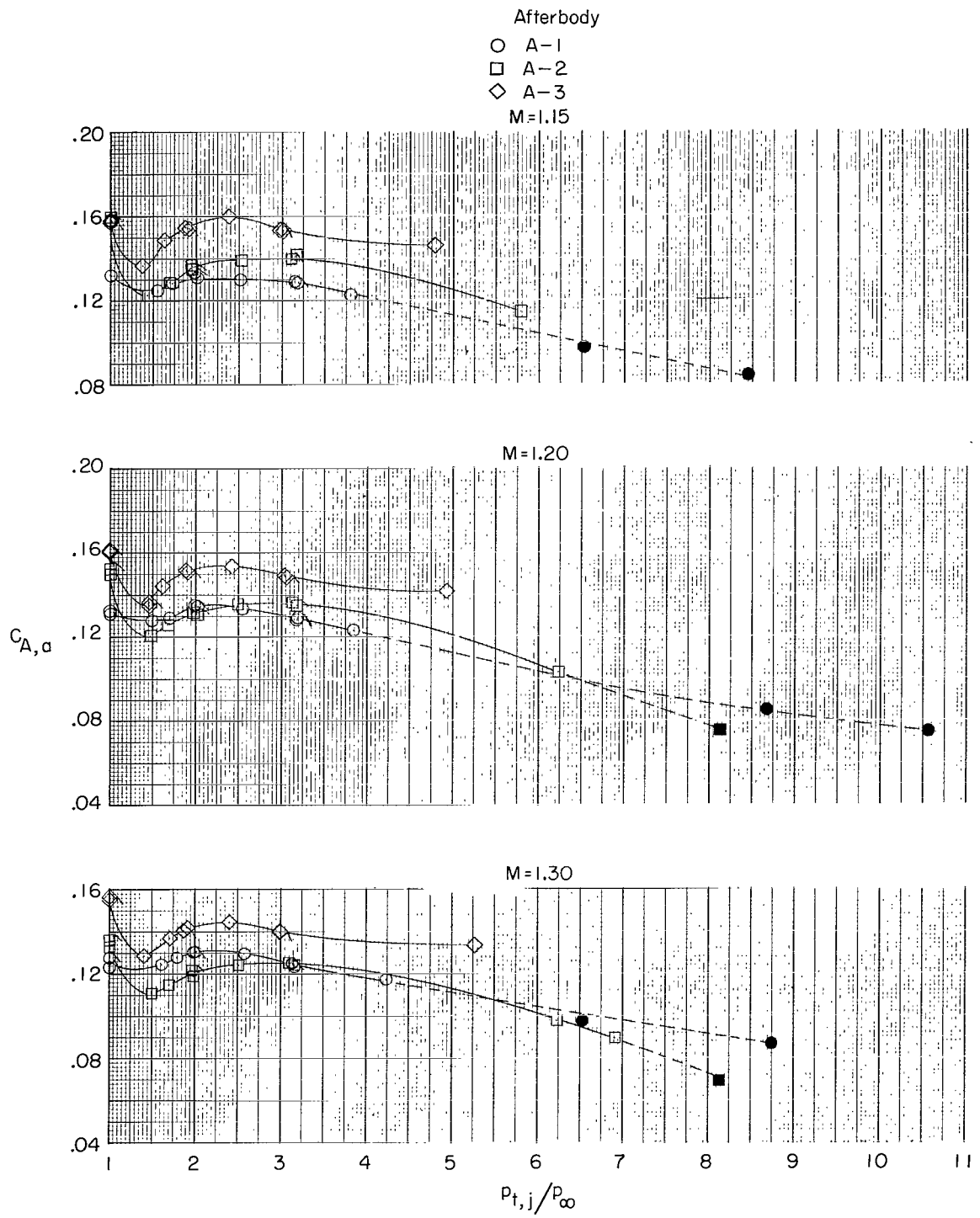
(a) $M = 0.50$ to 0.80 .

Figure 17.- Afterbody drag coefficient variation with jet total-pressure ratio at several Mach numbers. Convergent nozzles. Solid symbols indicate pressure integration plus skin friction. Flags denote decreasing pressure ratio.



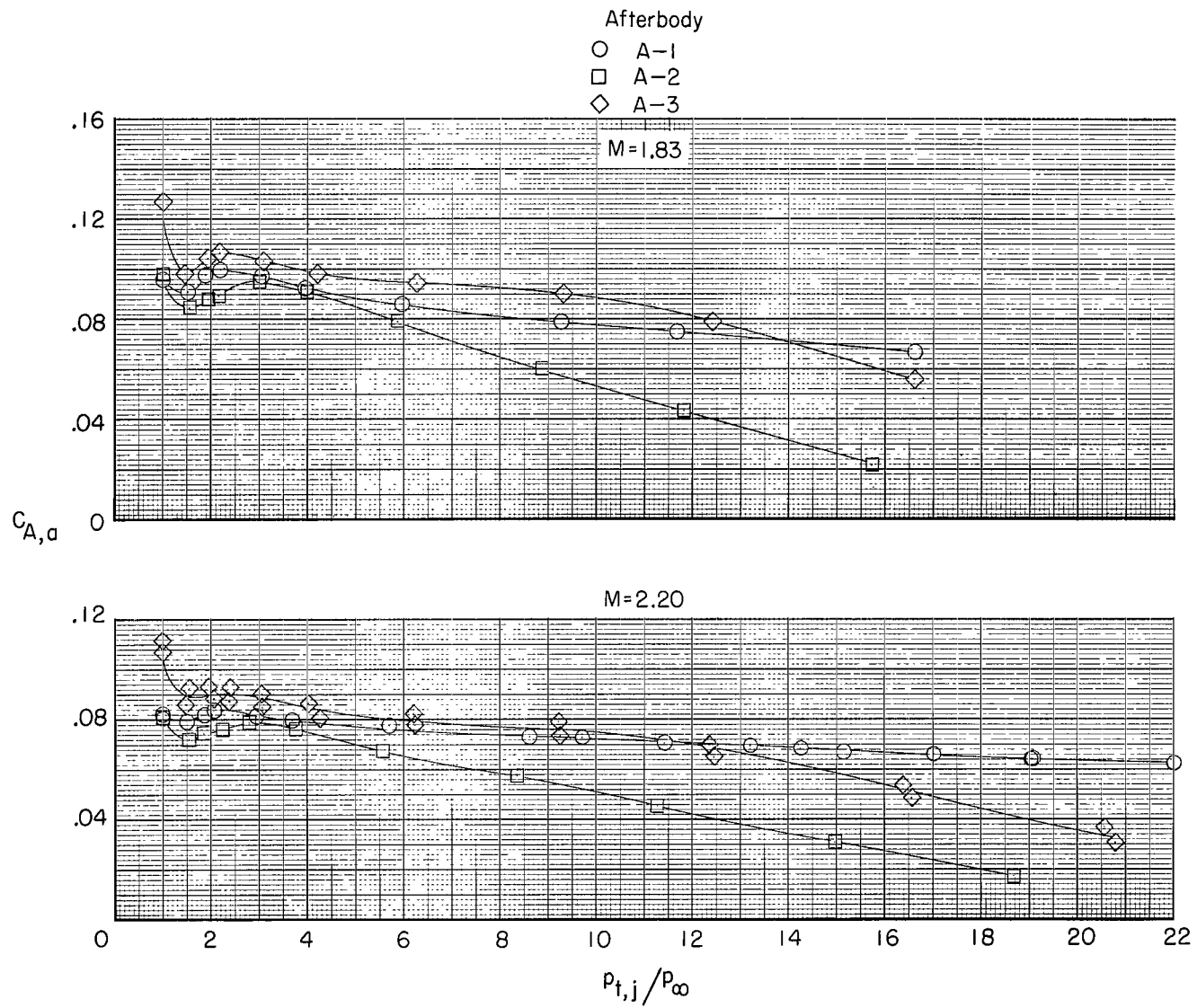
(b) $M = 0.90$ to 1.00 .

Figure 17.- Continued.



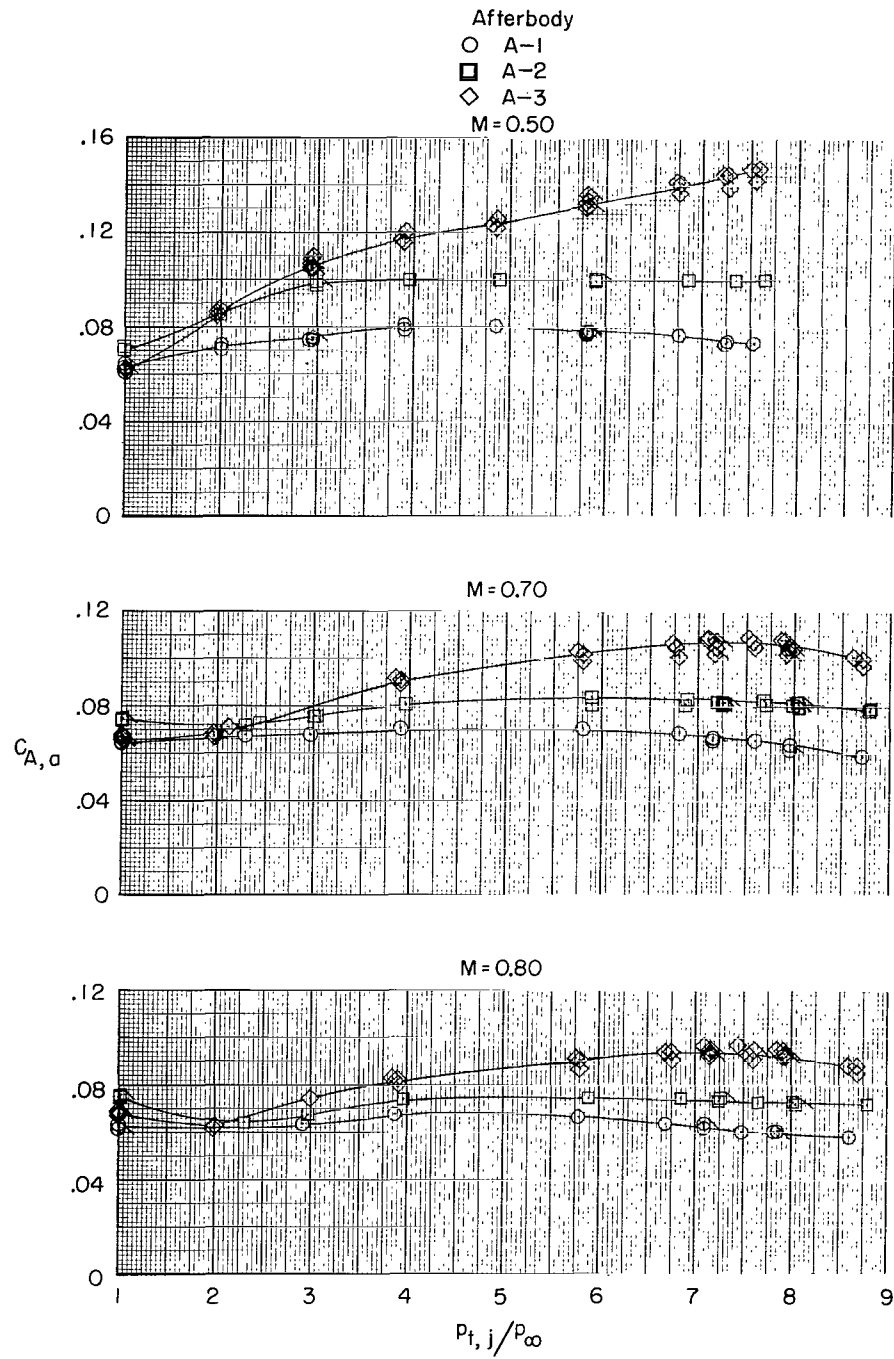
(c) $M = 1.15$ to 1.30 .

Figure 17.- Continued.



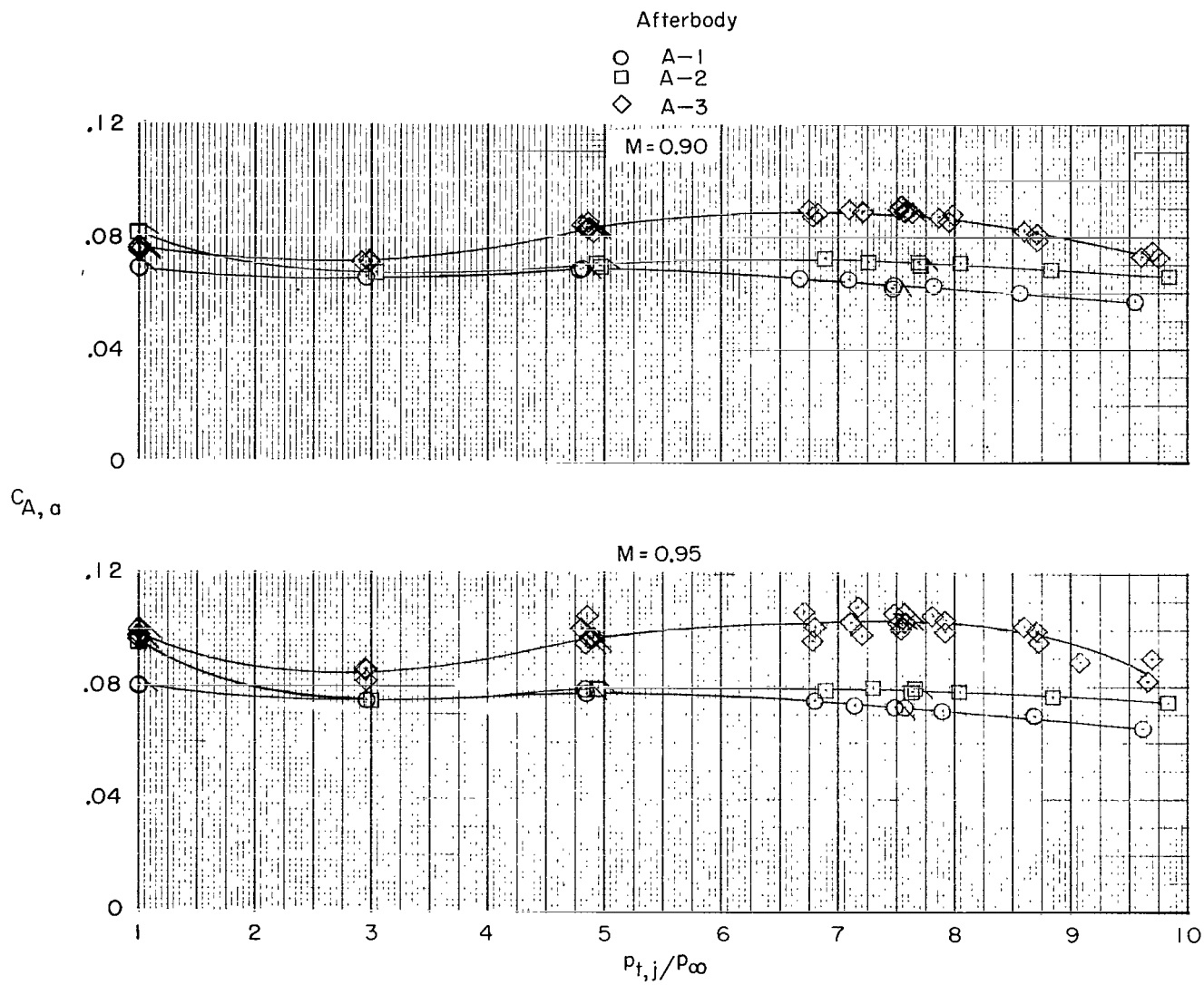
(d) $M = 1.83$ and 2.20 .

Figure 17.- Concluded.



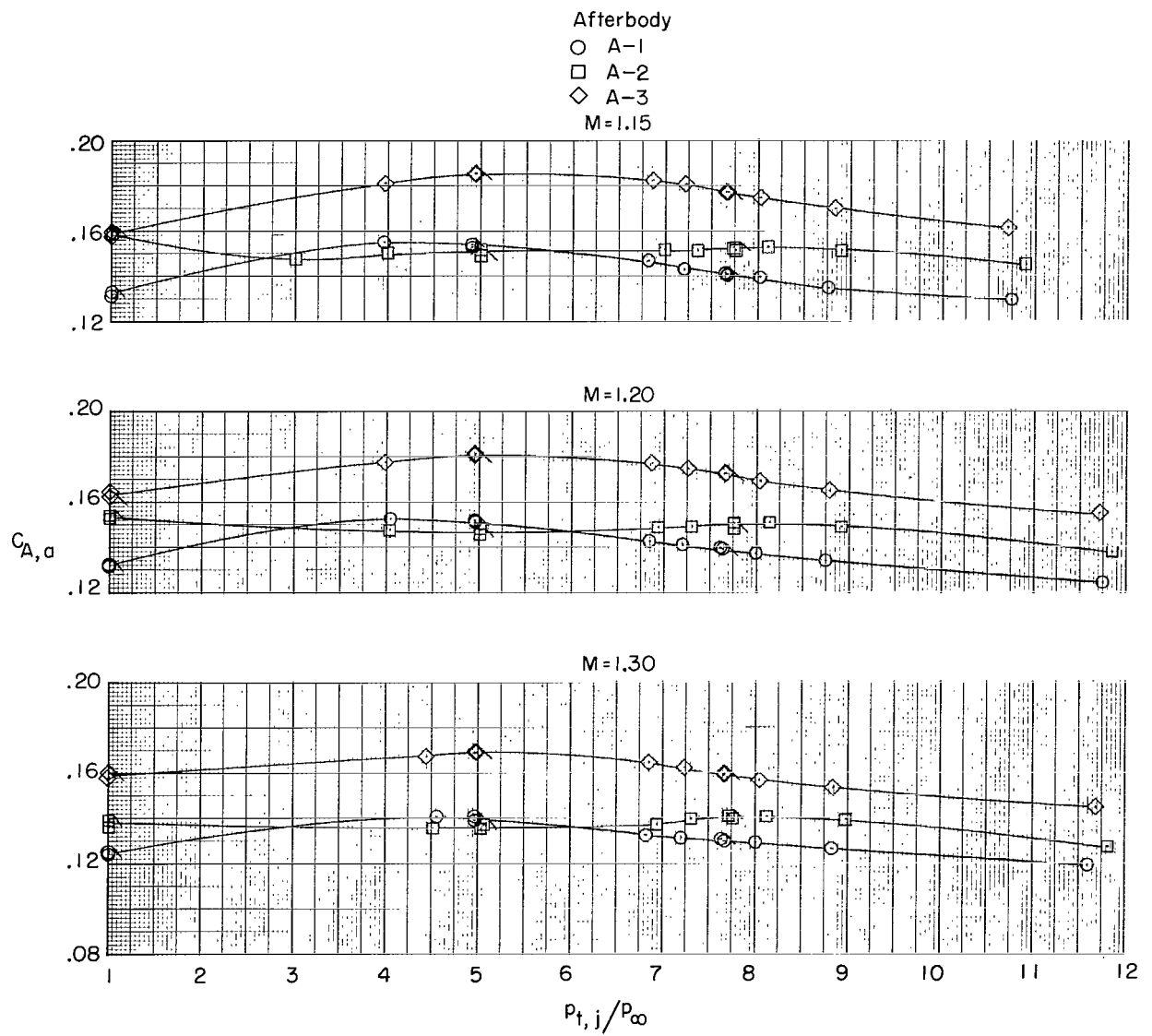
(a) $M = 0.50$ to 0.80 .

Figure 18.- Afterbody drag coefficient variation with jet total-pressure ratio at several Mach numbers. Convergent-divergent nozzles. Flags denote decreasing pressure ratio.



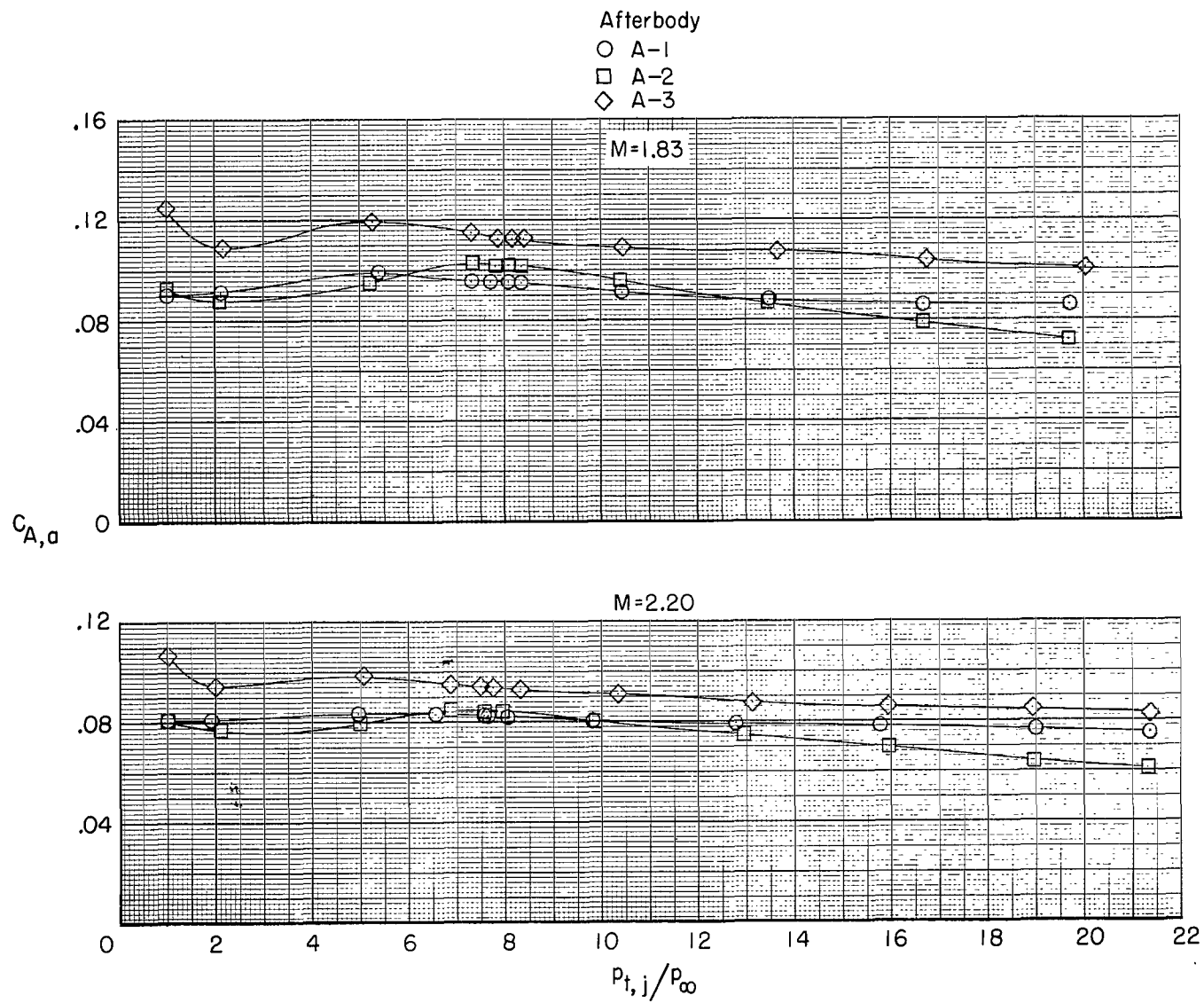
(b) $M = 0.90$ and 0.95 .

Figure 18.- Continued.



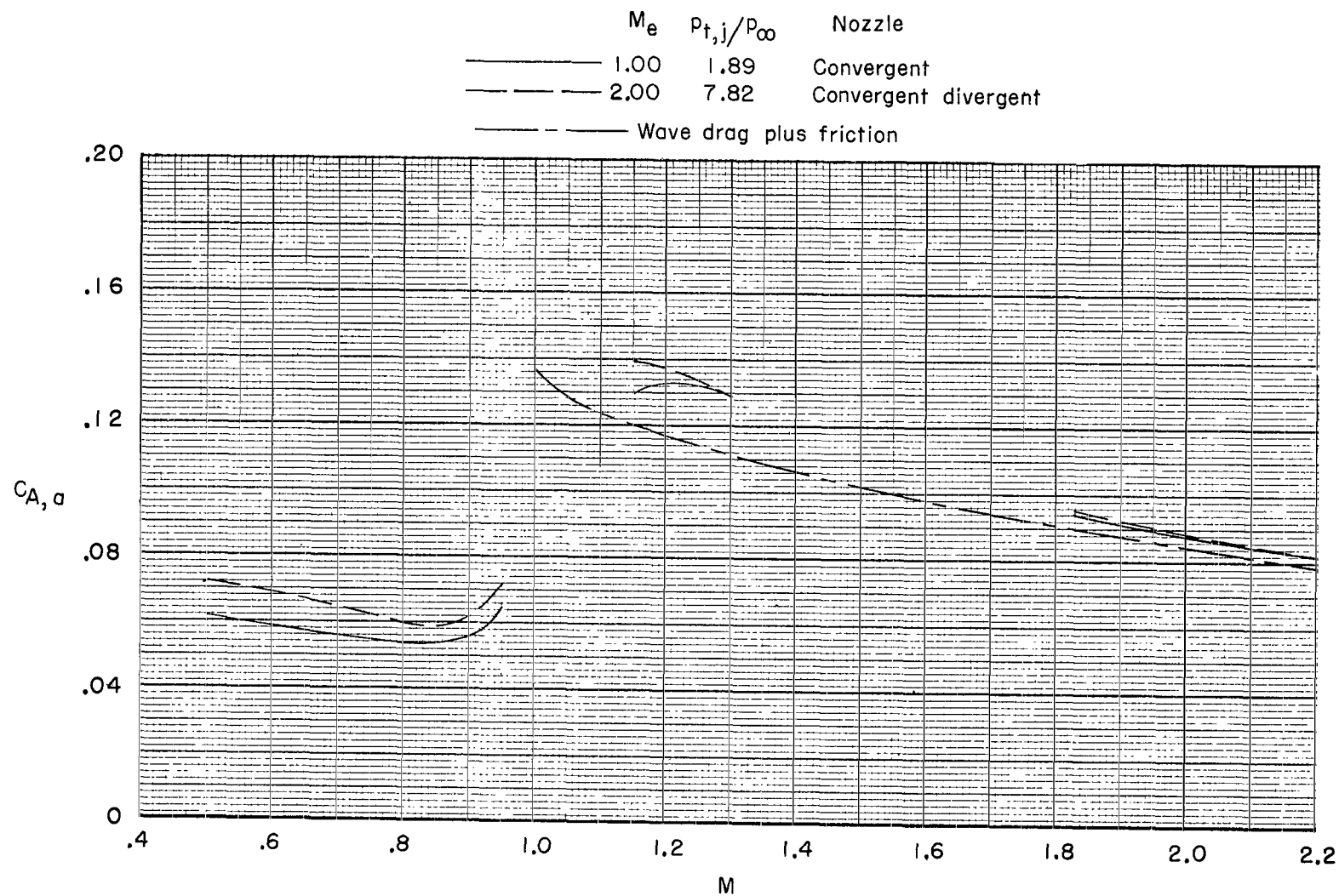
(c) $M = 1.15$ to 1.30 .

Figure 18.- Continued.



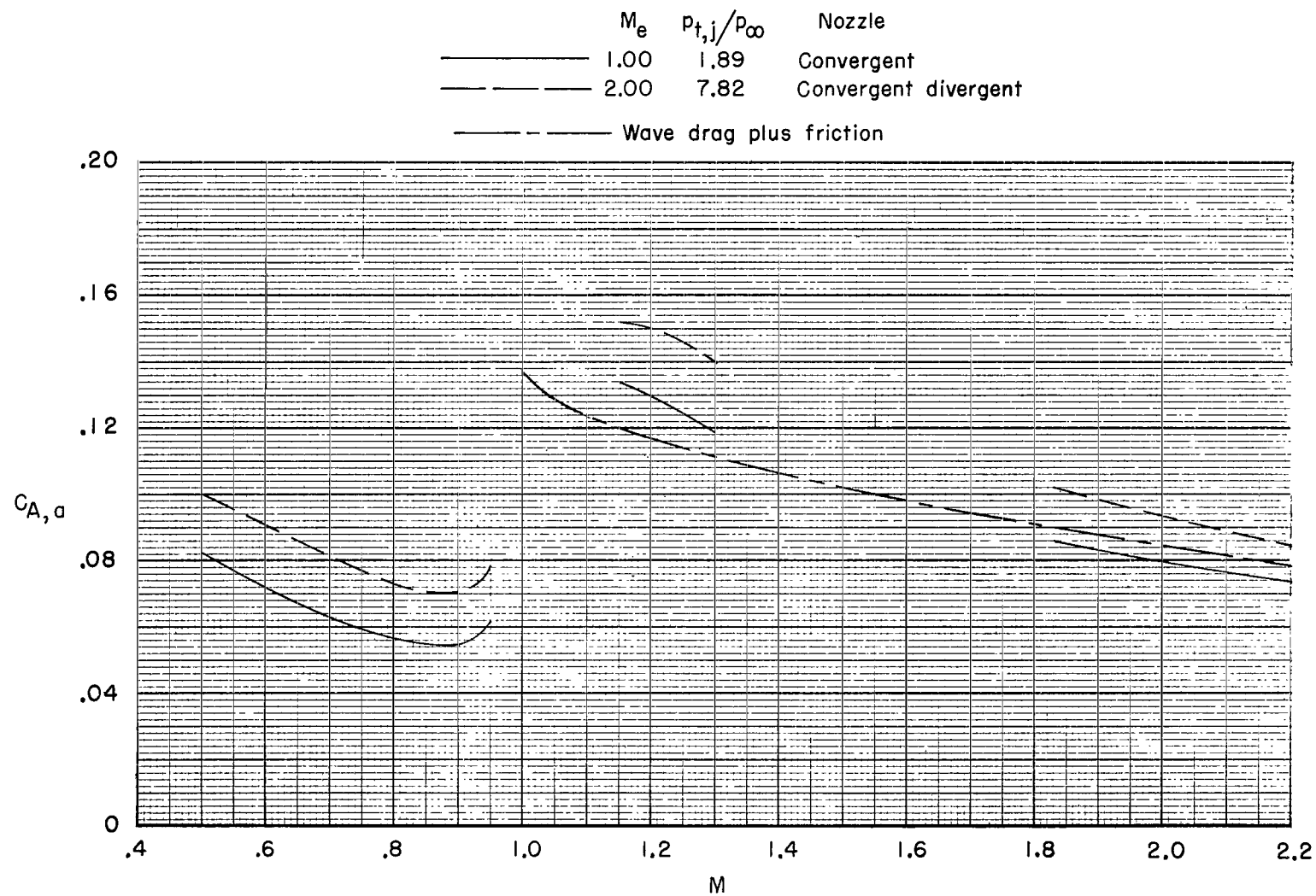
(d) $M = 1.83$ and 2.20 .

Figure 18.- Concluded.



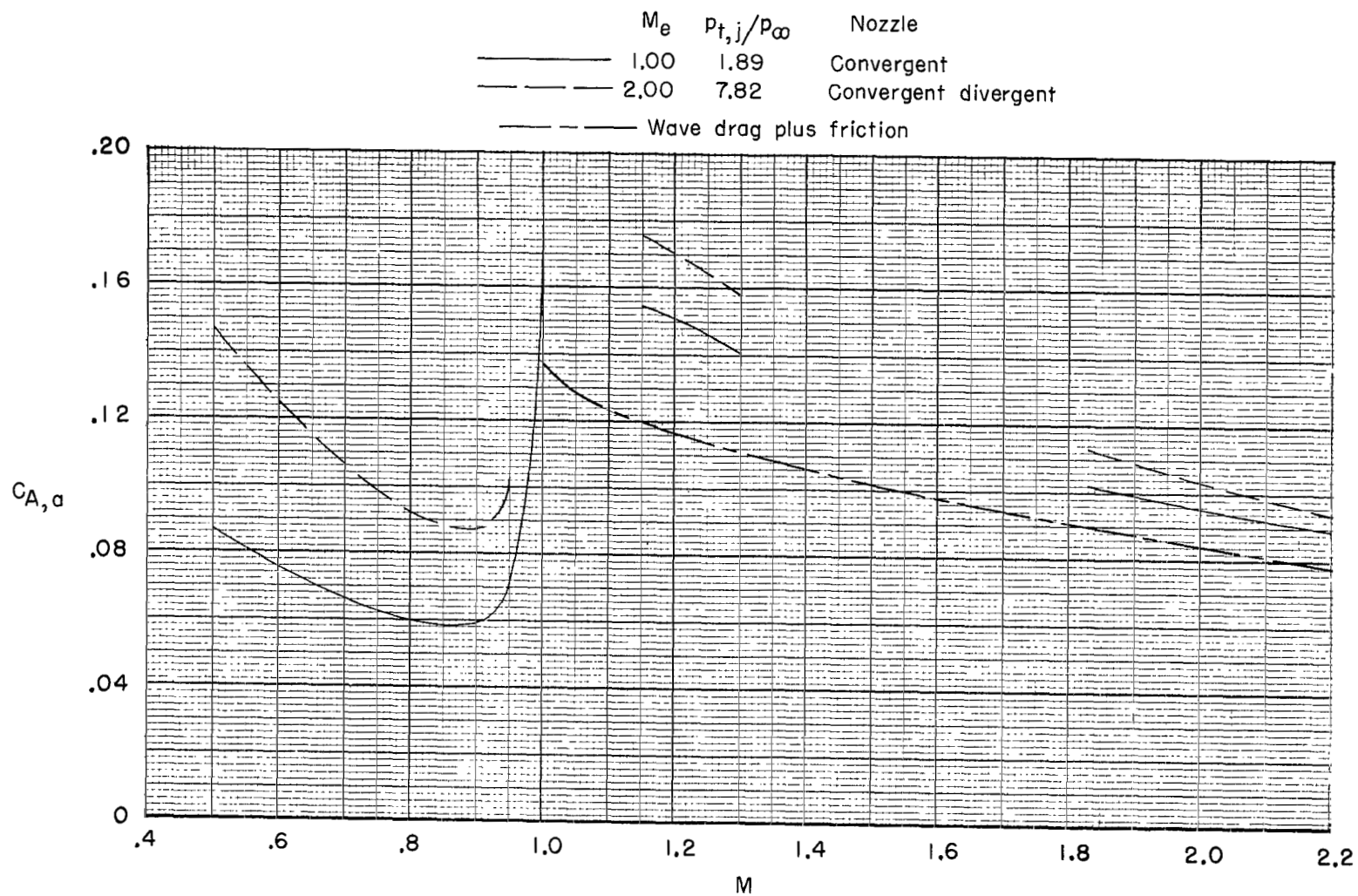
(a) Afterbody A-1.

Figure 19.- Variation of afterbody drag coefficient with Mach number with both nozzles at design total-pressure ratio (cylindrical jets).



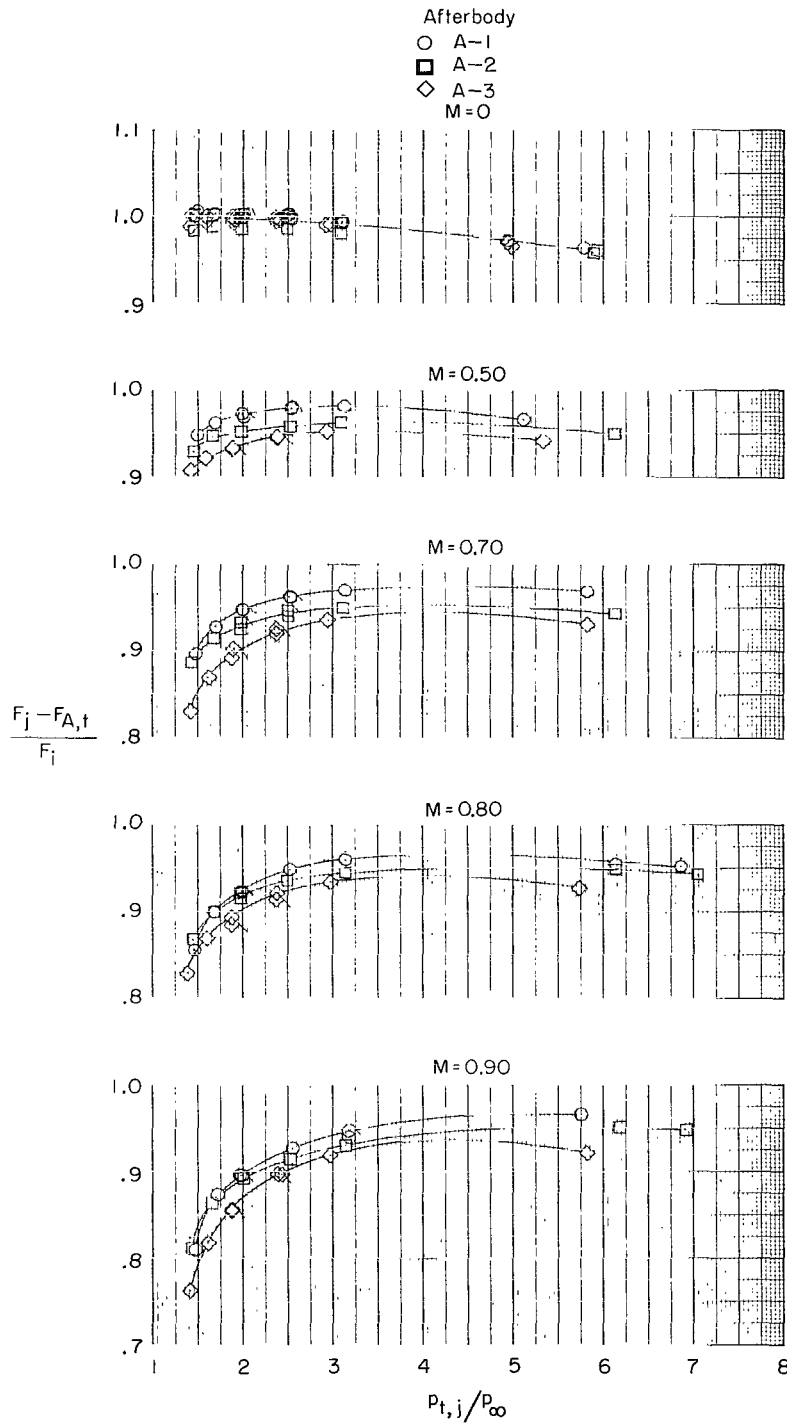
(b) Afterbody A-2.

Figure 19.- Continued.



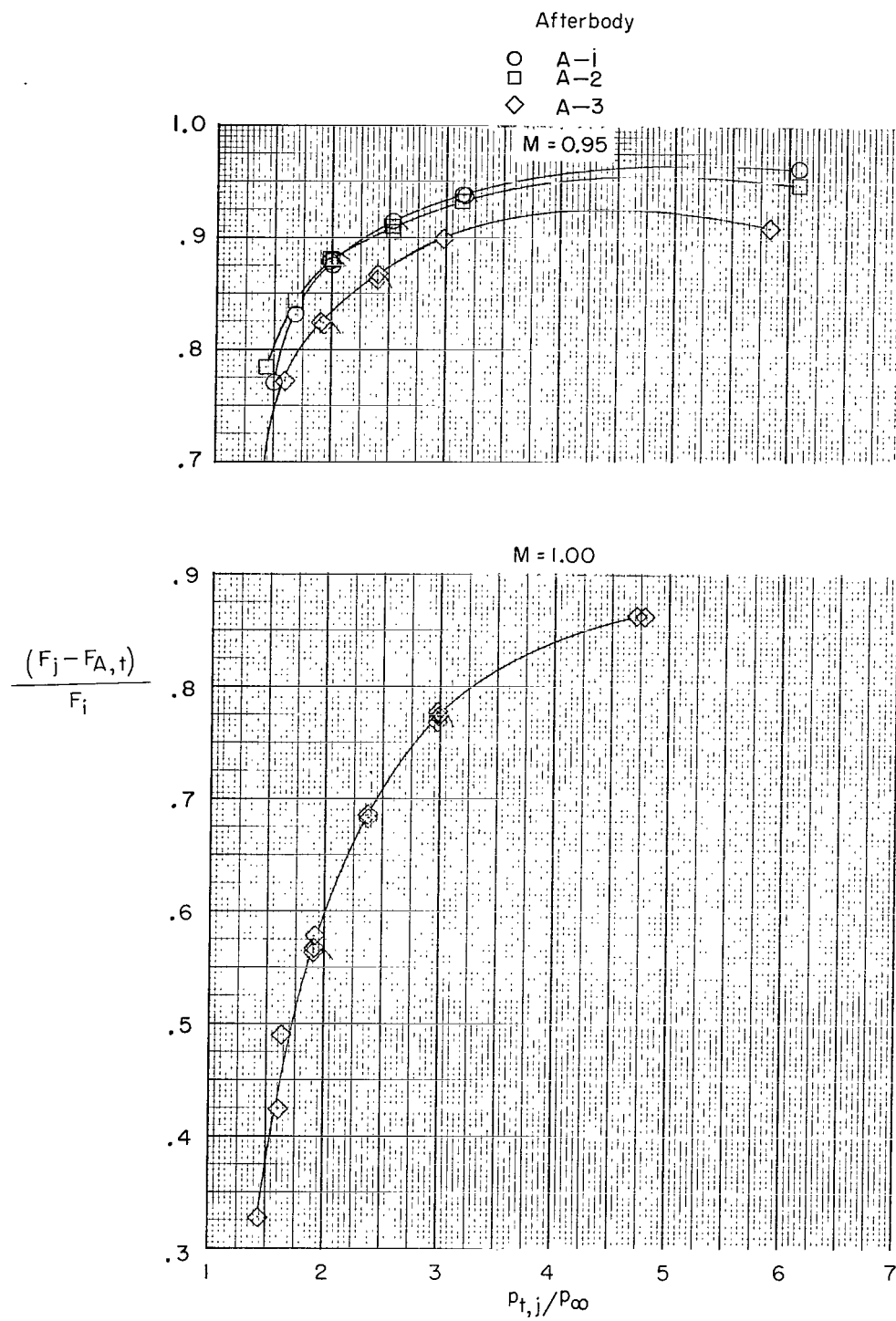
(c) Afterbody A-3.

Figure 19.- Concluded.



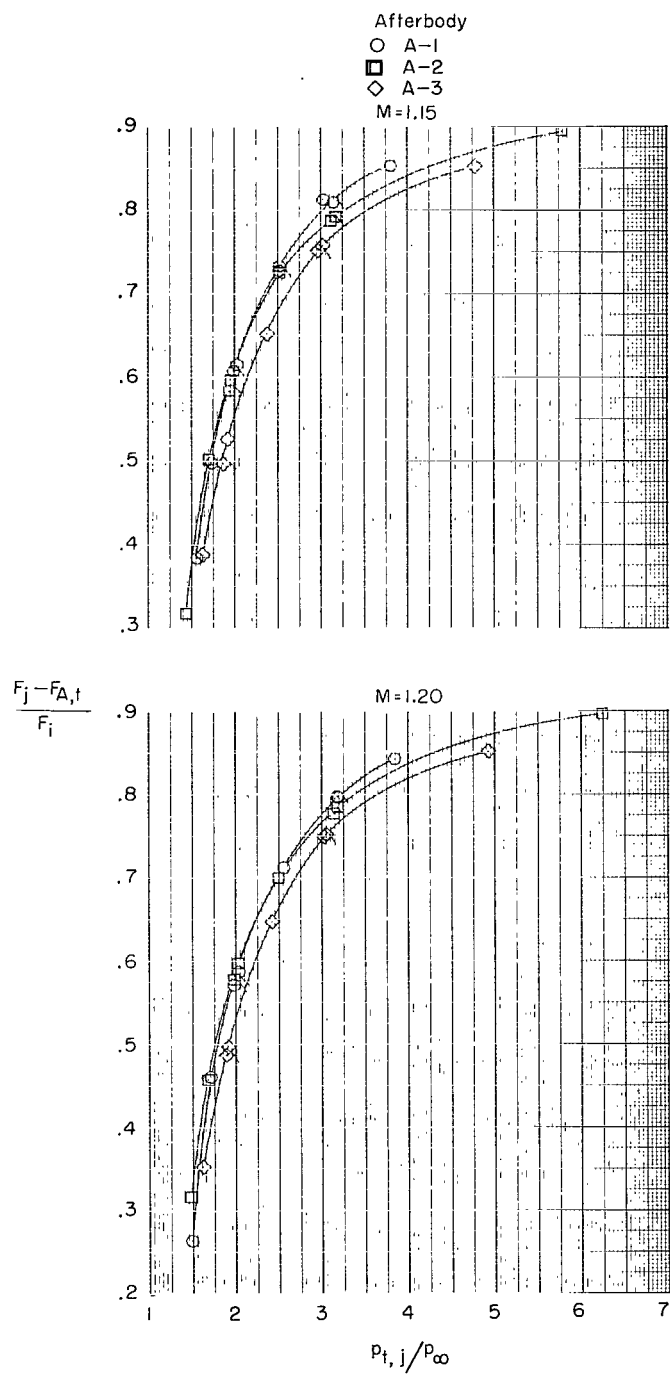
(a) M = 0 to 0.90.

Figure 20.- Thrust minus afterbody drag performance at various Mach numbers. Convergent nozzles. Tails indicate decreasing pressure ratio.



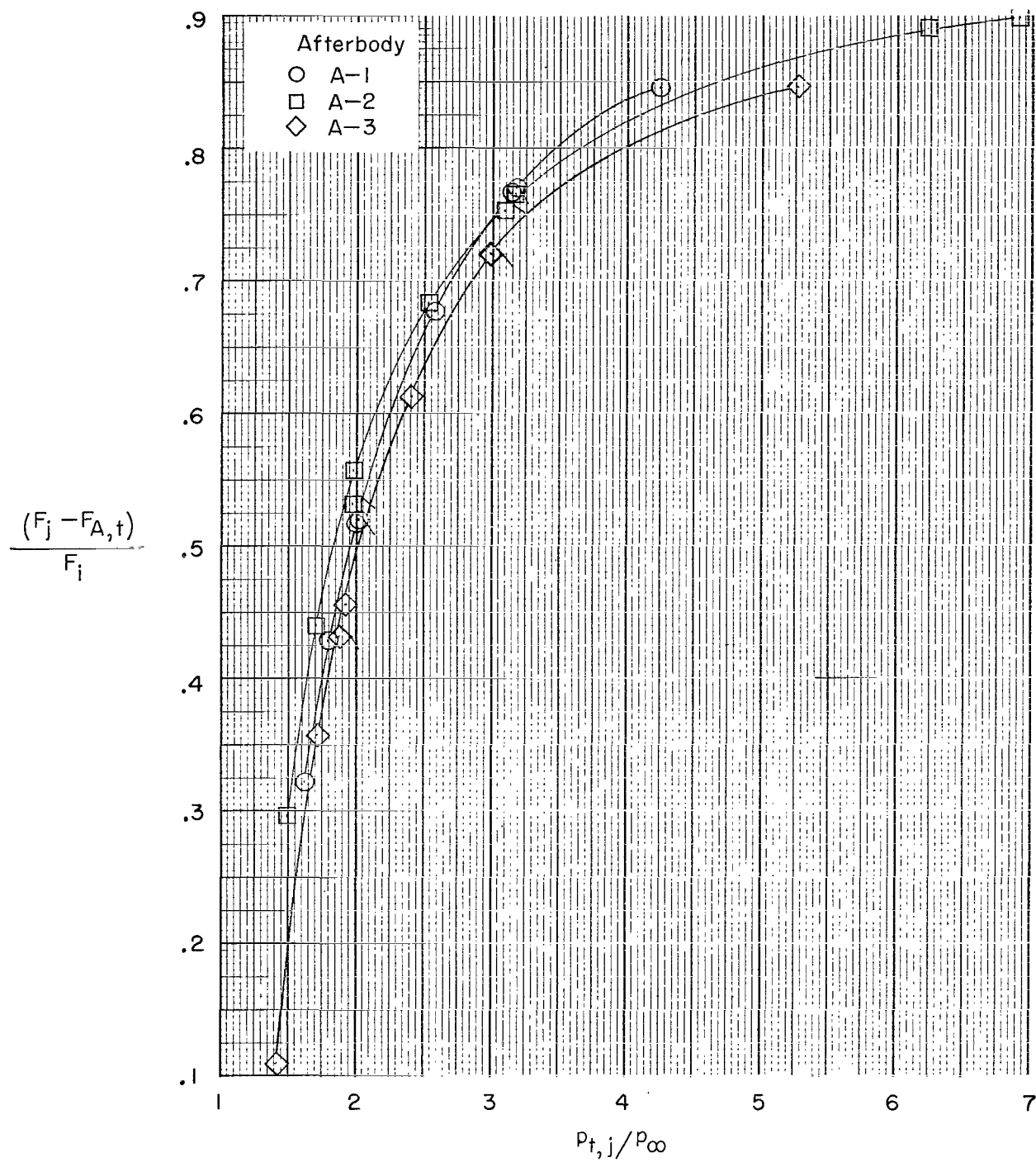
(b) $M = 0.95$ and 1.00 .

Figure 20.- Continued.



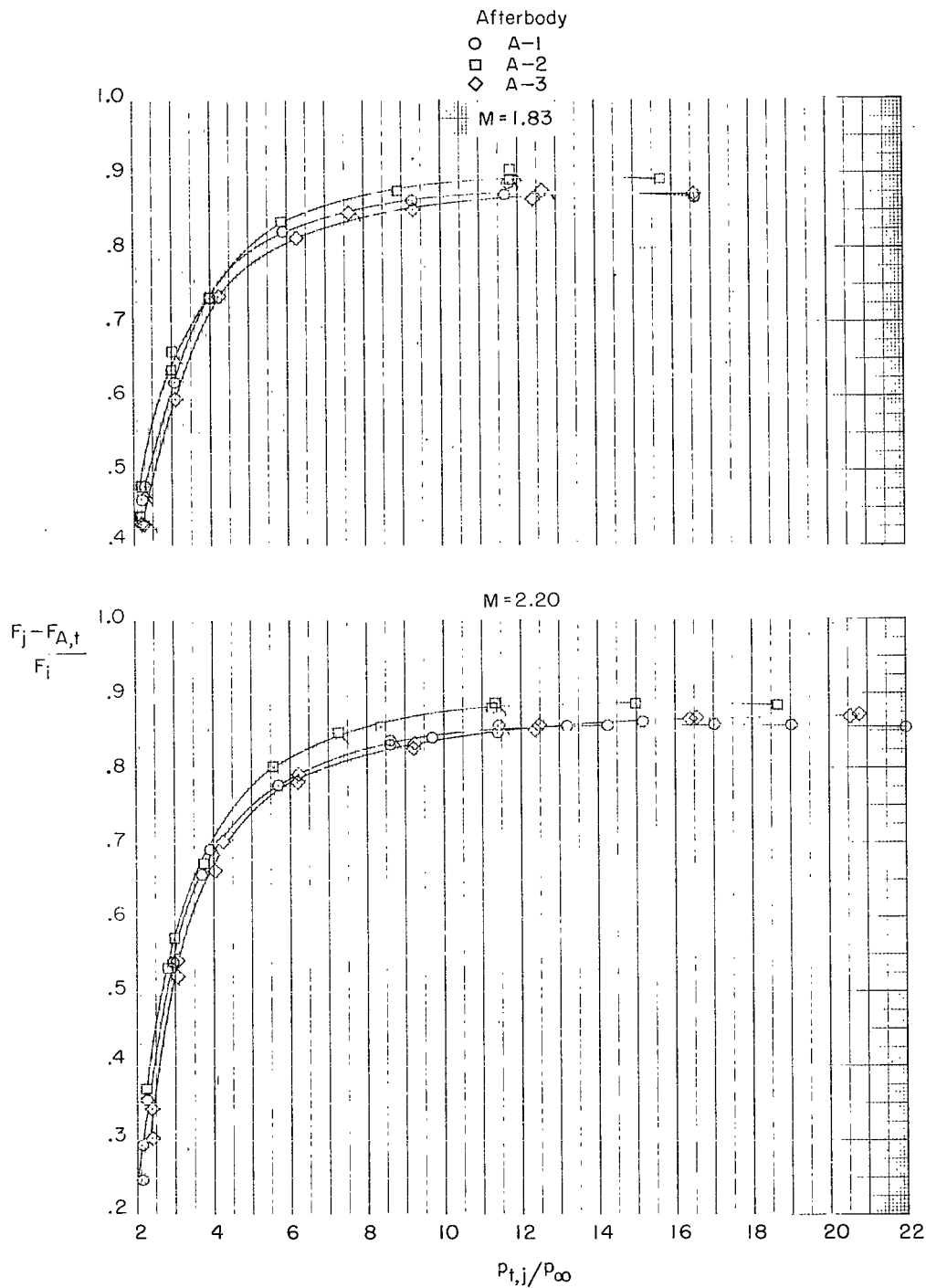
(c) $M = 1.15$ and 1.20 .

Figure 20.- Continued.



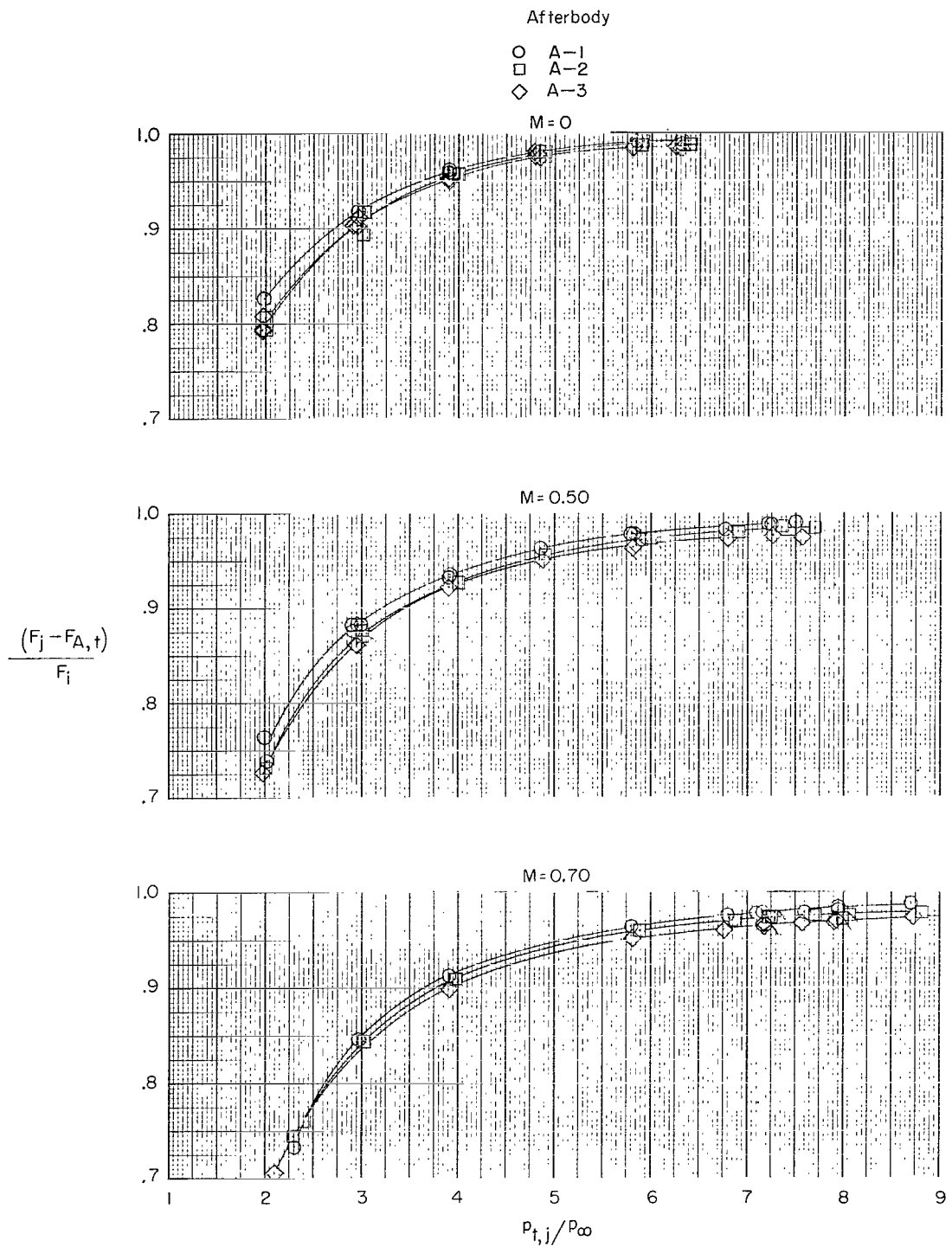
(d) $M = 1.30$.

Figure 20.- Continued.



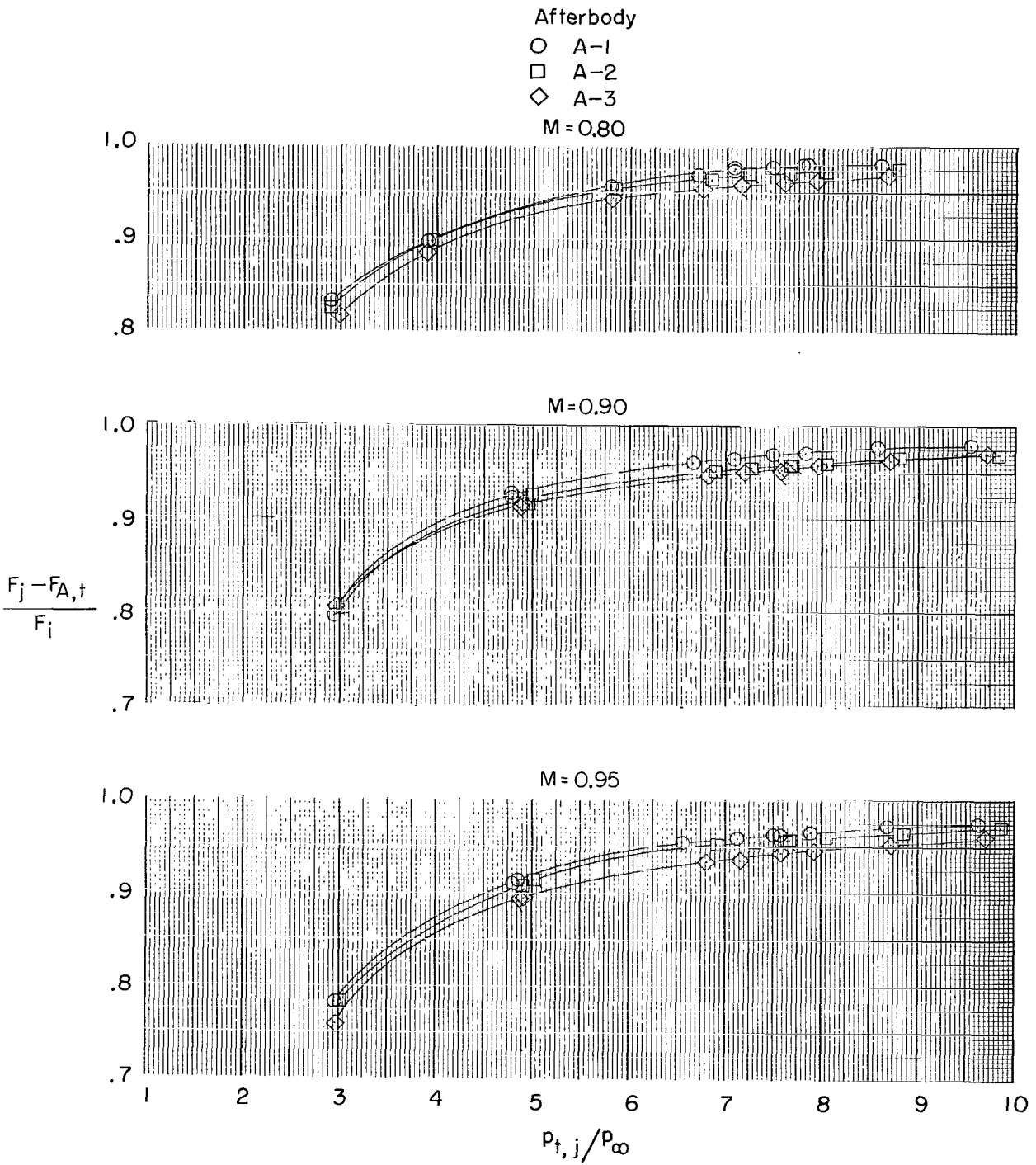
(e) $M = 1.83$ and 2.20 .

Figure 20.- Concluded.



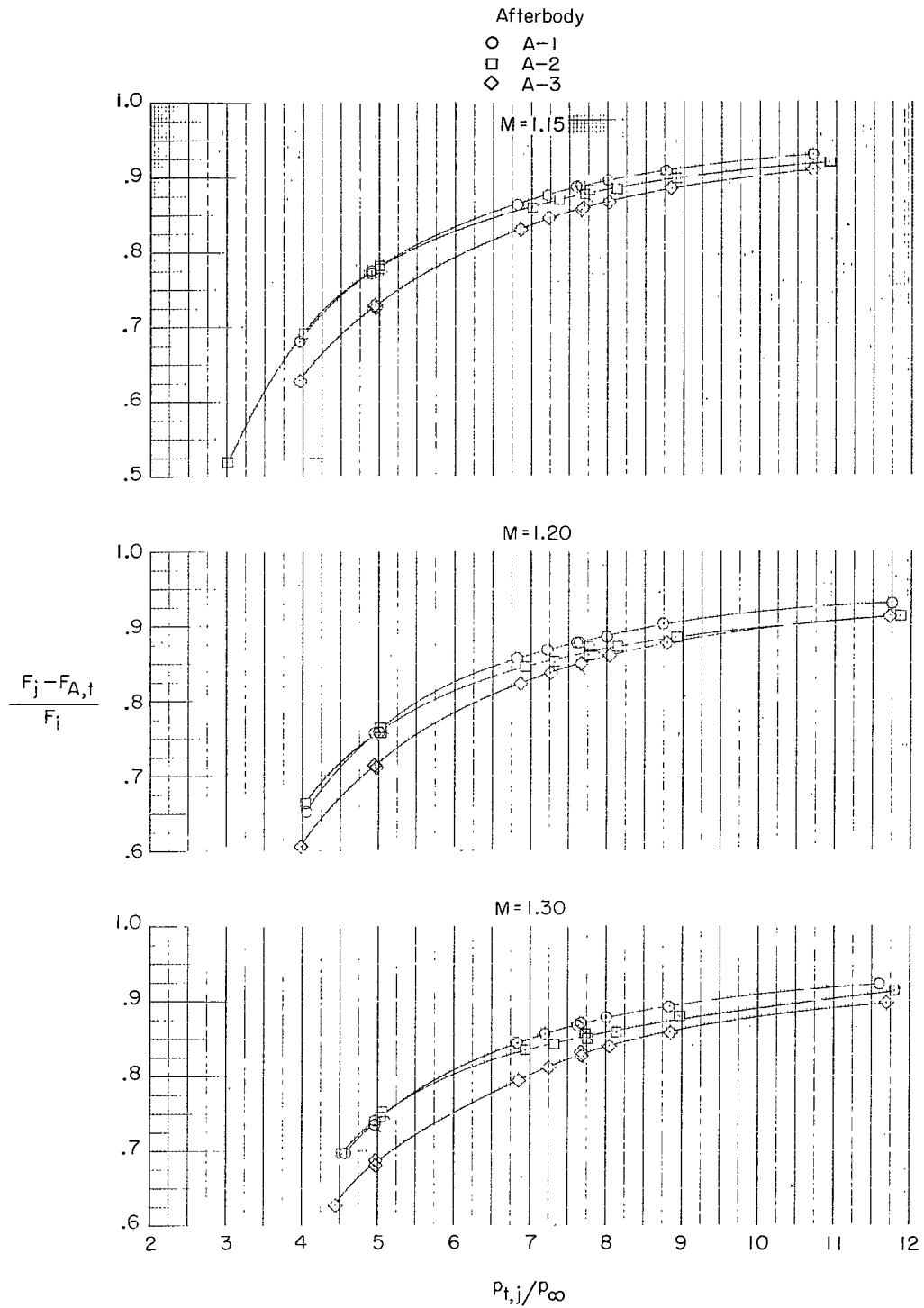
(a) M = 0 to 0.70.

Figure 21.- Thrust minus afterbody drag performance at various Mach numbers. Convergent-divergent nozzles. Flags denote decreasing pressure ratio.



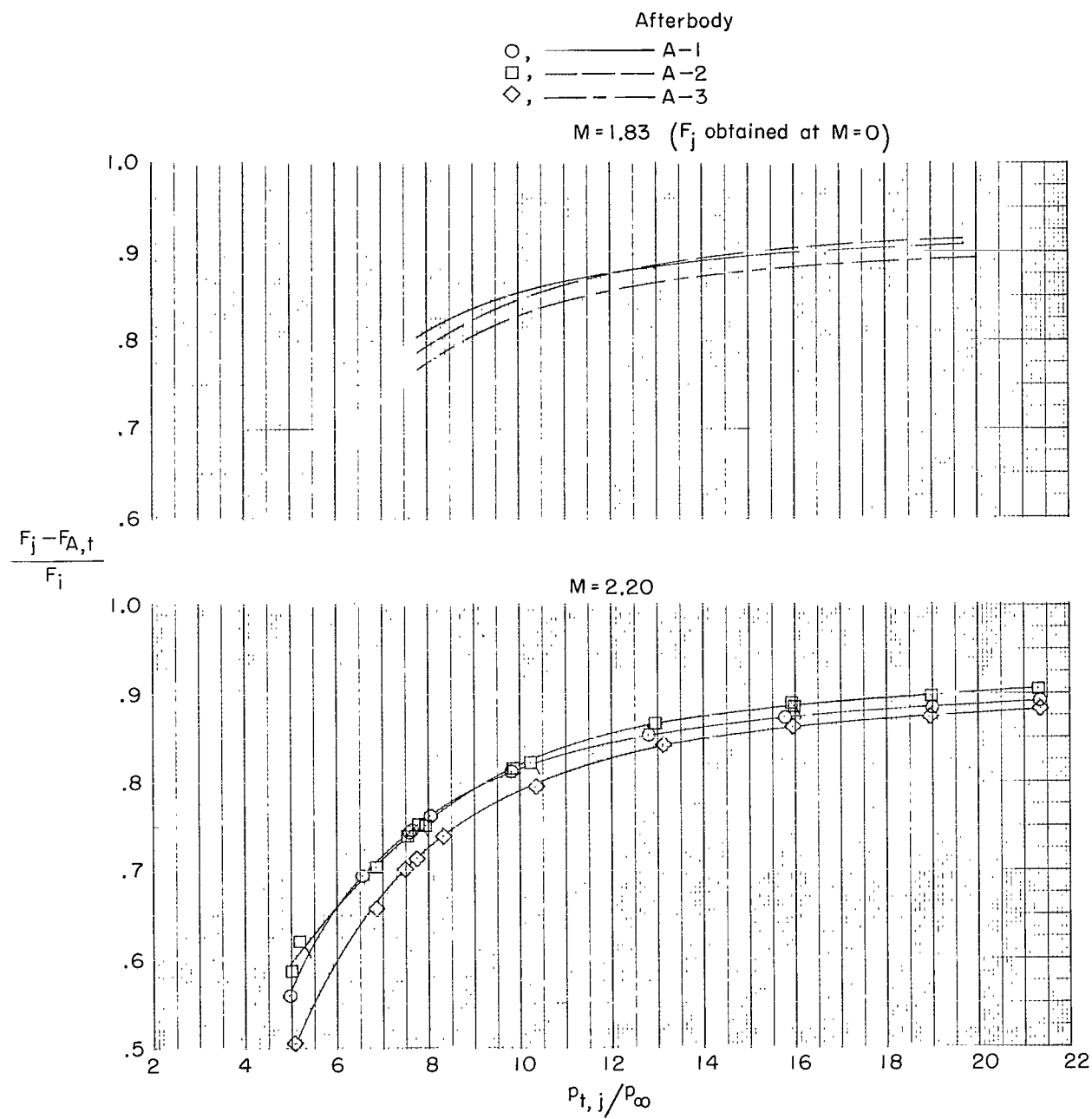
(b) $M = 0.80$ to 0.95 .

Figure 21.- Continued.



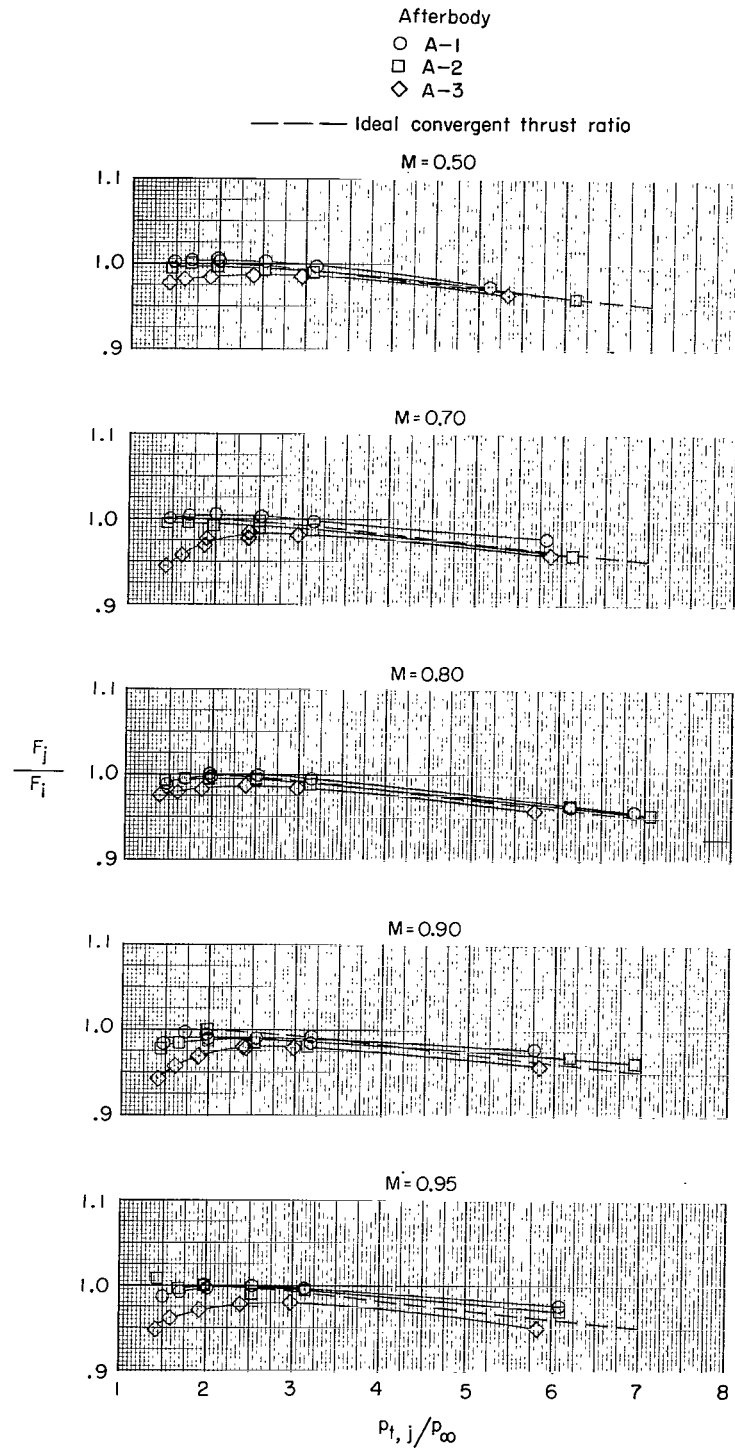
(c) $M = 1.15$ to 1.30 .

Figure 21.- Continued.



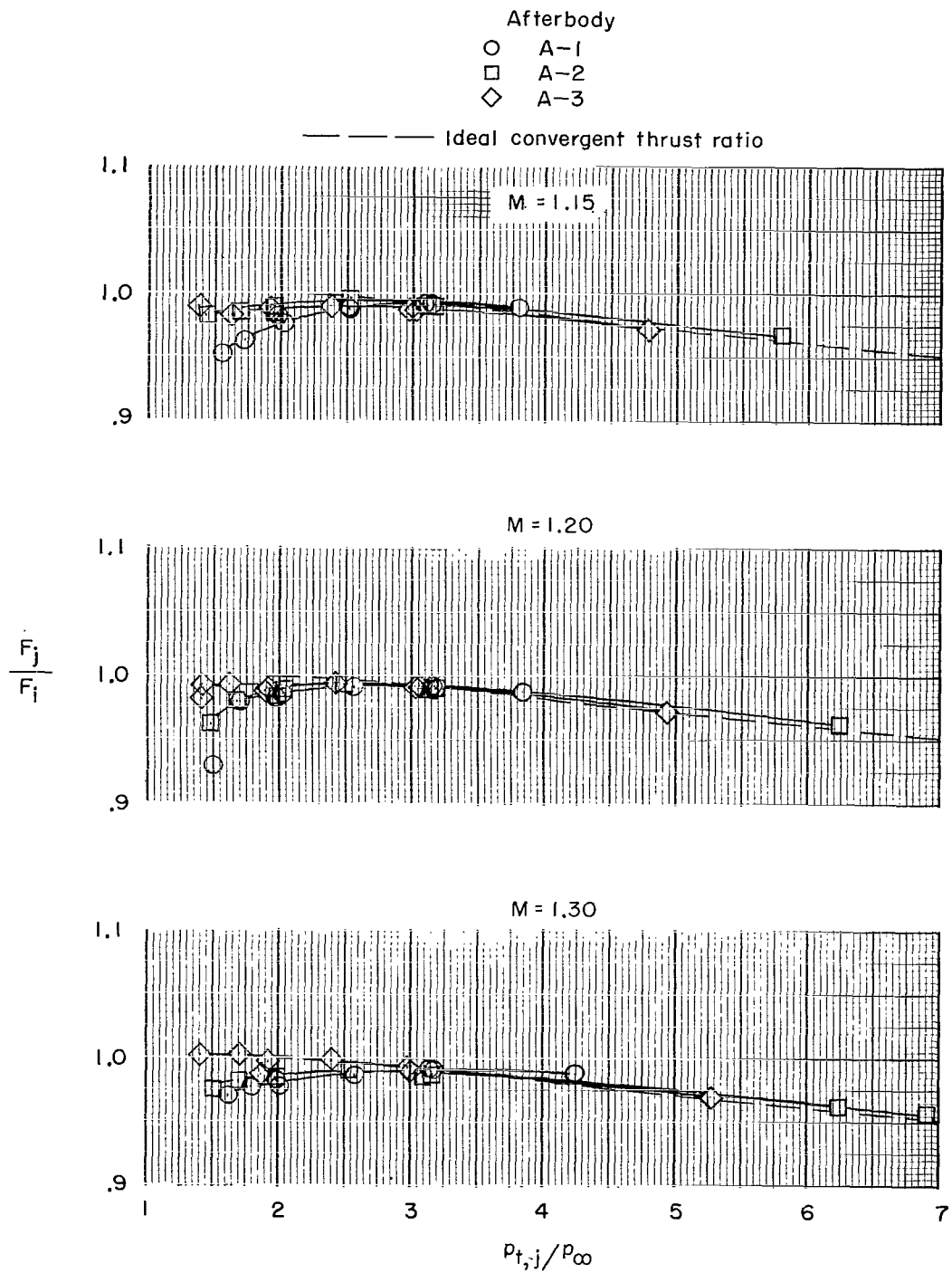
(d) $M = 1.83$ to 2.20 .

Figure 21.- Concluded.



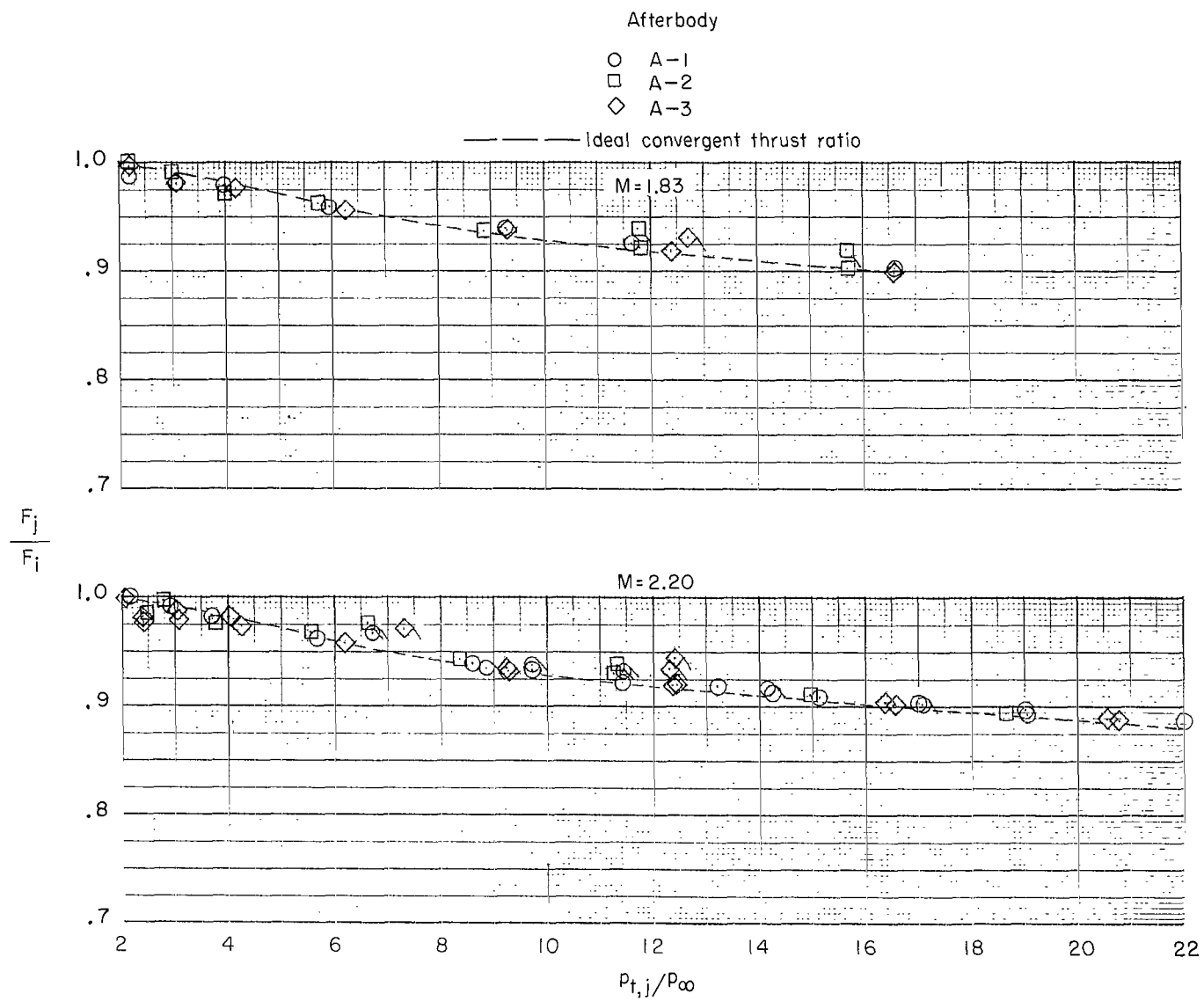
(a) $M = 0.50$ to 0.95 .

Figure 22.- Internal performance at several Mach numbers. Convergent nozzles. Flags denote decreasing pressure ratios.



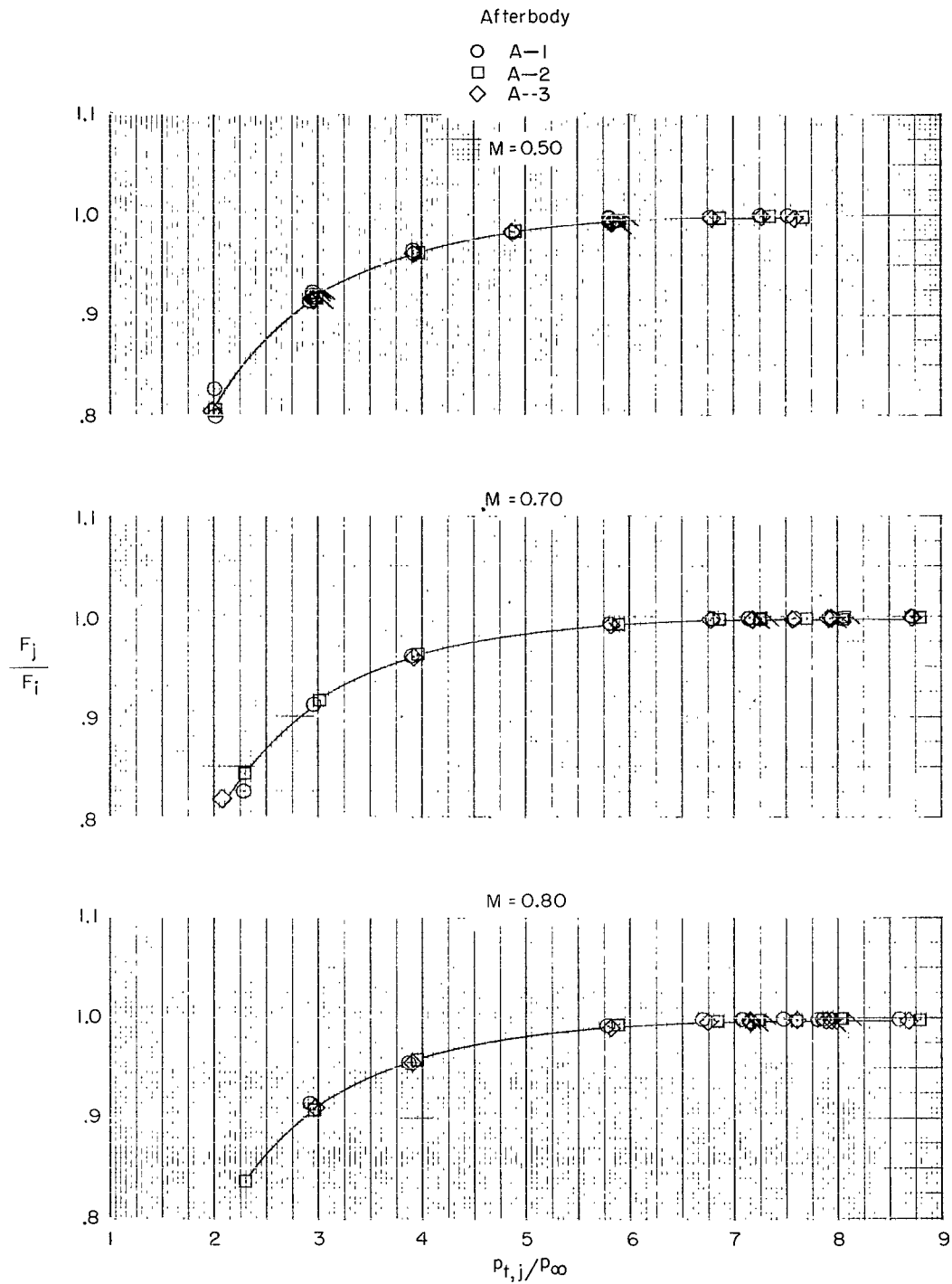
(b) $M = 1.15$ to 1.30 .

Figure 22.- Continued.



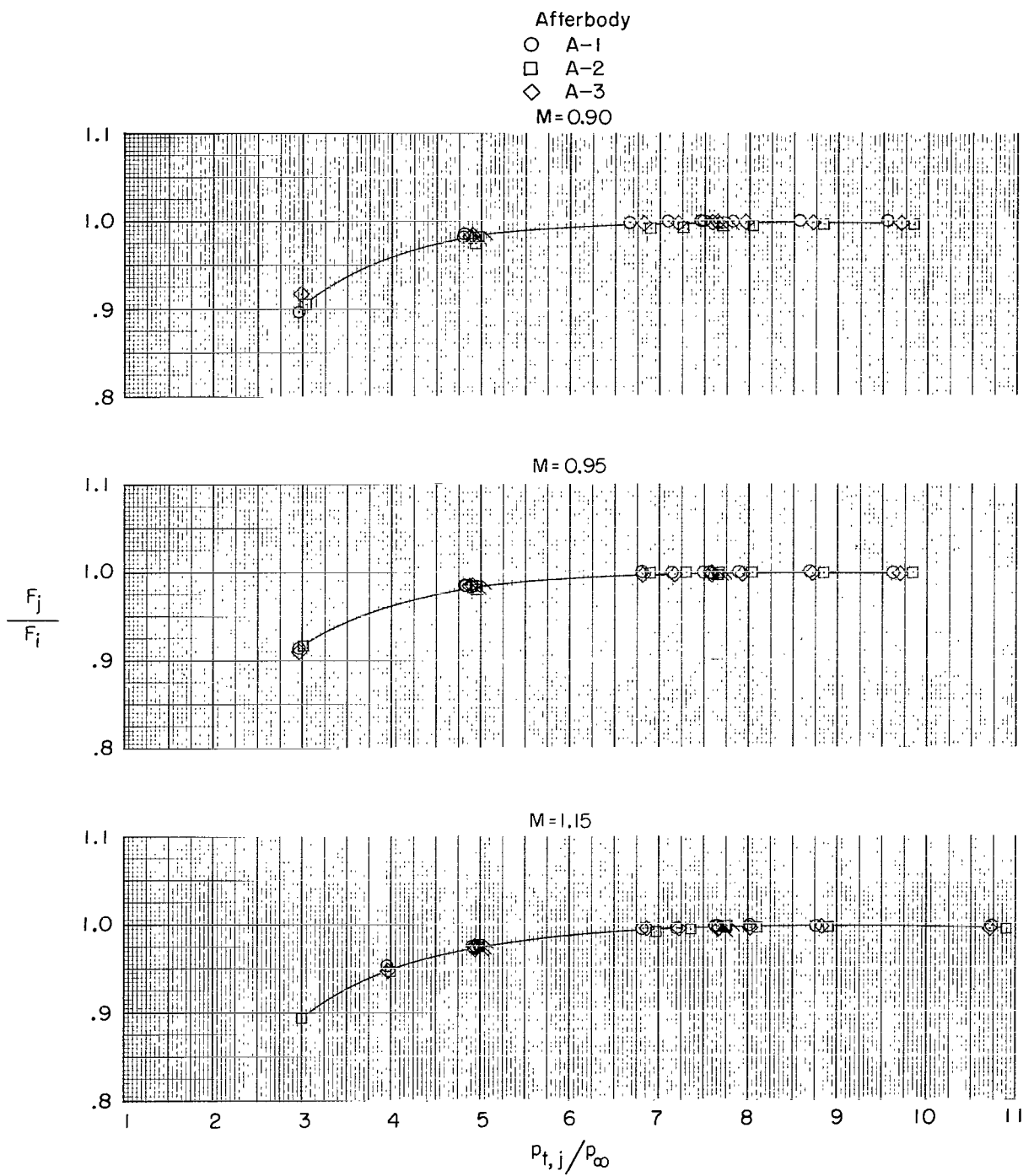
(c) $M = 1.83$ and 2.20 .

Figure 22.- Concluded.



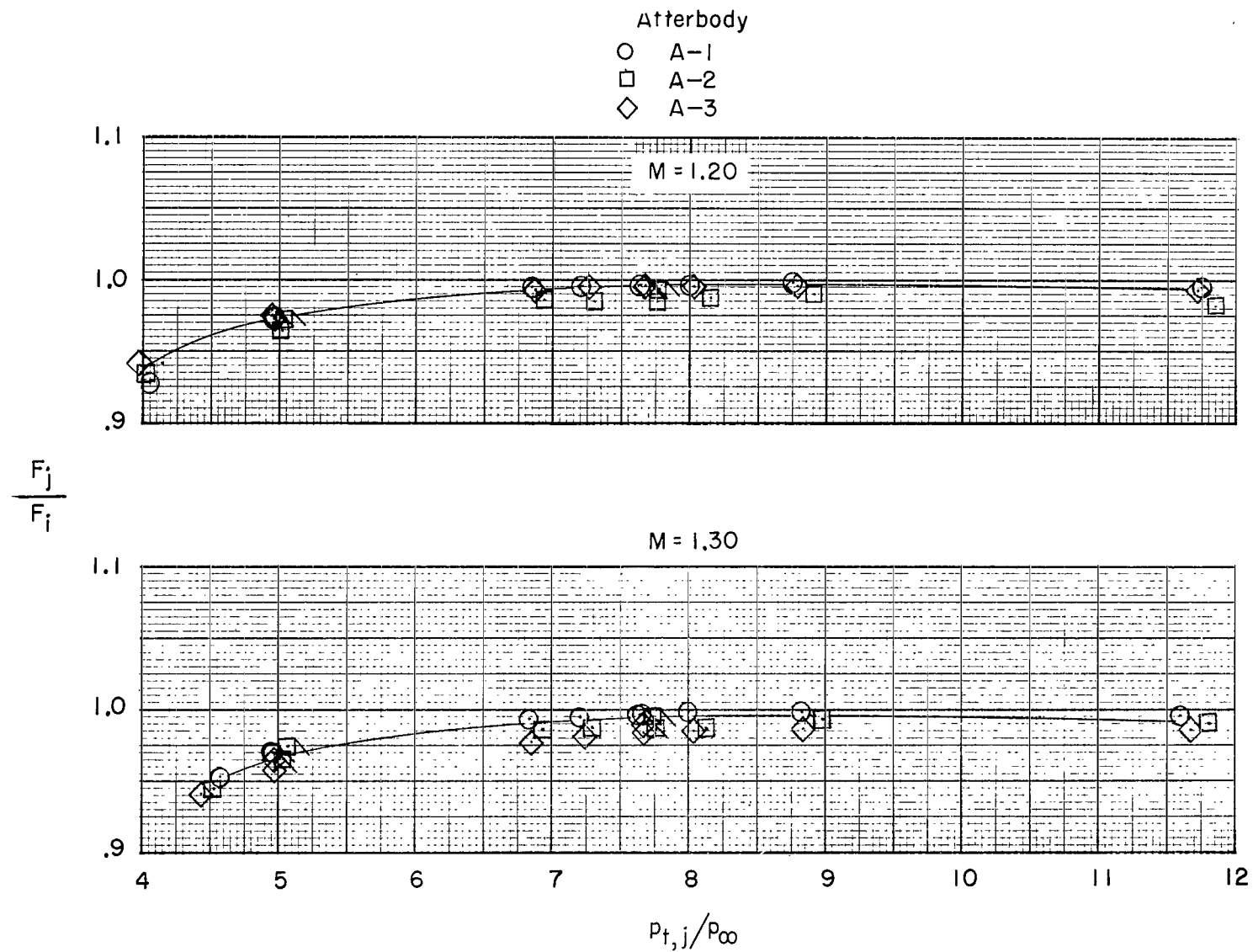
(a) $M = 0.50$ to 0.80 .

Figure 23.- Internal performance at several Mach numbers. Convergent-divergent nozzles. Flags denote decreasing pressure ratios.



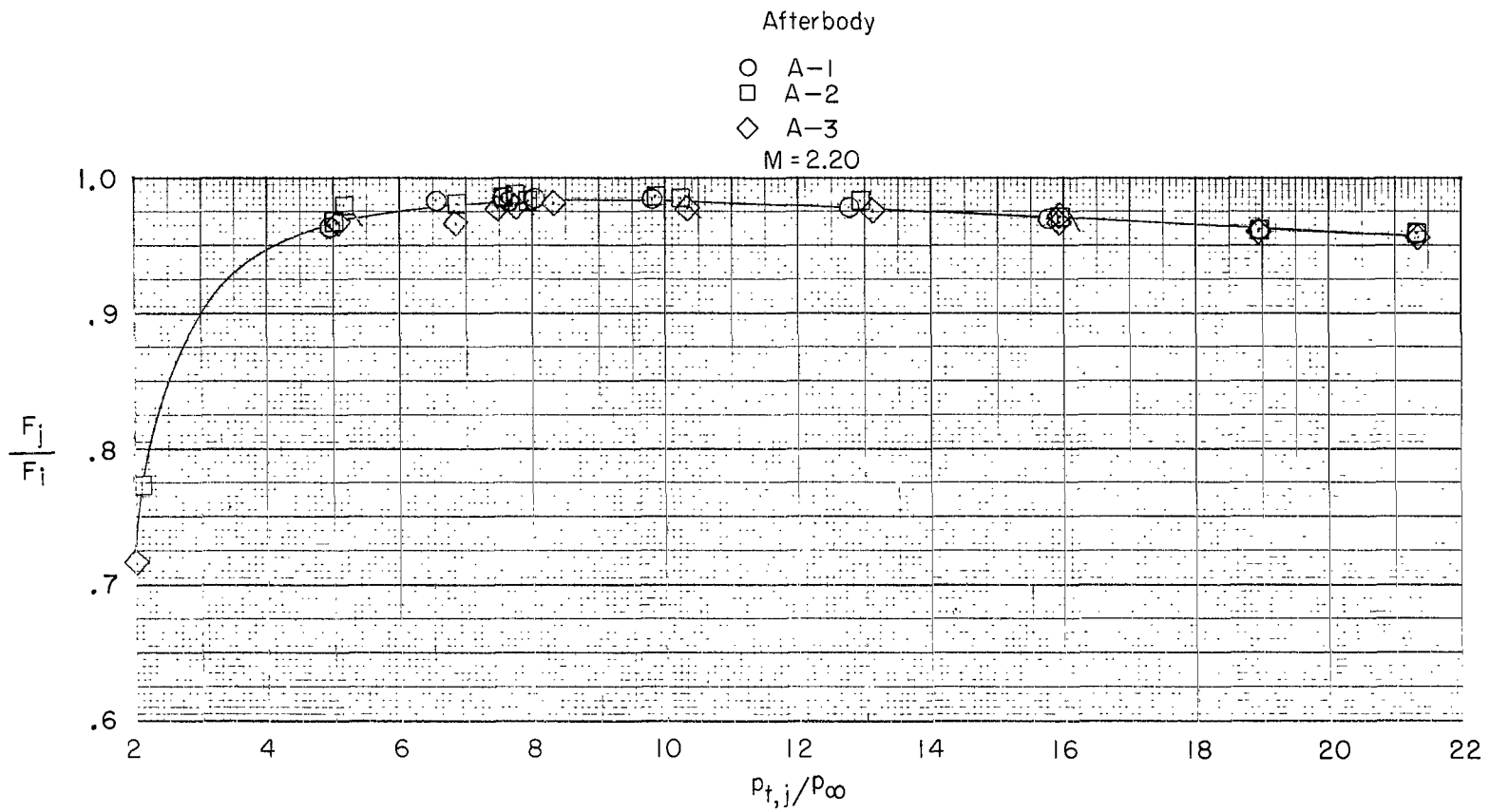
(b) $M = 0.90$ to 1.15 .

Figure 23.- Continued.



(c) $M = 1.20$ and 1.30 .

Figure 23.- Continued.



(d) $M = 2.20$.

Figure 23.- Concluded.

FIRST CLASS MAIL



POSTAGE AND FEES PAID
NATIONAL AERONAUTICS AND
SPACE ADMINISTRATION

C4U C01 53 51 305 69226 00903
AIR FORCE WEAPONS LABORATORY/AFWL/
KIRTLAND AIR FORCE BASE, NEW MEXICO 8711

ATT E. LOU BOWMAN, ACTING CHIEF TECH. LI

POSTMASTER: If Undeliverable (Section 15:
Postal Manual) Do Not Return

"The aeronautical and space activities of the United States shall be conducted so as to contribute . . . to the expansion of human knowledge of phenomena in the atmosphere and space. The Administration shall provide for the widest practicable and appropriate dissemination of information concerning its activities and the results thereof."

— NATIONAL AERONAUTICS AND SPACE ACT OF 1958

NASA SCIENTIFIC AND TECHNICAL PUBLICATIONS

TECHNICAL REPORTS: Scientific and technical information considered important, complete, and a lasting contribution to existing knowledge.

TECHNICAL NOTES: Information less broad in scope but nevertheless of importance as a contribution to existing knowledge.

TECHNICAL MEMORANDUMS: Information receiving limited distribution because of preliminary data, security classification, or other reasons.

CONTRACTOR REPORTS: Scientific and technical information generated under a NASA contract or grant and considered an important contribution to existing knowledge.

TECHNICAL TRANSLATIONS: Information published in a foreign language considered to merit NASA distribution in English.

SPECIAL PUBLICATIONS: Information derived from or of value to NASA activities. Publications include conference proceedings, monographs, data compilations, handbooks, sourcebooks, and special bibliographies.

TECHNOLOGY UTILIZATION PUBLICATIONS: Information on technology used by NASA that may be of particular interest in commercial and other non-aerospace applications. Publications include Tech Briefs, Technology Utilization Reports and Notes, and Technology Surveys.

Details on the availability of these publications may be obtained from:

SCIENTIFIC AND TECHNICAL INFORMATION DIVISION
NATIONAL AERONAUTICS AND SPACE ADMINISTRATION
Washington, D.C. 20546